Multigrid and Defect Correction for the Steady Navier-Stokes Equations

Application to Aerodynamics

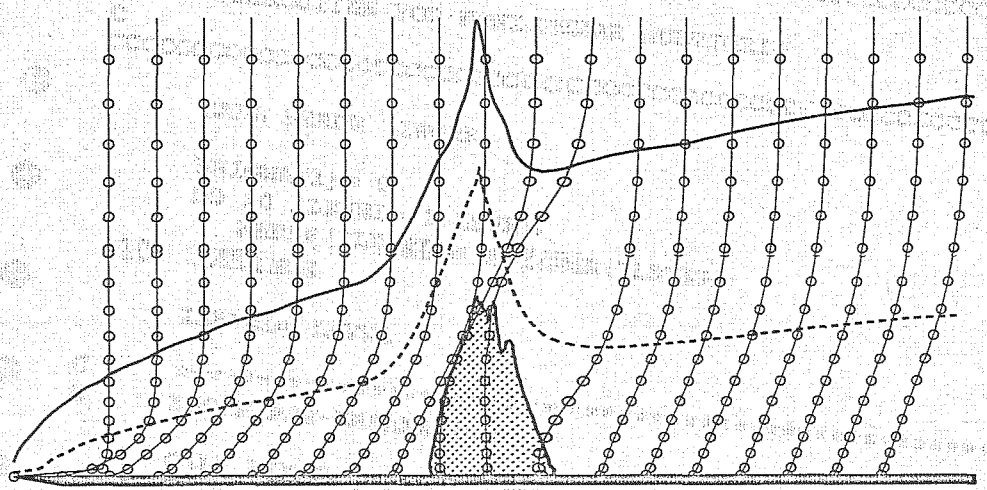

Barry Koren

Multigrid and Defect Correction for the Steady Navier-Stokes Equations

Application to Aerodynamics

Multigrid and Defect Correction for the Steady Navier-Stokes Equations
Application to Aerodynamics

Proefschrift

ter verkrijging van de graad van doctor
aan de Technische Universiteit Delft,
op gezag van de Rector Magnificus,
prof.drs. P.A. Schenck,
in het openbaar te verdedigen
ten overstaan van een commissie
door het College van Dekanen daartoe aangewezen,
op donderdag 11 mei 1989, te 16.00 uur

door

Barend Koren

geboren te Kamerik
vliegtuigbouwkundig ingenieur

Centrum voor Wiskunde en Informatica
Amsterdam
1989

Dit proefschrift is goedgekeurd door de promotor:
prof.dr.ir. P. Wesseling.

Dr. P.W. Hemker heeft als begeleider in hoge mate bijgedragen aan het totstandkomen van het proefschrift.

Aan Wijnie, Gijsbert en Gerbrand

Preface

The subject of this thesis is the accurate and efficient computation of high-speed gas flows described by the steady Navier-Stokes equations. The numerical investigations described are all pointed towards application in aerodynamics.

The Euler flow results presented in chapter 2 of the thesis proceed from the research project *Development of efficient numerical methods for flows described by the steady Euler equations,* which was initiated at the Centre for Mathematics and Computer Science (CWI) in cooperation with the National Aerospace Laboratory (NLR), and which was financially supported by the Netherlands Technology Foundation (STW). The STW-project started in July 1984 and was completed, one year earlier than foreseen, in June 1987. Portable Fortran software for computing steady, two-dimensional Euler flows, a result of the project, was transferred to NLR, Fokker Aircraft, Delft University of Technology, Brussels Free University (VUB), l'Institut National de Recherche en Informatique et en Automatique (INRIA), le Centre Européen de Recherche et de Formation Avancée en Calcul Scientifique (CERFACS), the Weizmann Institute of Science, the University of Michigan, and the University of Colorado at Denver. The STW-project was carried out in the Numerical Mathematics Department of CWI.

The Navier-Stokes and Euler flow results presented in the chapters 3 and 4 result from the still continuing research project *Convergence acceleration of a finite volume Euler and Navier-Stokes solution method and a geometric adaptive multigrid method for finite volume Euler and Navier-Stokes approximation,* which started in July 1987 and which is carried out in the framework of the Hermes Aerothermodynamics Programme of Avions Marcel Dassault - Bréguet Aviation. The project is financially supported by the European Space Agency (via the Dassault - Bréguet company) and is also carried out in the Numerical Mathematics Department of CWI.

This thesis is a synopsis of publications and reports prepared during both aforementioned projects: [10,12,15,16,17,19,20,29] from chapter 2, [5,6,8,9,10,11] from chapter 3, and [11] from chapter 4. I want to thank all those who contributed somehow to this work. In particular, I wish to express my gratitude to my project manager dr. P.W. Hemker (CWI) for his stimulating mathematical ideas, his critical reading of my drafts and his cooperation in our common papers. I am also grateful to my thesis supervisor prof.dr.ir. P. Wesseling (Delft University) for the useful advice given during both projects and for his careful reading of my drafts, including those for this thesis. Further, I want to thank my former co-worker dr.ir. S.P. Spekreijse (NLR) for the fruitful cooperation during the STW-project.

Amsterdam, January 1989 Barry Koren.

Contents

Chapter 1

Introduction

1.1. Introductory remarks

Understanding and controlling the dynamics of fluids is essential for modern technology. For this, in general, both experimental and theoretical means are available. Though experimental fluid dynamics enjoys much confidence because it considers real fluid flows, experiments often are more difficult and more expensive than computations.

Whereas theoretical fluid dynamics has great technological relevance at present, in the past it was mainly of academic interest. Large discrepancies existed between theoretical results and actual observations. As a consequence, early fluid flow technology developed largely independent of theory. However, break-throughs in both theory and technology closed gaps and led to an increasingly fruitful cross-fertilization of both.

The major application of fluid dynamics, which clearly shows this fruitful interaction, is flying with heavier-than-air craft. It can be stated that without theoretical fluid dynamics, the safety and economy of present-day aircraft would be still far out of reach. Yet, despite the many records broken since the early days of flying, every modern aircraft e.g. still merely heats the universe by taking-off with much energy stored in its fuel and by landing with, say, all this energy lost. This and many other challenging fluid flow problems still exist.

1.2. The Navier-Stokes equations

1.2.1. Inviscid equations of motion

A major break-through in theoretical fluid dynamics is Euler's idea to express knowledge about fluid dynamics in the form of partial differential equations [4]. Euler (1707-1783) derived equations of motion for a fluid. We shall proceed to rederive these equations in a sketchy way.

Equations of fluid motion can be derived from Newton's second law which states that the product of mass and acceleration of a body is equal to the sum of the external forces acting on the body. Here we do not consider forces acting throughout the body (such as e.g. gravitation), but only forces acting on the outside, contact forces. The only contact forces that Euler considered were pressure forces. Applying Newton's second law to the motion of a cubic fluid element (Fig. 1.1a), this yields for a compressible fluid

$$\rho\left[\frac{\partial}{\partial t}+u\frac{\partial}{\partial x}+v\frac{\partial}{\partial y}+w\frac{\partial}{\partial z}\right]\begin{bmatrix}u\\v\\w\end{bmatrix}=\frac{\partial}{\partial x}\begin{bmatrix}-p\\0\\0\end{bmatrix}+\frac{\partial}{\partial y}\begin{bmatrix}0\\-p\\0\end{bmatrix}+\frac{\partial}{\partial z}\begin{bmatrix}0\\0\\-p\end{bmatrix}. \quad (1.1)$$

Here u,v and w denote the velocity components in x-, y- and z-direction, respectively, and p and ρ denote the pressure and density, respectively. All five flow quantities are conceived as functions of the time t and the coordinates x,y and z. For their determination, we need two more equations. One extra equation can be derived from the law of conservation of mass, the continuity equation. As the fifth equation we may add the equation of state for the specific fluid considered. If the latter equation contains temperature as an additional flow quantity, the sixth equation needed in that case can be derived from the law of conservation of energy.

Euler's equations of motion (1.1) quickly confirmed the correctness of Bernoulli's reliable and earlier developed formula relating pressure to velocity. 'Unfortunately', the equations also quickly confirmed the 'truth' of the earlier found d'Alembert paradox, which states that a body immersed in fluid flow does not encounter any resistance at all. The shortcoming of the Eulerian flow model is that it assumes fluid flows to be conservative dynamical systems in the sense of Lagrange. Real fluid flows are not. In real flows, friction forces exist.

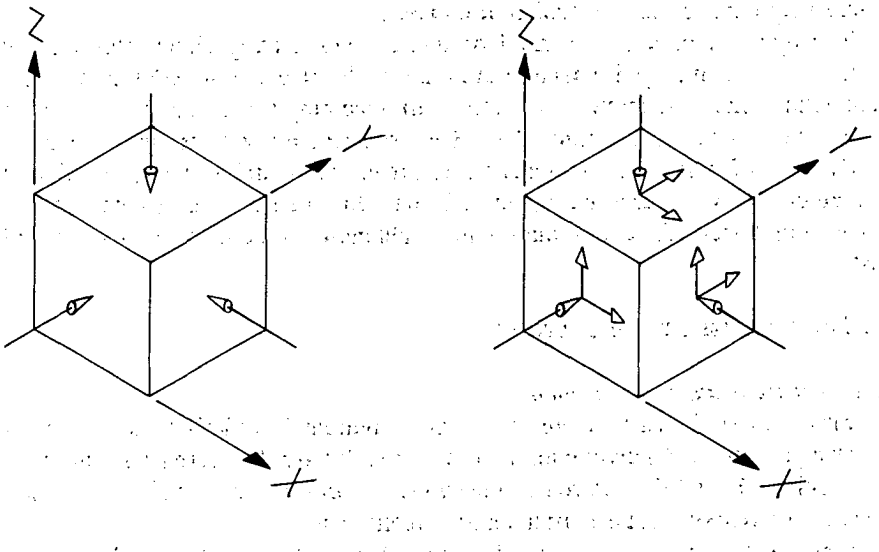

a. Normal stresses. b. Normal and tangential stresses.

Fig. 1.1. Fluid element with stresses acting on its faces.

1.2.2. Viscous equations of motion

In 1845, Stokes (1819-1903) introduced a better mathematical model than Euler's, a model with friction forces (Fig. 1.1b). Stokes extended (1.1) by postulating that Euler's scalar p is in fact a tensor of which, for fluids such as water and air (Newtonian fluids), the elements depend linearly on the local rate of strain tensor [32]. For an isotropic fluid he introduced as the equations of motion

$$\rho\left[\frac{\partial}{\partial t}+u\frac{\partial}{\partial x}+v\frac{\partial}{\partial y}+w\frac{\partial}{\partial z}\right]\begin{bmatrix}u\\v\\w\end{bmatrix}=\frac{\partial}{\partial x}\begin{bmatrix}\sigma_{xx}\\\sigma_{yx}\\\sigma_{zx}\end{bmatrix}+\frac{\partial}{\partial y}\begin{bmatrix}\sigma_{xy}\\\sigma_{yy}\\\sigma_{zy}\end{bmatrix}+\frac{\partial}{\partial z}\begin{bmatrix}\sigma_{xz}\\\sigma_{yz}\\\sigma_{zz}\end{bmatrix}, \tag{1.2a}$$

with

$$\begin{aligned}\sigma_{xx} &= -p+\lambda\left[\frac{\partial u}{\partial x}+\frac{\partial v}{\partial y}+\frac{\partial w}{\partial z}\right]+2\mu\frac{\partial u}{\partial x},\\ \sigma_{yy} &= -p+\lambda\left[\frac{\partial u}{\partial x}+\frac{\partial v}{\partial y}+\frac{\partial w}{\partial z}\right]+2\mu\frac{\partial v}{\partial y},\\ \sigma_{zz} &= -p+\lambda\left[\frac{\partial u}{\partial x}+\frac{\partial v}{\partial y}+\frac{\partial w}{\partial z}\right]+2\mu\frac{\partial w}{\partial z},\end{aligned} \tag{1.2b}$$

and, assuming symmetry

$$\begin{aligned}\sigma_{xy} &= \sigma_{yx} = \mu\left[\frac{\partial v}{\partial x}+\frac{\partial u}{\partial y}\right],\\ \sigma_{yz} &= \sigma_{zy} = \mu\left[\frac{\partial w}{\partial y}+\frac{\partial v}{\partial z}\right],\\ \sigma_{zx} &= \sigma_{xz} = \mu\left[\frac{\partial u}{\partial z}+\frac{\partial w}{\partial x}\right].\end{aligned} \tag{1.2c}$$

Here λ and μ are viscosity coefficients depending on the fluid considered and possibly also on the flow solution. Besides introducing λ, Stokes also eliminated λ by relating it to μ as $3\lambda+2\mu=0$, which states the bulk viscosity to be zero. Assuming incompressibility, (1.2) reduces to a model which has been introduced by Navier (1785-1836), already in 1822 [18].

1.2.3. Navier-Stokes equations in conservation form

With dimensions. Instead of Newton's second law applied to a moving fluid element, as the physical principle for deriving three equations we may also apply the law of conservation of momentum for a fixed volume element through which fluid is flowing. By assuming the bulk viscosity to be zero and μ to be constant, and by separating the pressure and viscous forces, this gives the momentum equations

$$\frac{\partial}{\partial t}\begin{bmatrix}\rho u\\ \rho v\\ \rho w\end{bmatrix}+\frac{\partial}{\partial x}\begin{bmatrix}\rho u^2+p\\ \rho uv\\ \rho uw\end{bmatrix}+\frac{\partial}{\partial y}\begin{bmatrix}\rho vu\\ \rho v^2+p\\ \rho vw\end{bmatrix}+\frac{\partial}{\partial z}\begin{bmatrix}\rho wu\\ \rho wv\\ \rho w^2+p\end{bmatrix}-$$

$$\mu\left[\frac{\partial}{\partial x}\begin{bmatrix}\tau_{xx}\\ \tau_{yx}\\ \tau_{zx}\end{bmatrix}+\frac{\partial}{\partial y}\begin{bmatrix}\tau_{xy}\\ \tau_{yy}\\ \tau_{zy}\end{bmatrix}+\frac{\partial}{\partial z}\begin{bmatrix}\tau_{xz}\\ \tau_{yz}\\ \tau_{zz}\end{bmatrix}\right]=0, \tag{1.3a}$$

with

$$\begin{aligned}\tau_{xx} &= +\frac{4}{3}\frac{\partial u}{\partial x}-\frac{2}{3}\frac{\partial v}{\partial y}-\frac{2}{3}\frac{\partial w}{\partial z},\\ \tau_{yy} &= -\frac{2}{3}\frac{\partial u}{\partial x}+\frac{4}{3}\frac{\partial v}{\partial y}-\frac{2}{3}\frac{\partial w}{\partial z},\\ \tau_{zz} &= -\frac{2}{3}\frac{\partial u}{\partial x}-\frac{2}{3}\frac{\partial v}{\partial y}+\frac{4}{3}\frac{\partial w}{\partial z},\end{aligned} \tag{1.3b}$$

and

$$\begin{aligned}\tau_{xy} &= \tau_{yx} = \frac{\partial v}{\partial x}+\frac{\partial u}{\partial y},\\ \tau_{yz} &= \tau_{zy} = \frac{\partial w}{\partial y}+\frac{\partial v}{\partial z},\\ \tau_{zx} &= \tau_{xz} = \frac{\partial u}{\partial z}+\frac{\partial w}{\partial x}.\end{aligned} \tag{1.3c}$$

When considering a fluid with equation of state $p=p(\rho,T)$, with T denoting temperature, as mentioned, besides the mass-conservative continuity equation, an energy-conservative equation can be used for completing the system. In combination with the momentum equations, this yields a system which is consistently based on conservation laws, the Navier-Stokes equations in conservation form. For the (more convenient) two-dimensional case this system reads

$$\frac{\partial}{\partial t}\begin{bmatrix}\rho\\ \rho u\\ \rho v\\ \rho e\end{bmatrix}+\frac{\partial}{\partial x}\begin{bmatrix}\rho u\\ \rho u^2+p\\ \rho uv\\ \rho u(e+\frac{p}{\rho})\end{bmatrix}+\frac{\partial}{\partial y}\begin{bmatrix}\rho v\\ \rho vu\\ \rho v^2+p\\ \rho v(e+\frac{p}{\rho})\end{bmatrix}-$$

$$\mu\left[\frac{\partial}{\partial x}\begin{bmatrix}0\\ \tau_{xx}\\ \tau_{xy}\\ u\tau_{xx}+v\tau_{xy}\end{bmatrix}+\frac{\partial}{\partial y}\begin{bmatrix}0\\ \tau_{xy}\\ \tau_{yy}\\ u\tau_{xy}+v\tau_{yy}\end{bmatrix}\right]-$$

$$k\left[\frac{\partial^2}{\partial x^2}\begin{bmatrix}0\\0\\0\\T\end{bmatrix}+\frac{\partial^2}{\partial y^2}\begin{bmatrix}0\\0\\0\\T\end{bmatrix}\right]=0. \tag{1.4}$$

In the energy equation, e denotes the total internal energy per unit of mass, $e=c_v T+\frac{1}{2}(u^2+v^2)$ with c_v the (constant) specific heat at constant density. Further, k denotes the heat conductivity which, analogous to μ, we assume to be constant.

Without dimensions. To obtain a convenient non-dimensional form of the Navier-Stokes equations, the coordinates are made non-dimensional by some characteristic length $\tilde{l}$, the velocity components by some characteristic speed $\tilde{v}$, density by some characteristic density $\tilde{\rho}$, and, consequently, time by $\tilde{l}/\tilde{v}$, pressure by $\tilde{\rho}\tilde{v}^2$ and temperature by $\tilde{v}^2/c_v$. Maintaining the same notation for the non-dimensional variables, and grouping together the elliptic (viscous and heat conduction) terms, (1.4) can be rewritten as

$$\frac{\partial}{\partial t}\begin{bmatrix}\rho\\ \rho u\\ \rho v\\ \rho e\end{bmatrix}+\frac{\partial}{\partial x}\begin{bmatrix}\rho u\\ \rho u^2+p\\ \rho uv\\ \rho u\left(e+\frac{p}{\rho}\right)\end{bmatrix}+\frac{\partial}{\partial y}\begin{bmatrix}\rho v\\ \rho vu\\ \rho v^2+p\\ \rho v\left(e+\frac{p}{\rho}\right)\end{bmatrix}-$$

$$\frac{1}{Re}\left[\frac{\partial}{\partial x}\begin{bmatrix}0\\ \tau_{xx}\\ \tau_{xy}\\ u\tau_{xx}+v\tau_{xy}+\frac{\gamma}{Pr}\frac{\partial T}{\partial x}\end{bmatrix}+\frac{\partial}{\partial y}\begin{bmatrix}0\\ \tau_{xy}\\ \tau_{yy}\\ u\tau_{xy}+v\tau_{yy}+\frac{\gamma}{Pr}\frac{\partial T}{\partial y}\end{bmatrix}\right]=0, \tag{1.5}$$

with $e=T+\frac{1}{2}(u^2+v^2)$, $Re\equiv\tilde{\rho}\tilde{v}\tilde{l}/\mu$ the Reynolds number, $Pr\equiv\mu c_p/k$ the Prandtl number, c_p being the (constant) specific heat at constant pressure, and $\gamma\equiv c_p/c_v$. The Reynolds number measures the ratio between convection and diffusion. Most flows which are of aerodynamic interest have $Re\gg 1$, and hence are convection dominated. In the diffusive operator, the Prandtl number is the ratio of viscous and heat conduction terms. For air e.g. $Pr=$ O(1), with - as a consequence - a diffusion of kinetic and thermal energy which is of the same order of magnitude; this implies approximately equally thick kinetic and thermal layers.

With the introduction of the Navier-Stokes equations, theoretical fluid dynamics seemed to be reduced to a large extent to a purely mathematical exercise requiring the integration of systems such as (1.5). Understanding and controlling a large class of fluid flows from a few basic differential equations seemed to be close at hand.

1.3. Computational methods

1.3.1. Analytical methods

The introduction of the Navier-Stokes equations inaugurated a period of great advances in theoretical fluid dynamics. Riemann gave an analysis of compressible plane waves of finite amplitude in inviscid fluids. Green constructed potential flows around ellipsoids, and somewhat later, many plane potential flows were constructed by conformal transformations of the flow around a circular cylinder. Kelvin introduced a theorem on the invariance of circulation implying the persistence of potential flow in an incompressible inviscid flow. Green, Airy and Kelvin systematized and extended theories of tides and waves. Rankine determined algebraic equations governing shock waves. Helmholtz, Kelvin and Rayleigh used vortex motions for explaining phenomena such as smoke rings, aeolian tones and cyclones, whereas Helmholtz and Kelvin also notably advanced the theory of sound. . . . A detailed documentation of these and many other advances in theoretical fluid dynamics can be found in [13].

Yet, no real progress was made in integrating the full Navier-Stokes equations. In fact, all advances made have in common that they simplify the full Navier-Stokes equations in such a way that a flow model is obtained which, as opposed to the full Navier-Stokes equations, is analytically tractable. Further, despite the many theoretical successes, large discrepancies remained between fluid dynamics in theory and in practice, the latter developing independently in the industrial revolution that took place simultaneously.

The greatest discrepancy remained in the theory of drag, until in 1904 Prandtl introduced his boundary layer theory [21]. It had always been difficult to comprehend that frictional forces could influence flows of e.g. water and air to so large an extent as indicated by drag measurements, because nature also showed that the viscosity of these fluids is very small. Prandtl found that the observed momentum loss in wakes must have its counterpart in frictional forces, and showed that there are thin layers along a body where friction plays an essential role indeed. From the full Navier-Stokes equations, by simplification Prandtl derived the boundary layer equations, exploiting the small thickness of the layers. Suddenly a high degree of correlation was achieved between theory and practice, and a new impetus was given to both of them, a good example being airfoil theory and flying, respectively. An account of this and other advances can be found in e.g. [22,23].

However, even the practically relevant boundary layer theory quickly showed its limitations. Commonly occurring thick boundary layer flows e.g. could not be analyzed. (An important phenomenon such as stall cannot be analyzed by boundary layer theory.) Further, already for very simple geometries, integration of the boundary layer equations required great skill. In fact stagnation arose along the entire front of the nonlinear problems arising more and more in fluid dynamics. In conclusion, it was paradoxical to see that the introduction of the general Navier-Stokes equations only led to an even greater fragmentation into different flow models, flow models which are all intended to describe the motion of the same Newtonian fluid.

1.3.2. Numerical methods

The limited capabilities of analytical methods and the large fragmentation into different simplified models created a strong demand for the development of a numerical method for (finally) integrating the full Navier-Stokes equations.

Analogous to the introduction of the Navier-Stokes equations, the invention of the digital computer also inaugurated a period of great progress in theoretical fluid dynamics. Von Neumann et al. presented a method allowing computations with the nonlinear, three-dimensional vorticity equations. Crank and Nicolson published a method allowing the computation of general boundary layer flows. Dufort and Frankl introduced a method that allowed the computation of unsteady vortex streets. Peaceman and Rachford introduced solution methods for efficient computations with the incompressible Navier-Stokes equations. Von Neumann and Richtmyer proposed a method for computing flows with shock waves. Courant, Isaacson and Rees introduced a method accounting for the direction of wave propagation. . . . A survey of these and many other early advances in numerical fluid dynamics can be found in e.g. [24,25].

New mathematical concepts that are irrelevant for analytical methods arose as crucial properties of numerical methods, properties such as consistency, numerical stability and convergence. Given a numerical method, mathematics offers many tools for studying these properties. Unfortunately, the complexity of a flow model such as the full Navier-Stokes equations inhibits rigorous numerical analysis. In general, we can only perform rigorous analyses for strongly simplified models. Additional confidence can be gained by performing appropriate experiments with the full equations and the numerical method considered. As opposed to analytical fluid dynamics, heuristics is a characteristic component in numerical fluid dynamics. Though at present, in many cases, numerical methods allow an easy integration of the full Navier-Stokes equations, probably as a consequence of the dependence on heuristics, so far no ultimate numerical method exists for this purpose. Whereas in analytical fluid dynamics a large fragmentation into *models* was arising, in numerical fluid dynamics we observe a still increasing fragmentation into different *methods* per model. Furthermore, numerical methods, by giving discrete data only, do not provide functional relationships, as opposed to analytical methods. As a consequence, numerical fluid dynamics is less suitable for qualitative studies.

The early idea of von Neumann that with 'automatic computing machines' it would at least become possible to completely replace analytical fluid dynamics by numerical fluid dynamics (tackling full nonlinear flow models in general geometries), and that with sufficiently powerful machines it would even become possible to completely replace experimental fluid dynamics, obviously did not become reality so far. At present, a common opinion is that all three branches of fluid dynamics supplement each other invaluably, and will remain to do so for the time being.

1.4. Purpose of this study

1.4.1. Steady Navier-Stokes equations

The aim of the present study is to develop an accurate and in particular an efficient numerical method for the steady, two-dimensional, compressible Navier-Stokes equations, which we write in the following form

$$\frac{\partial f(q)}{\partial x} + \frac{\partial g(q)}{\partial y} - \frac{1}{Re}\left[\frac{\partial r(q)}{\partial x} + \frac{\partial s(q)}{\partial y}\right] = 0, \tag{1.6a}$$

with q the conservative state vector

$$q = \begin{bmatrix} \rho \\ \rho u \\ \rho v \\ \rho e \end{bmatrix}, \tag{1.6b}$$

$f(q)$ and $g(q)$ the convective flux vectors

$$f(q) = \begin{bmatrix} \rho u \\ \rho u^2 + p \\ \rho uv \\ \rho u(e + \frac{p}{\rho}) \end{bmatrix}, \quad g(q) = \begin{bmatrix} \rho v \\ \rho vu \\ \rho v^2 + p \\ \rho v(e + \frac{p}{\rho}) \end{bmatrix}, \tag{1.6c}$$

and $r(q)$ and $s(q)$ the diffusive flux vectors

$$r(q) = \begin{bmatrix} 0 \\ \tau_{xx} \\ \tau_{xy} \\ u\tau_{xx} + v\tau_{xy} + \dfrac{\gamma}{Pr}\dfrac{\partial T}{\partial x} \end{bmatrix}, \quad s(q) = \begin{bmatrix} 0 \\ \tau_{xy} \\ \tau_{yy} \\ u\tau_{xy} + v\tau_{yy} + \dfrac{\gamma}{Pr}\dfrac{\partial T}{\partial y} \end{bmatrix}. \tag{1.6d}$$

The relevance of having both good accuracy and efficiency is obvious; in practice one is always interested in the highest accuracy at the lowest expense.

For many flows of practical interest, the assumption of steadyness is not too drastic. (Most flight conditions of aircraft e.g. can be assumed to be steady by good approximation, in particular of course the important cruising flight condition.) Though to a smaller extent than steadyness, the assumption of two-dimensionality still allows practically relevant computations as well. (Airfoil flow computations e.g. remain important for the design of complete wings.)

The Reynolds numbers that we are interested in lie in a wide range of practically interesting high Reynolds numbers, $0 \leqslant 1/Re \leqslant$ O(100), whereas the flow speeds that we are mainly interested in range from medium-subsonic to medium-supersonic. With M denoting the Mach number $M \equiv \sqrt{u^2+v^2}/c$, c denoting the speed of sound, this range can be globally quantified as $\frac{1}{3} \lesssim M \lesssim 3$. A short exploration will also be made into a hypersonic flow regime; $3 \lesssim M \lesssim 10$.

1.4.2. Perfect gas

As the fluid we consider a gas that is assumed to be perfect for the complete Mach number range under consideration. With the perfect gas equation of state $p=\rho RT$, R denoting the specific gas constant, and with the non-dimensionalization applied in section 1.2.3, the non-dimensional equation of state reads $p=(\gamma-1)\rho T$. For a perfect gas the speed of sound is given by (with and without dimensions) $c^2=\gamma p/\rho$.

For gases with multi-atomic molecules, over the complete Mach number range considered, we assume γ to be constant and to be determined by fully excited translational and rotational energies only. (The vibrational energy is assumed to be zero.)

1.5. Point of departure

1.5.1. Steady Euler equations

When developing a numerical method for high-Reynolds number flows, in the first instance it is useful to refrain from taking Re to be a variable parameter and to appropriately fix it at $1/Re=0$. With the Navier-Stokes equations (1.6), this leads us to the steady, two-dimensional Euler equations

$$\frac{\partial f(q)}{\partial x}+\frac{\partial g(q)}{\partial y}=0, \tag{1.7}$$

which are of course significantly less intricate than (1.6), but still have all major mathematical difficulties of (1.6) gathered in them. An additional advantage of employing the Euler equations as a platform for developing a numerical method for the Navier-Stokes equations is that analytical methods for non-dissipative flow models are further developed than those for dissipative flow models, with - as a consequence - the availability of more and better reference results. Of course, as already mentioned in section 1.2.1, the practical relevance of the Euler equations is limited, their subsonic zero-drag predictions being a striking example of this.

By going from Navier-Stokes to Euler we have (re)introduced our dynamically conservative system, a system in which the flow processes are reversible. In nature, all (adiabatic) processes are irreversible, i.e. guided by the principle that entropy can only increase. Hence the Euler equations, as a reversible system, allow physically unrealistic entropy decreases. To avoid such spurious solutions, all existing numerical methods for the Euler equations satisfy the entropy principle by adding a proper amount of numerical diffusion.

Further, by going from Navier-Stokes to Euler, solutions with layers of Re-dependent thickness have been 'simplified' to solutions with layers shrunk to zero-thickness: discontinuities. Since at discontinuities differential equations are not valid, the Euler equations require a more general concept of possible solutions than the Navier-Stokes equations. For this purpose, following Lax [14], instead of the differential form (1.7), most existing Euler methods are based on the integral form

$$\oint (f(q)n_x + g(q)n_y)ds = 0, \tag{1.8}$$

which is in fact the form in which the Euler equations first arise when deriving them for a fixed volume element.

1.5.2. Efficient numerical methods

Fully implicit methods. Considering a two-dimensional computational domain which may be curved, e.g. wrapped around an airfoil, a straightforward system of discretized equations is obtained by (i) subdividing that domain into non-overlapping subdomains, (ii) requiring (1.8) to hold for each subdomain separately, and by (iii) invoking some numerical method for evaluating the convective flux vector across each subdomain face. However, for the Mach number range considered, the solution of such a system is not that straightforward. The discrete system is of the same complex mathematical type as the continuous system, it is simply hyperbolic in supersonic flow regions but hybrid (mixed hyperbolic-elliptic) in subsonic flow regions. Only for completely supersonic flows a straightforward and efficient solution method exists: space marching. For most supersonic flows space marching is hardly interesting because of the common occurrence of locally normal shock waves, producing locally subsonic flow regions. Given moreover the complete unsuitability of space marching for the intended extension to Navier-Stokes, it is absolutely out of interest here.

An early remedy to avoid the difficulty in solving discrete steady Euler equations was to take the continuous unsteady Euler equations

$$\int\int \frac{\partial q}{\partial t} dx\, dy + \oint (f(q)n_x + g(q)n_y)ds = 0 \tag{1.9}$$

as a point of departure. The unsteady Euler equations are hyperbolic with respect to time (independent of the Mach number) and thus allow time marching from a conveniently chosen initial solution to a solution which is the asymptotic steady state of an unsteady process. Many time stepping schemes have been developed so far. Basically, two classes can be considered: (i) schemes in which the time discretization is coupled with the space discretization (Lax-Wendroff-type schemes), and (ii) schemes which have no such coupling (semi-discretization-type schemes). In an explicit time stepping formulation, for both classes, an efficient solution is hampered by a stability restriction imposed on the time step. Furthermore, even in an implicit formulation, Lax-Wendroff-type schemes are hampered by an accuracy restriction imposed on the time step. Because of the fact that for both restrictions the maximally allowable time step is proportional to the local mesh size, and because of the fact that in Navier-Stokes flow computations the local mesh sizes may become very small, to our opinion, Lax-Wendroff-type schemes and explicit semi-discretization-type schemes are not interesting from the viewpoint of efficiency. Because of their unconditional stability and accuracy, to our opinion, only fully implicit semi-discretization-type schemes are. These schemes allow

infinitely large time steps, actually abolishing time as an independent variable. Hence for infinitely large time steps, fully implicit semi-discretization-type schemes can be interpreted as direct solvers, or relaxation methods, for the steady equations. (With the time step increasing to infinity, e.g. backward Euler applied to (1.9) passes into Newton applied to (1.8).)

Multigrid methods. In general, as far as efficiency is concerned, a drawback of single-grid solution methods is that smooth components, which are efficiently approximated on coarse grids but are slow to converge in fine grid processes, conflict with short-wave-length components which must be approximated on fine grids. Due to Brandt, Hackbusch and others (see [2] for an extensive multigrid bibliography), it is well-known nowadays that a very significant further efficiency improvement can be obtained by employing interactively several (geometric) scales of discretization: a (geometric) multigrid technique. The main advantage of a multigrid technique over other acceleration techniques is that under quite general conditions, the convergence rate is independent of the problem size. Other techniques slow down when the discretization becomes finer. In the beginning, multigrid techniques only existed for systems arising from the discretization of elliptic partial differential equations. Later they were also applied with success to parabolic problems, and to problems involving integral equations. No indication existed that multigrid would not work for other types of equations, such as the steady Euler equations (being hybrid in subsonic flow regions and hyperbolic in supersonic regions).

Recently, two different multigrid approaches have been developed for numerical methods directly tackling the steady Euler equations by some relaxation method. The first approach falls back on well-developed multigrid work. For the relaxation method, it linearizes a large subsystem (e.g. a line in a two-dimensional problem) or possibly the complete system of discretized equations, and then applies, inside the relaxation, multigrid iteration to the solution of the resulting system of linear equations *(linear multigrid).* The other approach applies multigrid directly to the system of nonlinear discretized equations *(nonlinear multigrid)* and applies, inside that, a relaxation to a subsystem; e.g. a line in a two-dimensional problem but usually a single point only. To the steady Euler equations, the linear multigrid approach has been applied by Jespersen [11], Mulder [17], and Lallemand [12]. The nonlinear approach has been applied by Steger [30], Jespersen [11], Hemker and Spekreijse [9], and Dick [3]. An advantage of the linear approach is that linear multigrid (LMG or CS) is further developed than nonlinear multigrid (NMG or FAS), both in theory and in practice. However, practical drawbacks of linear multigrid are that (i) in general it requires much more storage than nonlinear multigrid, and that (ii) it does not allow a fine grid initialization in the same natural way as the nonlinear approach does by iterative solution prolongation from the underlying coarser grid(s): nested iteration (FMG). To prevent the initial solution from lying outside the attraction domain of the relaxation method, in [17] the original fully-implicitness, an essential element for high efficiency, is even abandoned by applying a Rosenbrock method which is gradually transformed into

Newton during the iteration.

Crucial for the success of both multigrid approaches is that short-wavelength components are efficiently damped on the finest level. This smoothing property requires the discretization to be sufficiently dissipative. A sufficient and in particular natural dissipation is guaranteed by first-order upwind schemes. Continuous differentiability of these schemes, as required by Newton methods, is not guaranteed in general, Godunov's scheme [5] being a striking example. Fortunately, continuously differentiable upwind schemes exist now.

It should be noticed that multigrid acceleration for steady Euler flow computations is not restricted to relaxation schemes, but has also been applied (and still is applied) to time stepping schemes. Well-known and widely used are Ni's multigrid method [19] which is based on a Lax-Wendroff time stepping scheme, and Jameson's method [10] which is based on an explicit semi-discretization-type scheme.

1.5.3. An efficient and accurate numerical method

By applying a relaxation method with multigrid as acceleration technique, high efficiency can be obtained. Unfortunately, we cannot expect more than we pay for. In general, for a given grid, multigrid does not allow sufficiently accurate solutions, because, in general, too dissipative discretizations are required. A natural remedy to this problem has been given by Hemker [8]. The remedy is natural in the sense that it first recognizes that multigrid fits in the general mathematical framework of defect correction processes, and then extends, within this framework, a given multigrid method for first-order accurate systems to a method for higher-order accurate systems. The multigrid technique extended is that developed earlier, for the steady Euler equations, by Hemker and Spekreijse [9]. Both the multigrid and defect correction technique are taken as a point of departure here. We proceed in giving a summary of both.

Discretization method. In the standard way, Hemker and Spekreijse discretize the Euler equations in the integral form

$$\oint_{\partial\Omega^*} (f(q)\cos\phi + g(q)\sin\phi)ds = 0, \tag{1.10}$$

where Ω^* is an arbitrary subdomain of the computational domain Ω, $\partial\Omega^*$ the boundary of Ω^*, and $\cos\phi$ and $\sin\phi$ the x- and y-component of the outward unit normal on $\partial\Omega^*$. A straightforward and simple discretization is obtained by subdividing Ω, in a structured manner, into disjunct, non-overlapping subdomains $\Omega_{i,j}$, $i = 1,2,...,I$, $j = 1,2,...,J$ (finite volumes), and by requiring that

$$\oint_{\partial\Omega_{i,j}} (f(q)\cos\phi + g(q)\sin\phi)ds = 0, \quad \forall_{i,j}. \tag{1.11}$$

Using the rotational invariance of the Euler equations

$$f(q)\cos\phi + g(q)\sin\phi = T^{-1}(\phi)f(T(\phi)q), \tag{1.12}$$

where $T(\phi)$ is the rotation matrix

$$T(\phi) = \begin{bmatrix} 1 & 0 & 0 & 0 \\ 0 & \cos\phi & \sin\phi & 0 \\ 0 & -\sin\phi & \cos\phi & 0 \\ 0 & 0 & 0 & 1 \end{bmatrix}, \tag{1.13}$$

(1.11) can be rewritten as

$$\oint_{\partial\Omega_{i,j}} T^{-1}(\phi) f(T(\phi)q) ds = 0. \tag{1.14}$$

As finite volumes arbitrarily shaped quadrilaterals are considered, the structured subdivision being such that $\Omega_{i\pm1,j}$ and $\Omega_{i,j\pm1}$ are the neighbouring volumes of $\Omega_{i,j}$ (Fig. 1.2a). In this discretization a proper evaluation of the flux vector along $\partial\Omega_{i,j}$ is crucial for the success of the multigrid technique. Following the Godunov approach [5], along each cell face the flux vector is assumed to be constant, and to be determined by a uniformly constant left and right state, q^l and q^r (Fig. 1.2b), only. Hence (1.14) becomes

$$\begin{aligned} \mathcal{F}_{i,j}(q_{i,j}) \equiv\ & T^{-1}(\phi_{i+\frac{1}{2},j}) F(T(\phi_{i+\frac{1}{2},j}) q^l_{i+\frac{1}{2},j},\ T(\phi_{i+\frac{1}{2},j}) q^r_{i+\frac{1}{2},j}) l_{i+\frac{1}{2},j} - \\ & T^{-1}(\phi_{i-\frac{1}{2},j}) F(T(\phi_{i-\frac{1}{2},j}) q^l_{i-\frac{1}{2},j},\ T(\phi_{i-\frac{1}{2},j}) q^r_{i-\frac{1}{2},j}) l_{i-\frac{1}{2},j} + \\ & T^{-1}(\phi_{i,j+\frac{1}{2}}) F(T(\phi_{i,j+\frac{1}{2}}) q^l_{i,j+\frac{1}{2}},\ T(\phi_{i,j+\frac{1}{2}}) q^r_{i,j+\frac{1}{2}}) l_{i,j+\frac{1}{2}} - \\ & T^{-1}(\phi_{i,j-\frac{1}{2}}) F(T(\phi_{i,j-\frac{1}{2}}) q^l_{i,j-\frac{1}{2}},\ T(\phi_{i,j-\frac{1}{2}}) q^r_{i,j-\frac{1}{2}}) l_{i,j-\frac{1}{2}} = 0, \end{aligned} \tag{1.15}$$

where e.g. $F(T(\phi_{i+\frac{1}{2},j}) q^l_{i+\frac{1}{2},j},\ T(\phi_{i+\frac{1}{2},j}) q^r_{i+\frac{1}{2},j})$ represents the transport of mass, momentum and energy (per unit of length and time) across $\partial\Omega_{i+\frac{1}{2},j}$, and where $l_{i+\frac{1}{2},j}$ denotes the length of $\partial\Omega_{i+\frac{1}{2},j}$.

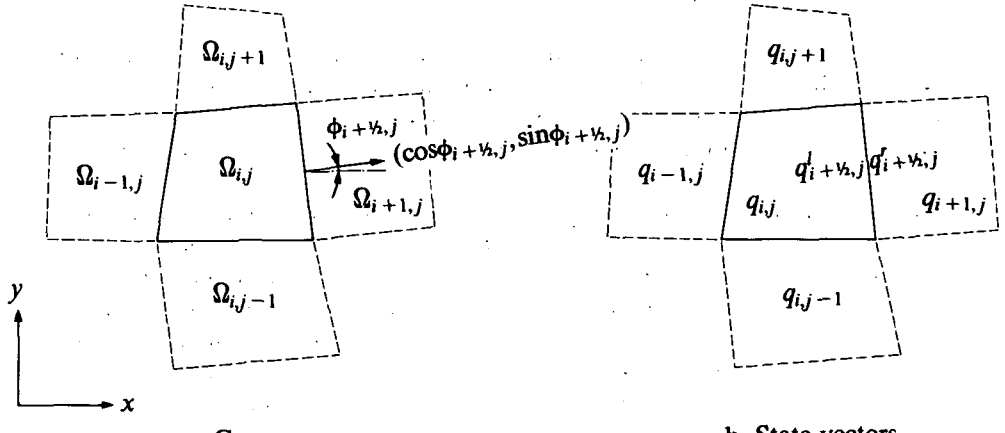

a. Geometry. b. State vectors.

Fig. 1.2. Finite volume $\Omega_{i,j}$ and neighbours.

By following the Godunov approach, the flux evaluation is identical to the numerical solution of a one-dimensional Riemann problem. For this, Hemker and Spekreijse apply an approximate Riemann solver. From the various

approximate Riemann solvers available [27,7,31,26,15,20], they have chosen Osher's scheme, reasons being (i) its continuous differentiability, and (ii) its consistent and likewise continuously differentiable treatment of boundary conditions. Despite its good differentiability properties, Osher's original scheme (O-variant [9]) is not very suitable for efficient implementation. Hemker and Spekreijse significantly improved this by reversing its wave path ordering (P-variant [9]). Further, more or less standard, they conceive the fluxes as functions of u,v,c and $z \equiv \ln(p\rho^{-\gamma})$, leading to simple algebraic relations for the Riemann invariants.

The choice of the left and right states, such as $q^l_{i+\frac{1}{2},j}$ and $q^r_{i+\frac{1}{2},j}$, determines the accuracy of the discretization. First-order accuracy is obtained by simply taking

$$q^l_{i+\frac{1}{2},j} = q_{i,j}, \tag{1.16a}$$

$$q^r_{i+\frac{1}{2},j} = q_{i+1,j}, \tag{1.16b}$$

where $q_{i,j}$ and $q_{i+1,j}$ are the cell-centered states in $\Omega_{i,j}$ and $\Omega_{i+1,j}$, respectively. In spite of its suitability for multigrid, two severe drawbacks of the first-order accurate discretization are (i) its need for relatively fine grids in smooth flow regions, and (ii) its strong smearing of discontinuities that are not aligned with the grid. As a remedy against both drawbacks, a higher-order accurate discretization can be used. Higher-order accuracy can be obtained with e.g. the κ-schemes introduced by Van Leer [16],

$$q^l_{i+\frac{1}{2},j} = q_{i,j} + \frac{1+\kappa}{4}(q_{i+1,j} - q_{i,j}) + \frac{1-\kappa}{4}(q_{i,j} - q_{i-1,j}), \tag{1.17a}$$

$$q^r_{i+\frac{1}{2},j} = q_{i+1,j} + \frac{1+\kappa}{4}(q_{i,j} - q_{i+1,j}) + \frac{1-\kappa}{4}(q_{i+1,j} - q_{i+2,j}), \tag{1.17b}$$

with $\kappa \in [-1,1]$. For $\kappa = -1$, $\kappa = 0$ and $\kappa = 1$, we have the one-sided scheme, the Fromm scheme and the centred scheme, respectively. Spurious non-monotonicity (wiggles) that may arise when using these κ-schemes, can be suppressed, maintaining the global accuracy, by applying a limiter [33,28].

Multigrid method. As the smoothing technique for the first-order discretized Euler equations, Hemker and Spekreijse apply collective symmetric point Gauss-Seidel relaxation. *Point* refers to the property that during the update of the state vector $q_{i,j}$ all other state vectors are kept fixed. *Collective* refers to the property that the update of $q_{i,j}$ is done for all of its four components simultaneously. Further, *symmetric* means that after a relaxation sweep, i.e. after an update of all state vectors $q_{i,j}$, a new sweep in the reverse direction is made. At each volume visited during a relaxation sweep the system of four nonlinear equations, (1.15), is approximately solved by (exact) Newton iteration, the differential operator applied being $(\partial/\partial u, \partial/\partial v, \partial/\partial c, \partial/\partial z)^T$. The most efficient relaxation is obtained by selecting a large tolerance for the Newton iteration so that in all but exceptional cases only a single Newton step is needed. All derivatives that are needed for the relaxation method are clearly

listed in [29]. The relaxation method mentioned is simple and robust, and for the first-order upwind discretized equations considered, it has good smoothing properties.

For the multigrid acceleration Hemker and Spekreijse apply the nonlinear approach preceded by nested iteration. To apply multigrid they construct a nested set of grids such that each finite volume on a coarse grid is the union of 2×2 volumes on the next finer grid (Fig. 1.3).

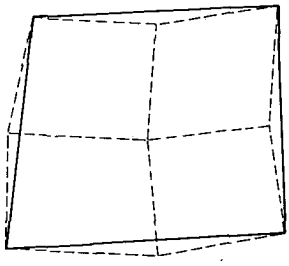

Fig. 1.3. Coarse grid volume and corresponding fine grid volumes.

Let $\Omega_1,...,\Omega_{l-1},\Omega_l,\Omega_{l+1},...,\Omega_L$ be a sequence of such nested grids, with Ω_1 the coarsest and Ω_L the finest grid. Then, nested iteration is applied to obtain a good initial solution on Ω_L, whereas nonlinear multigrid is applied to converge q_L. The first iterate for the nonlinear multigrid cycling is the solution obtained by nested iteration. We proceed to discuss both stages in more detail.

The nested iteration starts with a user-defined initial estimate of q_1, the solution on the coarsest grid. To obtain an initial solution on a finer grid Ω_{l+1}, first the solution on the coarser grid Ω_l is improved by a single nonlinear multigrid cycle. Hereafter, this solution is prolongated to the finer grid Ω_{l+1}. These steps are repeated until the highest level (finest grid) has been reached. On a grid Ω_l with an even number of volumes in both the i- and j-direction, the prolongation used to obtain the initial solution on a next finer grid is bilinear (if not mentioned otherwise). For this purpose the grid Ω_l is subdivided into disjunct sets of 2×2 volumes, and the four state vectors corresponding with each set are interpolated in a bilinear way. Since each volume of Ω_l overlaps 2×2 volumes of Ω_{l+1}, 4×4 new state vectors are obtained on Ω_{l+1}.

Let $N_l(q_l)=0$ denote the nonlinear system of first-order discretized equations at Ω_l, then a single nonlinear multigrid cycle is recurrently defined by the following steps:

(i) Improve on Ω_l the latest obtained solution q_l by application of p pre-relaxation sweeps.

(ii) Compute on the next coarser grid Ω_{l-1} the right-hand side $r_{l-1}=N_{l-1}(q_{l-1})-I_l^{l-1}N_l(q_l)$, where I_l^{l-1} is a restriction operator for right-hand sides.

(iii) Approximate the solution of $N_{l-1}(q_{l-1})=r_{l-1}$ by the application of σ nonlinear multigrid cycles. Denote the approximation obtained as $\tilde{q}_{l-1}$.
(iv) Correct the current solution by: $q_l=q_l+\tilde{I}_{l-1}^{l}(\tilde{q}_{l-1}-q_{l-1})$, where $\tilde{I}_{l-1}^{l}$ is a prolongation operator for solutions.
(v) Improve again q_l by application of q post-relaxations.

Steps (ii),(iii) and (iv) form the so-called coarse grid correction. (These three steps are skipped on the coarsest grid.) The efficiency of a coarse grid correction depends in general on the coarseness of the coarsest grid. (In general it holds: the coarser the coarsest grid, the better the efficiency.) The restriction operator I_l^{l-1} and the prolongation operator $\tilde{I}_{l-1}^{l}$ are defined by

$$(r_{l-1})_{i,j} = (I_l^{l-1}r_l)_{i,j} \equiv (r_l)_{2i,2j}+(r_l)_{2i-1,2j}+ (r_l)_{2i,2j-1}+(r_l)_{2i-1,2j-1}, \tag{1.18a}$$

$$(\tilde{I}_{l-1}^{l}q_{l-1})_{2i,2j} = (\tilde{I}_{l-1}^{l}q_{l-1})_{2i-1,2j} = (\tilde{I}_{l-1}^{l}q_{l-1})_{2i,2j-1} = (\tilde{I}_{l-1}^{l}q_{l-1})_{2i-1,2j-1} \equiv (q_{l-1})_{i,j}. \tag{1.18b}$$

Defining the grid transfer operators in this way, it can be verified that

$$N_{l-1}(q_{l-1}) = I_l^{l-1}N_l(\tilde{I}_{l-1}^{l}q_{l-1}), \tag{1.19}$$

i.e. a coarse grid discretization of the Euler equations is a Galerkin approximation of the discretization on the next finer grid. This implies that the coarse grid correction efficiently reduces the short-wave-length components in the defect. If not mentioned otherwise, as values for σ, and p and q we use at all levels l: $\sigma=1$, and $p=q=1$; i.e. as nonlinear multigrid cycles we use V-cycles with one pre- and one post-relaxation per level.

In Fig. 1.4 an illustration is given of the structure of the multigrid method. A five-level multigrid schedule is considered. Between each pair AB, we have a nonlinear multigrid cycle (V-cycle). In the nested iteration stage, between each pair BA we have the bilinear prolongation of the solution.

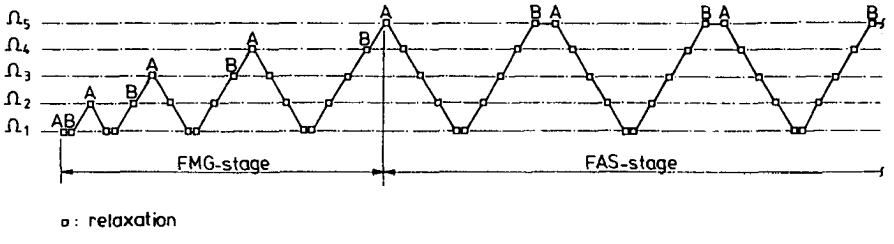

Fig. 1.4. Example schedule of nonlinear multigrid iteration.

Defect correction method. For higher-order discretizations the good smoothing properties are lost. The cause of this difference with the first-order discretized equations is the fact that the system of first-order equations is always weakly diagonally dominant, whereas the system of higher-order discretized equations is not. A standard method for improving the solvability would be to explicitly add some artificial diffusion. But, of course, adding artificial diffusion reduces the accuracy. Further, adding the proper amount of diffusion may require much trial and error. To avoid both, Hemker [8] suggested to solve the system of higher-order discretized equations as they stand by iterative defect correction (IDeC). This implies the repeated solution of the diagonally dominant first-order system with the target operator working via the right-hand side. Though iterative defect correction is well-developed as far as the mathematical concept is concerned [1], it is still under-developed with respect to applications. Given the availability of efficient inner solution method(s), the efficiency of a method with defect correction as outer iteration may be hard to beat. Denoting the higher-order target operator by N_L^+, defect correction iteration reads

$$N_L(q_L^{n+1}) = N_L(q_L^n) - N_L^+(q_L^n), \quad n = 0,1,...,N, \tag{1.20}$$

with the superscript n denoting the iteration counter. With a second-order accurate N_L^+ and a sufficiently smooth problem, already q_L^1 will be second-order accurate, the requirement being that q_L^0 is a sufficiently converged first-order accurate solution [6]. In general it is sufficient to take for q_L^0 the solution obtained by nested iteration followed by a single nonlinear multigrid cycle. The consequence of defect correction cycling for the inner nonlinear multigrid cycling is that all its right-hand sides are extended with the right-hand side from (1.20), and restrictions of that. For a five-level schedule, in Fig. 1.5 we give an illustration of a complete process, assuming that only one nonlinear multigrid cycle is applied per defect correction cycle. In the defect correction stage, between each pair *BA* we have the computation of the right-hand side in (1.20).

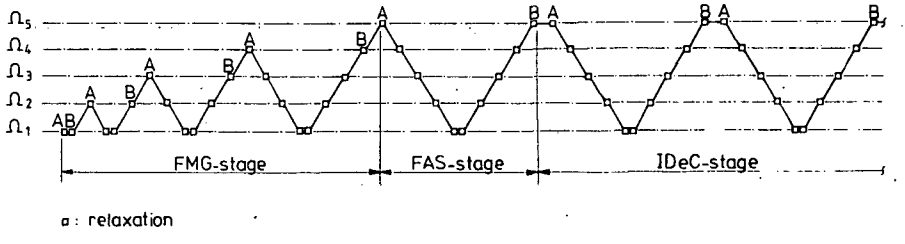

Fig. 1.5. Example schedule of defect correction iteration.

1.6. Concluding remarks

The present-day technological relevance of theoretical fluid dynamics can be attributed to a large extent to the gradually built-up confidence in the Navier-Stokes equations for the wide class of fluid flows for which they were derived one-and-a-half century ago.

Integration of the full Navier-Stokes equations has become reality with the rise of the digital computer. Yet, for the full Navier-Stokes equations (still) no ultimate numerical method exists. Many methods are available, all differing in accuracy and efficiency, mostly either accurate but inefficient, or inaccurate but efficient. In the chapters to follow a new member will be added to the family of numerical Navier-Stokes methods, a method which finds some compromise between the conflicting properties of accuracy and efficiency. For this purpose the Hemker-Spekreijse method is taken as a point of departure, a method which seems apt to an accurate and efficient computation of Euler flows over a wide range of practical interest.

References

1. K. Böhmer, P.W. Hemker and H.J. Stetter, *The Defect Correction Approach,* Comput. Suppl. 5, 1-32 (1984).
2. K. Brand, M. Lemke and J. Linden, *Multigrid Bibliography,* in Multigrid Methods, Frontiers in Applied Mathematics Vol. 3, 189-230, edited by S.F. McCormick (SIAM, Philadelphia, 1987).
3. E. Dick, *A Multigrid Method for Steady Euler Equations, based on Flux-Difference Splitting with respect to Primitive Variables,* in Robust Multi-Grid Methods, Proceedings of the Fourth GAMM-Seminar, Kiel, 1988, Notes on Numerical Fluid Mechanics Vol. 23, 69-85, edited by W. Hackbusch (Vieweg, Braunschweig, 1988).
4. L. Euler, *De Principiis Motus Fluidorum,* Novi Comm. Acad. Petrop. 14, 1 (1759).
5. S.K. Godunov, *Finite Difference Method for Numerical Computation of Discontinuous Solutions of the Equations of Fluid Dynamics,* (Cornell Aeronautical Lab. Transl. from the Russian) Math. Sbornik 47, 271-306 (1959).
6. W. Hackbusch, *Multi-Grid Methods and Applications* (Springer, Berlin, 1985).
7. A. Harten and P.D. Lax, *A Random Choice Finite-Difference Scheme for Hyperbolic Conservation Laws,* SIAM J. Numer. Anal. 18, 289-315 (1981).
8. P.W. Hemker, *Defect Correction and Higher Order Schemes for the Multi Grid Solution of the Steady Euler Equations,* in Multigrid Methods II, Proceedings of the Second European Conference on Multigrid Methods, Cologne, 1985, Lecture Notes in Mathematics Vol. 1228, 149-165, edited by W. Hackbusch and U. Trottenberg (Springer, Berlin, 1986).
9. P.W. Hemker and S.P. Spekreijse, *Multiple Grid and Osher's Scheme for the Efficient Solution of the Steady Euler Equations,* Appl. Numer. Math. 2, 475-493 (1986).

10. A. JAMESON, *Solution of the Euler Equations for Two Dimensional Transonic Flow by a Multigrid Method,* Appl. Math. Comput. 13, 327-355 (1983).
11. D.C. JESPERSEN, *Design and Implementation of a Multigrid Code for the Euler Equations,* Appl. Math. Comput. 13, 357-374 (1983).
12. M.-H. LALLEMAND, *Schémas Décentrés Multigrilles pour la Résolution des Equations d'Euler en Eléments Finis,* Thèse de Docteur, Université de Provence, Centre Saint Charles (Institut National de Recherche en Informatique et en Automatique, Sophia-Antipolis, 1988).
13. H. LAMB, *Hydrodynamics* (Cambridge University Press, Cambridge, 1932).
14. P.D. LAX, *Hyperbolic Systems of Conservation Laws II,* Comm. Pure Appl. Math. 10, 537-566 (1957).
15. B. VAN LEER, *Flux-Vector Splitting for the Euler Equations,* in Proceedings of the Eighth International Conference on Numerical Methods in Fluid Dynamics, Aachen, 1982, Lecture Notes in Physics Vol. 170, 507-512, edited by E. Krause (Springer, Berlin, 1982).
16. B. VAN LEER, *Upwind-Difference Methods for Aerodynamic Problems governed by the Euler Equations,* in Large Scale Computations in Fluid Mechanics, Proceedings of the 15th AMS-SIAM Summer Seminar on Applied Mathematics, Scripps Institution of Oceanography, 1983, Lectures in Applied Mathematics Vol. 22, Part 2, 327-336, edited by B.E. Engquist et al. (Amer. Math. Soc., Providence, RI, 1985).
17. W.A. MULDER, *Multigrid Relaxation for the Euler Equations,* J. Comput. Phys. 60, 235-252 (1985).
18. C.L.M.H. NAVIER, *Mémoire sur les Lois du Mouvement des Fluides,* Mém. de l'Acad. des Sciences 6, 389 (1822).
19. R.-H. NI, *A Multiple-Grid Scheme for Solving the Euler Equations,* AIAA J. 20, 1565-1571 (1982).
20. S. OSHER AND F. SOLOMON, *Upwind Difference Schemes for Hyperbolic Systems of Conservation Laws,* Math. Comput. 38, 339-374 (1982).
21. L. PRANDTL, *Über Flüssigkeitsbewegung bei Sehr Kleiner Reibung,* in Verhandlungen des Dritten Internationalen Mathematiker-Kongresses, Heidelberg, 1904 (Leipzig, 1905).
22. L. PRANDTL AND O.G. TIETJENS, *Fundamentals of Hydro- and Aeromechanics* (McGraw-Hill, New York, 1934).
23. L. PRANDTL AND O.G. TIETJENS, *Applied Hydro- and Aeromechanics* (McGraw-Hill, New York, 1934).
24. R.D. RICHTMYER AND K.W. MORTON, *Difference Methods for Initial-Value Problems* (Wiley, New York, 1967).
25. P.J. ROACHE, *Computational Fluid Dynamics* (Hermosa, Albuquerque, 1976).
26. P.L. ROE, *Approximate Riemann Solvers, Parameter Vectors, and Difference Schemes,* J. Comput. Phys. 43, 357-372 (1981).
27. V.V. RUSANOV, *The Calculation of the Interaction of Non-Stationary Shock Waves and Obstacles,* USSR Comput. Math. and Math. Phys. 1, 304-320 (1962).

28. S.P. SPEKREIJSE, *Multigrid Solution of Monotone Second-Order Discretizations of Hyperbolic Conservation Laws,* Math. Comput. 49, 135-155 (1987).
29. S.P. SPEKREIJSE, *Multigrid Solution of the Steady Euler Equations,* CWI-tract 46 (Centre for Mathematics and Computer Science, Amsterdam, 1988).
30. J.L. STEGER, *A Preliminary Study of Relaxation Methods for the Inviscid Conservative Gasdynamics Equations using Flux Splitting,* NASA-CR-3415 (unpublished, 1981).
31. J.L. STEGER AND R.F. WARMING, *Flux Vector Splitting of the Inviscid Gasdynamic Equations with Application to Finite-Difference Methods,* J. Comput. Phys. 40, 263-293 (1981).
32. G.G. STOKES, *On the Theories of the Internal Friction of Fluids in Motion, and of the Equilibrium and Motion of Elastic Solids,* Trans. Cambr. Phil. Soc. 8, 287 (1845).
33. P.K. SWEBY, *High Resolution Schemes using Flux Limiters for Hyperbolic Conservation Laws,* SIAM J. Numer. Anal. 21, 995-1011 (1984).

Chapter 2

Numerical Results for the Steady Euler Equations

2.1. Introductory remarks

In this chapter we examine the practical interest of the Hemker-Spekreijse method, and investigate the possibilities of extending it with e.g. grid adaptation and τ-extrapolation. For this we consider successively an internal, simply-connected geometry (a wind tunnel section) and some external, multiply-connected geometries (two mono-airfoils and a bi-airfoil). In all cases, the perfect gas to be considered is di-atomic; $\gamma = 1.4$. The wind tunnel flow and airfoil flow results to be presented here have been (or are near being) published in [16,17,29] and [10,12,15,19,20], respectively. The present chapter gives a synoptic account of these papers.

2.2. Transonic wind tunnel flow

2.2.1. Purpose

An important physical feature for the design of transonic airfoils is the interaction between the possible shock wave(s) at the airfoil and the boundary layers along the airfoil. In transonic aerodynamics a lot of work, both experimental and theoretical, is devoted to this so-called transonic shock wave - boundary layer interaction. At the Delft University of Technology, Faculty of Aerospace Engineering, a transonic wind tunnel section has been designed and constructed [28] for performing measurements on this phenomenon [29]. Limited accessibility to the flow in the wind tunnel section inhibits measurements throughout the entire flow field. However, knowledge of the entire flow field is important for redesign purposes. This situation motivated a computation of the entire flow field.

As a suitable flow model the steady, two-dimensional Euler equations have been chosen, the motivation being that, in the first instance, only inviscid flow solutions with (possibly occurring) rotation are of interest. The use of a steady flow model is motivated by the fact that the main flow in the wind tunnel section is steady. Further, the use of a two-dimensional model is motivated by the fact that, besides a curved lower and upper wall, the wind tunnel section has flat, parallel side walls.

2.2.2. Grid adaptation

In Fig. 2.1 graphs are given of the wind tunnel section considered. In Fig. 2.1a a graph is given of the complete computational domain. It shows a flat, parallel inflow part, followed by a slender curved part up to the outlet. In Fig. 2.1b a photograph is given of the test section in an opened wind tunnel. Notice that the present geometry deviates significantly more from 'completely flat and parallel' than the geometry of the standard channel flow from [32], the latter being almost suited for small perturbation approaches.

In order to obtain a good resolution of some interesting, large local gradients, we use stretched grids (Fig. 2.2). The following stretching relations are used for the x-coordinates of the vertical grid lines:

$$x_i = x_{shock} + (x_{in} - x_{shock}) \frac{e^{c_{x_1} \frac{n_{x_1} - i}{n_{x_1}}} - 1}{e^{c_{x_1}} - 1}, \quad i = 0, 1, ..., n_{x_1}, \tag{2.1a}$$

$$x_i = x_{shock} + (x_{out} - x_{shock}) \frac{e^{c_{x_2} \frac{i - n_{x_1}}{n_{x_2}}} - 1}{e^{c_{x_2}} - 1}, \quad i = n_{x_1} + 1, n_{x_1} + 2, ..., n_{x_1} + n_{x_2}. \tag{2.1b}$$

Here, the known coordinate x_{shock} (Fig. 2.2) denotes the x-coordinate of the vertical grid line which is supposed to lie in the foot of the possibly occurring shock wave. The known x_{in} and x_{out} correspond with the vertical grid line at the in- and outlet, respectively. The unknown (positive) constants c_{x_1} and c_{x_2} determine the stretching up- and downstream of x_{shock}, respectively, whereas the known n_{x_1} and n_{x_2} denote the number of volumes in x-direction, up- and downstream of x_{shock}, respectively. For the y-coordinates of the volume vertices the following stretching relation is applied:

$$y_j(x) = y_{low}(x) + (y_{up}(x) - y_{low}(x)) \frac{e^{c_y \frac{j}{n_y}} - 1}{e^{c_y} - 1}, \quad j = 0, 1, ..., n_y. \tag{2.2}$$

Here, the known $y_{low}(x)$ and the known $y_{up}(x)$ correspond with the lower and upper wall, respectively. The unknown (positive) constant c_y determines the stretching in y-direction, and the known n_y denotes the total number of volumes in y-direction. (The y-distribution of the lower and upper wall, $y_{low}(x)$ and $y_{up}(x)$, are known from accurate measurements at discrete x-positions and, consecutively, cubic spline interpolation.)

To find a satisfactory value for c_{x_1}, c_{x_2} and c_y we impose the following stretching requirements:

$$\frac{x_i - x_{i-1}}{x_{i+1} - x_i} \leqslant 1 + \delta, \quad i = 1, 2, ..., n_{x_1} - 1, \tag{2.3a}$$

$$\frac{x_{i+1} - x_i}{x_i - x_{i-1}} \leqslant 1 + \delta, \quad i = n_{x_1} + 1, n_{x_1} + 2, ..., n_{x_1} + n_{x_2} - 1, \tag{2.3b}$$

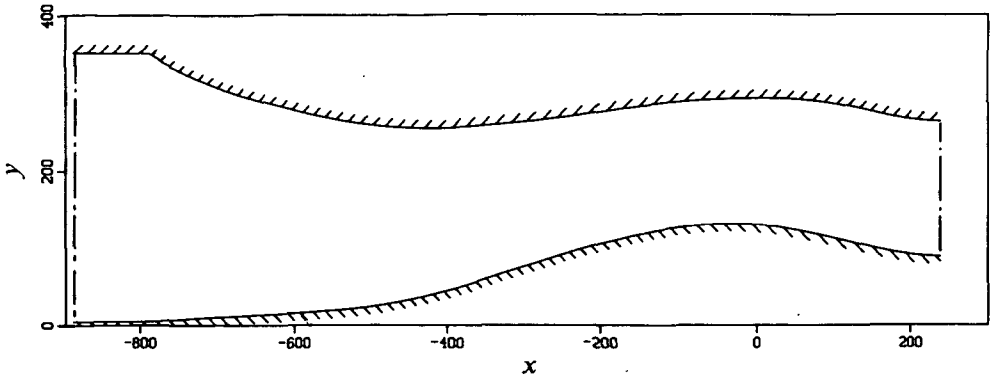

a. Complete computational domain.

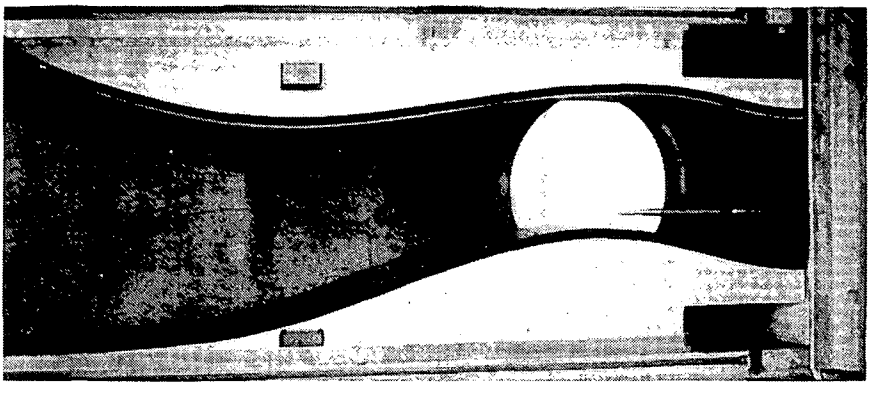

b. Test section in opened wind tunnel.

Fig. 2.1. Wind tunnel section.

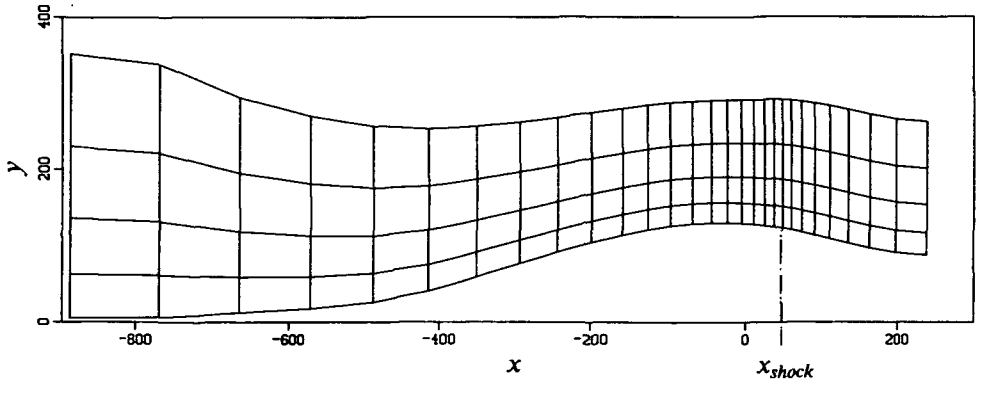

Fig. 2.2. Stretched grid.

and

$$\frac{y_{j+1}(x)-y_j(x)}{y_j(x)-y_{j-1}(x)} \leqslant 1+\delta, \quad j=1,2,...,n_y-1, \quad x_{in} \leqslant x \leqslant x_{out}, \tag{2.4}$$

with δ some positive constant. The smoothness requirements (2.3) and (2.4) are imposed now for the coarsest grid only (with $\delta=1$). Further, for the finest grid we impose the following matching requirement:

$$\frac{x_{i+1}-x_i}{x_i-x_{i-1}} = 1, \quad x_i = x_{shock}. \tag{2.5}$$

The value of x_{shock} is adapted during the solution process. It is initialized to the x-location of the wind tunnel throat, and is adapted to the shock location during the nested iteration stage. The grid adaptation is simple. First, after each solution prolongation in the nested iteration stage, a search is made for the x-location of the maximum velocity gradient at the lower wall, downstream of the throat. This location is assigned to x_{shock}. Hereafter, we generate the new grids. Without any correction, the states $q_{i,j}$ are shifted together with the volumes $\Omega_{i,j}$. In doing this, the quality of the finest-grid solution as yielded by the nested iteration becomes worse. However, no significant deterioration of convergence rates is observed. (The grid adaptation has no other effect than that what it is meant for: to reduce the mesh size at the possible shock wave, in order to make it sharper.)

2.2.3. *Boundary conditions*

Different boundary conditions considered. The boundary condition treatment must be correct both mathematically and physically. Mathematics prescribes how many conditions must be imposed at a boundary; physics prescribes what conditions should be imposed. The number of conditions to be imposed at a boundary depends on the type of flow at that boundary. Types of flow to be considered here (and the corresponding number of boundary conditions to be imposed) are: (i) subsonic inflow (three), (ii) subsonic outflow (one), and (iii) impermeable walls (one). For our wind tunnel section, the following conditions are imposed.

At the impermeable upper and lower wall, the boundary condition is trivial: a zero normal velocity component.

At the inlet, uniformly constant distributions $u=u_{in}$, $v=0$ and $c=1$ are imposed. These simple distributions are motivated by the fact that the inlet part is flat and parallel. The one-dimensional flow theory value, given a sonic throat, is taken as a subsonic value for u_{in}.

Because of the fact that the outlet part is non-flat and non-parallel, the boundary condition at the outlet cannot be as trivial as those at the inlet. The following possibilities are considered: (i) $h=h_{in}$ is uniformly constant, with h denoting the total enthalpy $h=c^2/(\gamma-1)+\frac{1}{2}(u^2+v^2)$; (ii) $v/u=\theta(y)$; (iii) $u=u(y)$; and (iv) $p=p(y)$.

The first possibility is motivated by the fact that with a known uniformly constant distribution of u,v and c at the inlet (i.e. with a known uniformly constant total enthalpy at the inlet), this boundary condition requires no knowledge of the non-uniform outlet flow. This because of the fact that for steady adiabatic Euler flows, with the total enthalpy at the upstream boundary known to be constant, only three differential equations describe the flow. The energy equation in its differential form may be replaced by the relation $c^2/(\gamma-1)+\frac{1}{2}(u^2+v^2)=h_{in}$ throughout the entire flow field. The present Euler code solves the full non-isenthalpic Euler equations. The simplifying property mentioned is not exploited in order to allow the computation of flows such as that through a propeller disk (section 2.3.4), and in particular to allow a rapid extension to a Navier-Stokes code (chapter 3). The second possibility, with the flow direction specified, is motivated by its simplicity. A linear distribution of $\theta(y)$ is assumed, using the known flow direction at the lower and upper wall. The third possibility is also motivated by its simplicity. For this possibility, we assume the outlet flow to be a potential vortex flow. The relation $u(y)r(y)=\psi_{out}$ is applied, with ψ_{out} uniformly constant and $r(y)$ the distribution of the radii of curvature of the streamlines. A linear distribution for the streamline curvature $1/r(y)$ is assumed, using the known curvature of the lower and upper wall. The value following from the one-dimensional flow theory, given a sonic throat and a transonic outflow with a shock of known constant strength, is taken as a value for ψ_{out}. A disadvantage of this boundary condition is its inconsistency in the case of a flow with shock wave of variable strength, which is what we have here. (It is a boundary condition which is consistent in a potential flow model, but not in the Eulerian rotational flow model.) For the fourth possibility we use the equation of curvilinear motion

$$\frac{dp(y)}{dy} = \gamma \frac{p(y)M^2(y)}{r(y)} \cos\phi(y), \tag{2.6}$$

with $M(y)$ the Mach number distribution and $\phi(y)$ the distribution of the angles between the streamlines and the x-axis. For $1/r(y)$ and $\phi(y)$ linear distributions are assumed again, such that the flow fits the channel outlet. $M(y)$ is taken uniformly constant. Its value is determined from the one-dimensional flow theory, again given a sonic throat and a transonic outflow with a shock of known constant strength. Using the corresponding value of p as value for p at the lower wall, an initial value problem is obtained, which is solved by means of a Runge-Kutta-Merson method. In the following, the well-posedness of each of these four outlet boundary conditions is investigated. There a choice is made for the outlet boundary condition to be applied.

Well-posedness subsonic outlet boundary conditions. Generally speaking, mathematically well-posed conditions to be imposed at a boundary are conditions for which the state at that boundary can be completed accurately. At a subsonic outlet, the boundary condition must fix the single degree of freedom existing over there. A subsonic outlet boundary condition can be represented as a three-dimensional surface in a four-dimensional state space. The smaller the angle α between the normal at this surface and the eigenvector corresponding to the negative eigenvalue of the Jacobian, $u-c$, the better the quality of the outlet boundary condition.

Considering the (ρ,u,v,e)-space as state space, the eigenvector corresponding with the eigenvalue $u-c$ is $r=(\rho,-c,0,c(c/\gamma-u))^T$. For h, v/u, u and p specified, respectively, the three-dimensional surface mentioned, say $B(q)$, is described by

$$B(q) = \gamma e - \frac{\gamma-1}{2}(u^2+v^2) = h_B, \tag{2.7a}$$

$$B(q) = \frac{v}{u} = \theta_B, \tag{2.7b}$$

$$B(q) = u = u_B, \tag{2.7c}$$

$$B(q) = (\gamma-1)\rho(e-\tfrac{1}{2}(u^2+v^2)) = p_B, \tag{2.7d}$$

with h_B, θ_B, u_B and p_B constant. For the angle α it holds that $\cos\alpha \propto \nabla B.r$, with $\nabla=(\partial/\partial\rho,\ \partial/\partial u,\ \partial/\partial v,\ \partial/\partial e)^T$. For h, v/u, u and p specified, respectively, we find then

$$\nabla B.r = c(c-u), \tag{2.8a}$$

$$\nabla B.r = -\frac{v}{u}\frac{c}{u}, \tag{2.8b}$$

$$\nabla B.r = -c, \tag{2.8c}$$

$$\nabla B.r = \gamma p. \tag{2.8d}$$

From (2.8a) and (2.8b) it can be seen that for h and v/u specified, the vectors ∇B and r become orthogonal for $u\to c$ and $v\to 0$, respectively. The consequence of a nearly orthogonal ∇B and r is that a small change in either the boundary condition or the state inside the computational domain near the outlet, may cause a large change in the boundary state and hence in the flux across the outlet. For a given state $q_0=(u_0,\ v_0,\ c_0,\ z_0)^T$ near the outlet, and the boundary conditions specified by (2.7a)-(2.7d), respectively, the effect of a small perturbation in q_0 can be shown exactly. The state at the outlet which corresponds with q_0 is $q=(u,\ v_0,\ c,\ z_0)^T$, with for boundary condition (2.7a)-(2.7d), respectively

$$c = \frac{\gamma-1}{\gamma+1}\left[u_0+\frac{2}{\gamma-1}c_0+\sqrt{(\gamma+1)(h_B-\tfrac{1}{2}v_0^2)-\frac{\gamma-1}{2}(u_0+\frac{2}{\gamma-1}c_0)^2}\right], \tag{2.9a}$$

$$u = \frac{v_0}{\theta_B}, \tag{2.9b}$$

$$u = u_B, \tag{2.9c}$$

$$c = \sqrt{\gamma p_B^{\frac{\gamma-1}{\gamma}} e^{\frac{z_0}{\gamma}}}, \tag{2.9d}$$

and either $u = u_0 + \frac{2}{\gamma-1}(c_0 - c)$ or $c = c_0 + \frac{\gamma-1}{2}(u_0 - u)$ to complete. With $\nabla = (\partial/\partial u_0, \partial/\partial v_0, \partial/\partial c_0, \partial/\partial z_0)^T$ we find for (2.9a)-(2.9d), respectively

$$\nabla c = \frac{\gamma-1}{\gamma+1}(1,0,\frac{2}{\gamma+1},0)^T + \frac{\gamma-1}{\gamma+1}\frac{1}{u-c}(\frac{\gamma-1}{2}u+c, \frac{\gamma+1}{2}v, u+\frac{2}{\gamma-1}c, 0)^T, \quad (2.10a)$$

$$\nabla u = (0,\frac{u}{v},0,0)^T, \quad (2.10b)$$

$$\nabla u = 0, \quad (2.10c)$$

$$\nabla c = (0,0,0,\frac{c}{2\gamma})^T, \quad (2.10d)$$

where we substituted $q = q_0$ into (2.10a) and (2.10b) for simplicity. It can be seen that the gradients (2.10a) and (2.10b) become infinitely large in aforementioned limit cases ($u \to c$ for h specified and $v \to 0$ for v/u specified). Flow computations with h specified and v/u specified show these outlet boundary conditions to be ill-posed indeed. This is not the case with the two other boundary conditions.

Because of its better consistency with the Euler flow model, we prefer the boundary condition with p specified to the one with u specified.

2.2.4. Results

The great slenderness of the wind tunnel section leads to a coarsest grid with a relatively large number of volumes in longitudinal direction. By using the 56×8-grid in Fig. 2.3a as the finest grid and by applying a four-level multigrid schedule, the 7×1-grid in Fig. 2.3d is the coarsest grid. (The dashed lines in Fig. 2.3 indicate the lower and upper wall of the wind tunnel section.) As flow problems we consider a non-choked flow with $M_u = 1.15$, M_u being the Mach number just upstream of the shock wave, and a choked flow with $M_u = 1.37$. As discretization we apply the first-order one only.

Convergence histories obtained for both test cases are given in Fig. 2.4. In both convergence histories, the single-grid history is given as well. The convergence histories are given by graphs of the residual ratio $\Sigma_{k=1}^4 |(N_L(q_L^n))_k| / \Sigma_{k=1}^4 |(N_L(q_L^0))_k|$ versus the number of cycles performed, one multigrid cycle being a V-cycle (with $p = q = 15$ for $l = 1$, and $p = 1$, $q = 3$ for $l > 1$), and one single-grid cycle being the equivalent number of finest-grid relaxation sweeps. $|(N_L(q_L^n))_k|$ denotes the summation - over all finest-grid volumes - of the absolute values of the k-th component in the first-order residuals, with q_L^n denoting the n-th iterate at $\Omega_L = \Omega_4$, the finest grid. The solution q_L^0 is that obtained at the end of the FMG-stage (Fig. 1.4). Though the multigrid convergence rates obtained are not optimal - optimal multigrid only needs a few cycles - they are satisfactory compared with many other solution techniques.

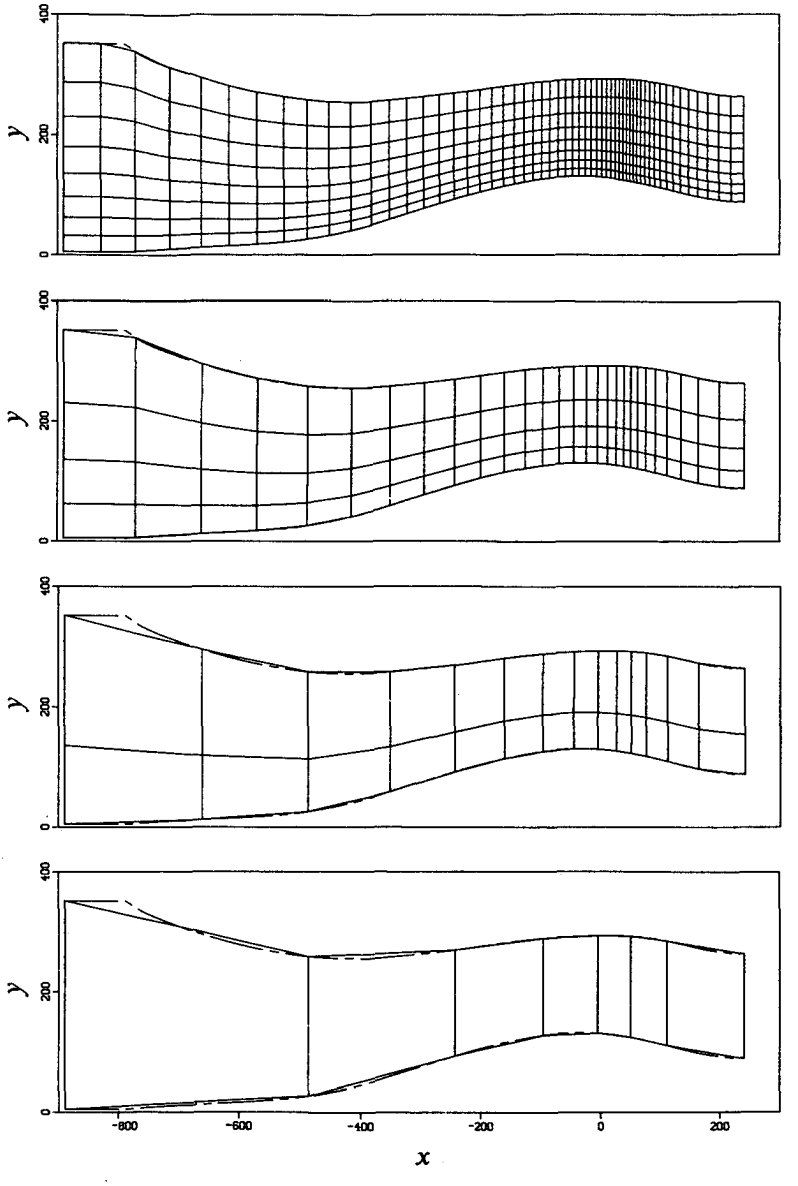

a. 56×8-grid.

b. 28×4-grid.

c. 14×2-grid.

d. 7×1-grid.

Fig. 2.3. Family of grids.

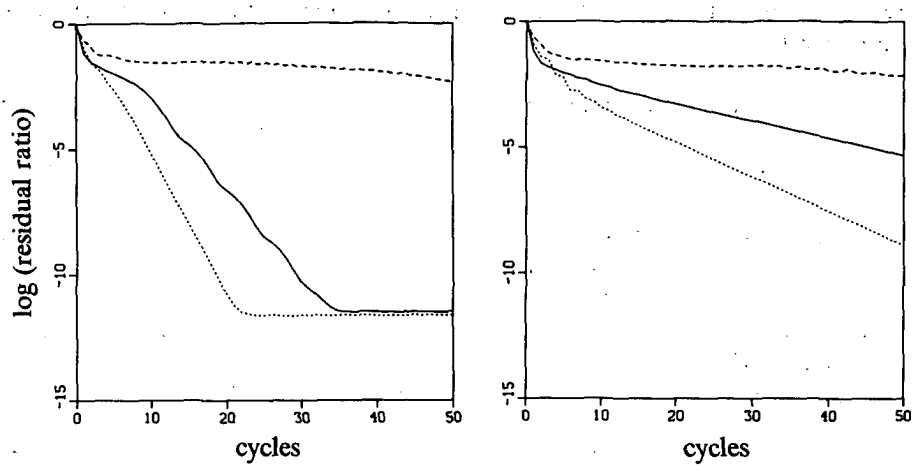

a. $M_u = 1.15$. b. $M_u = 1.37$.

Fig. 2.4. Convergence histories (------ : single-grid Osher, —— : multigrid Osher, ····· : multigrid Van Leer).

In [26], Mulder makes the statement that the present non-optimal multigrid performance is caused by too weak crosswind diffusion inherent in flux difference splitting schemes (such as Osher's [30] applied here) when having a strongly grid-aligned flow. The correctness of this statement is dubious when considering the good multigrid performance presented in [13] for an even more grid-aligned transonic channel flow. To investigate the other statement made in [26] that flux vector splitting schemes (such as Van Leer's [21]) do not suffer from grid-alignment due to their greater crosswind diffusion, to Fig. 2.4 we added the multigrid behaviour obtained with Van Leer's scheme. Though with Van Leer's scheme the multigrid method performs better indeed, its convergence rates are not significantly better than the corresponding ones presented in [13] for the more grid-aligned channel flow computed with Osher's scheme. Our opinion about the non-optimal multigrid-performance simply is that the method suffers from the rather large number of volumes in streamwise direction on the coarsest grid. An optimal acceleration is supposed to be attainable by introducing e.g. a one-dimensional coarse grid correction or a streamwise line relaxation. (The rather large difference in convergence between the choked and non-choked flow is not yet clear. Anyhow, it is not explained by the previous argument about the rather fine coarsest grid.)

Finest grids and lower surface - pressure distributions obtained for $M_u = 1.15$ and $M_u = 1.37$ are shown in Fig. 2.5. (The open markers in the pressure distributions correspond to computed pressures, the full markers to measured pressures.) A very satisfactory agreement is found away from the shock wave. Yet, an important result as the pressure rise across the shock wave at the wall is also predicted in a satisfactory way. The latter indicates that the Euler code may be exploited for designing experimental set-ups like this. From the finest grids and surface distributions obtained, it can be seen that for both flows the grid adaptation is good. Clearly visible for $M_u = 1.37$ is the occurrence of an after-expansion. Since a first-order accurate Osher-type discretization yields solutions without spurious non-monotonicity, the after-expansion occurring for $M_u = 1.37$ is not supposed to be a numerical artefact, but a correct part of the Euler flow solution indeed, namely the Zierep after-expansion [37].

For both the choked and non-choked flow, a comparison is made between the Mach number distributions computed with the Euler code and those obtained by holographic interferometry. In Fig. 2.6 the Mach number distributions are given as computed for the entire test section. In Fig. 2.7 a detail of both distributions is compared with the corresponding interferometric result. It appears that the computational and experimental results show a nice quantitative agreement away (of course) from the wall and shock wave.

The differences between computational and experimental results can also be exploited. Given an Euler code which has proved to be reliable, its results can be considered confidently as experimental results with viscosity and heat conduction switched off. They can be used for identifying simple viscous phenomena and, in particular, complicated viscous-inviscid phenomena.

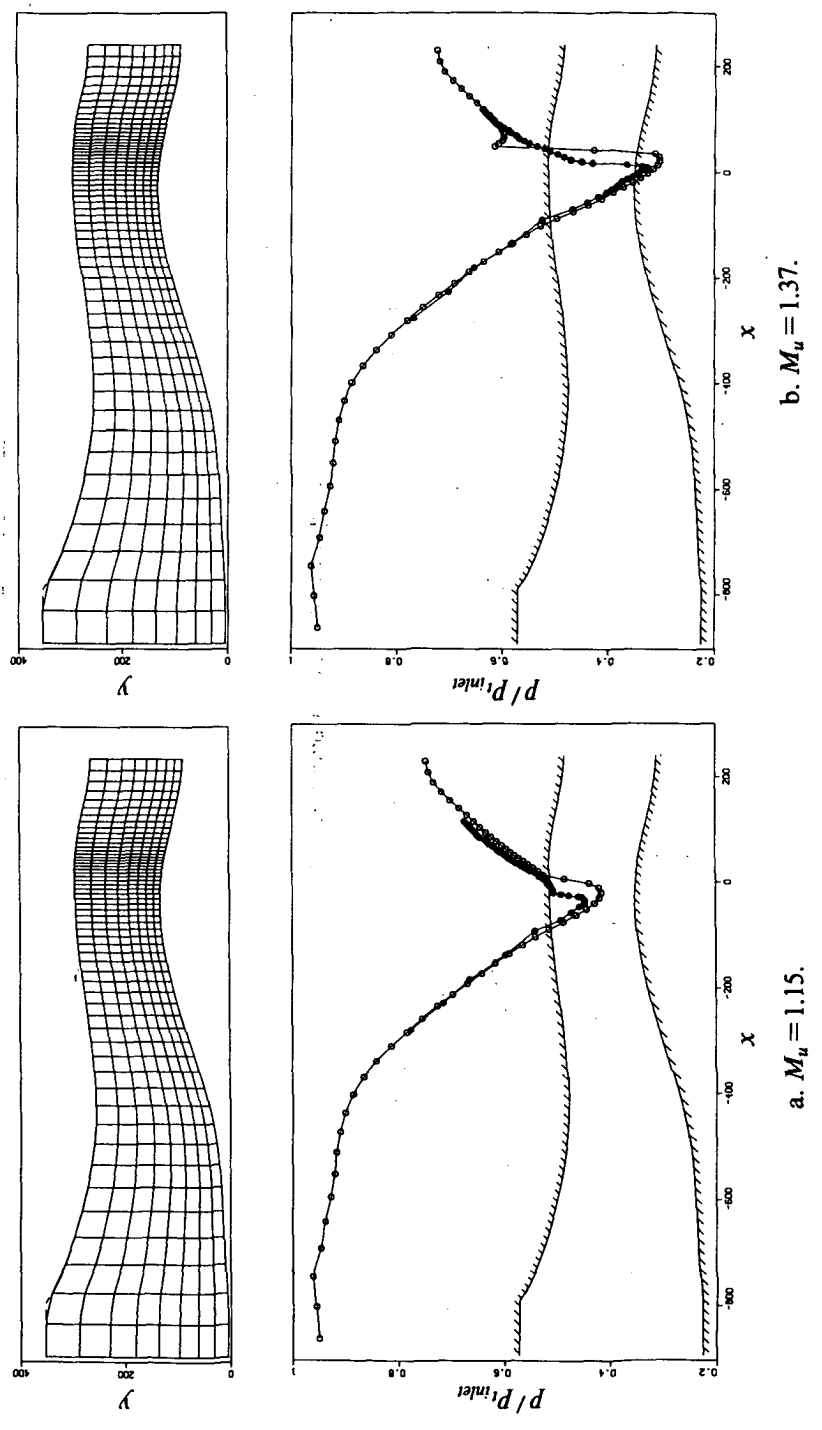

Fig. 2.5. Finest grids and lower surface - pressure distributions
(○ : computed, ● : measured).

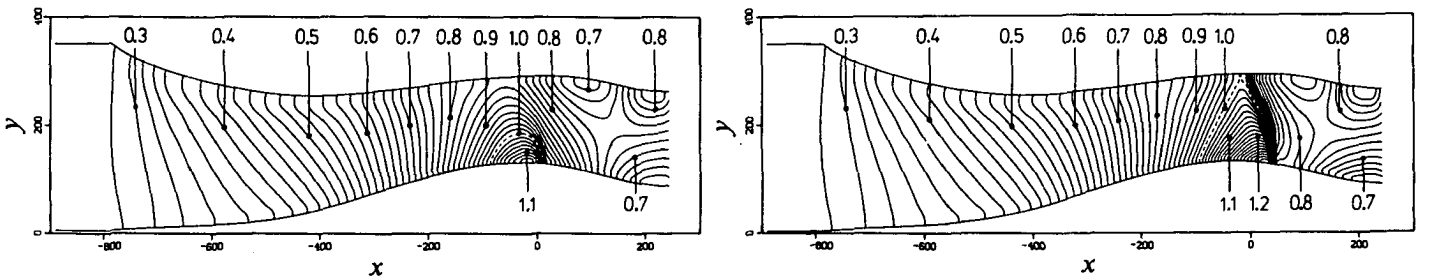

a. $M_u = 1.15$.

b. $M_u = 1.37$.

Fig. 2.6. Mach number distributions.

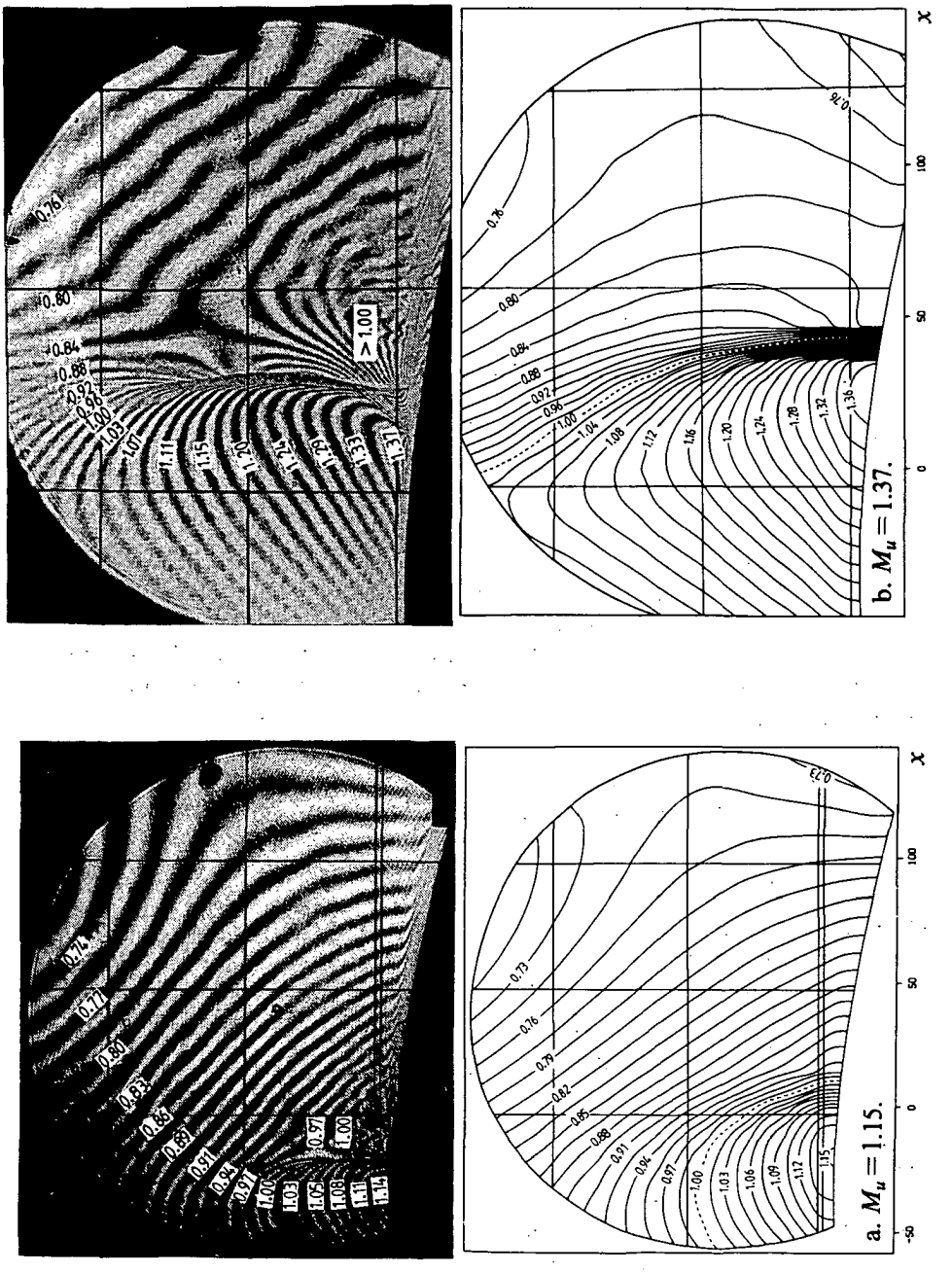

Fig. 2.7. Interferometric and numerical Mach number distributions.

2.3. Subsonic, transonic and supersonic airfoil flow

2.3.1. Purpose

A major difference between simply- and multiply-connected geometries is that multiply-connected geometries admit the generation of slip layers (or contact discontinuities), whereas simply-connected geometries do not. Because of the key role of discontinuities in developing accurate and efficient numerical methods, and because of the fact that for the Euler equations, besides shock waves, only contact discontinuities exist as other type of discontinuities, multiply-connected geometries (such as airfoils) are more interesting than simply-connected geometries (such as the previously considered wind tunnel section). Another important difference between the specific wind tunnel case just considered and the specific airfoil cases to be considered now is that the latter are in majority standard test cases for which reliable reference solutions exist. Because of these two differences, it is useful to examine the Hemker-Spekreijse method to its full extent now. Higher-order discretizations and iterative defect correction will be invoked, and - as an extra possibility - we will consider τ-extrapolation.

2.3.2. Higher-order discretizations

Third-order scheme. As mentioned, a higher-order accurate discretization can be obtained by applying Van Leer's κ-scheme (1.17) with some suitable value of κ, the extreme possibilities being centred ($\kappa=1$) and one-sided ($\kappa=-1$). The precise κ-value chosen influences the upwinding possibilities of the approximate Riemann solver to be applied thereupon (for $\kappa=1$ e.g. all upwinding possibilities are lost) and hence the accuracy and efficiency of the complete numerical method.

From the viewpoint of accuracy, an indication for the optimal value of κ can be quickly obtained by considering the scalar, linear convection equation

$$\frac{\partial u}{\partial x}+\frac{\partial u}{\partial y} = 0. \tag{2.11}$$

On a finite volume grid with cell faces which are equidistant and parallel to the x- and y-axis (Fig. 2.8), an upwind discretization using the κ-scheme yields as modified equation

$$\frac{\partial u}{\partial x}+\frac{\partial u}{\partial y}+h^2\frac{\kappa-\frac{1}{3}}{4}\left(\frac{\partial^3 u}{\partial x^3}+\frac{\partial^3 u}{\partial y^3}\right)+O(h^3) = 0. \tag{2.12}$$

Assuming the reliability of the underlying Taylor series expansions, from (2.12) it follows as the highest-accuracy-value: $\kappa=\frac{1}{3}$, yielding a third-order truncation error.

A disadvantage of this κ-scheme, in fact of any κ-scheme, is that it cannot be applied in a consistent way near boundaries. Near boundaries one has to fall back on e.g. a combination of the centred scheme and the one-sided scheme, which slightly reduces the local accuracy over there. Further, as already mentioned in section 1.5.3, κ-schemes may lead to spatially oscillatory solutions.

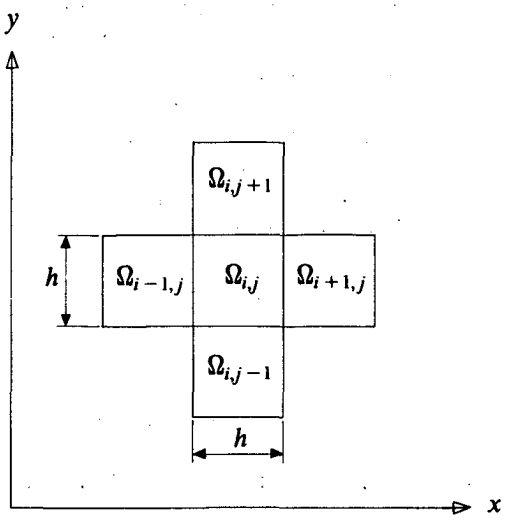

Fig. 2.8. Square model volume $\Omega_{i,j}$ with neighbours.

Superbox scheme. The inconsistency near boundaries can be removed by applying, instead of a κ-scheme, the superbox scheme proposed by Hemker [9]. This scheme is defined on a set of 2×2 finite volumes, a superbox. At the four inner walls of each superbox, it applies the centred κ-scheme, whereas at the eight outer walls it applies the one-sided κ-scheme. (Notice that superboxes do not overlap.) The superbox scheme fits well in our multigrid context with its even number of volumes guaranteed in each coordinate direction of the finest grid. A shortcoming of the scheme is that though it is second-order accurate for each superbox separately (including those along the boundaries), it is lower-order accurate for each single volume separately. However, this shortcoming can be eliminated by post-processing the converged solution in the following simple way. Because of the second-order accuracy per superbox, the lower-order error remaining after convergence consists of the shortest-wave-length component only. This component can be eliminated by computing, in a post-process, the states at the volume vertices as averages over the directly neighbouring volumes.

To suppress possibly occurring wiggles, the superbox scheme cannot be extended with a standard limiter without undoing its consistency. A 2×2-block only is too compact for applying a standard limiter.

Van Albada scheme. As mentioned in section 1.5.3, oscillatory solutions arising with a κ-scheme can be avoided by applying a limiter, without reducing the global accuracy. Though in smooth flow regions a limiter slightly suppresses physically correct minima and maxima, around discontinuities, instead of a possibly highly inaccurate, oscillatory solution, it yields a smooth solution with an accuracy which is in between first-order accuracy and the higher-order target accuracy. With the well-developed limiter theory and limiter functions available now [35,33], to us the only useful information broadcasted by wiggles [7] is that the corresponding solutions are useless for practical purposes (such as lift and drag computations).

Higher-order schemes using limiters can be written as

$$q^{l(k)}_{i+\frac{1}{2},j} = q^{(k)}_{i,j} + \frac{1}{2}\psi(R^{(k)}_{i,j})(q^{(k)}_{i,j} - q^{(k)}_{i-1,j}), \tag{2.13a}$$

$$q^{r(k)}_{i+\frac{1}{2},j} = q^{(k)}_{i+1,j} + \frac{1}{2}\psi(\frac{1}{R^{(k)}_{i+1,j}})(q^{(k)}_{i+1,j} - q^{(k)}_{i+2,j}), \tag{2.13b}$$

with k referring to the k-th state vector component ($k = 1,2,3,4$), with $\psi(R)$ the limiter function, and with

$$R^{(k)}_{i,j} = \frac{q^{(k)}_{i+1,j} - q^{(k)}_{i,j}}{q^{(k)}_{i,j} - q^{(k)}_{i-1,j}}. \tag{2.14}$$

Since limiter functions apply three volume states per left and right state separately, near boundaries one has to fall back on e.g. a superbox-like combination of the plain, centred and one-sided scheme, which may lead to wiggles over there.

For the present airfoil flow computations, we prefer a limiter which is smooth and which renders a scheme at the upstream side of shock waves which resembles the one-sided scheme, a natural scheme in those regions. For this purpose we take the Van Albada limiter [1]

$$\psi(R) = \frac{R^2 + R}{R^2 + 1}. \tag{2.15}$$

An illustration of this limiter in the extended monotonicity domain as introduced by Spekreijse [33] is given in Fig. 2.9. Notice that with the Van Albada limiter, (2.13) can also be interpreted as a modified Fromm ($\kappa = 0$) scheme. (At $R = 1$ it is tangent to the Fromm scheme, Fig. 2.9.) For convenience we will call '(2.13) with (2.15)' the Van Albada scheme.

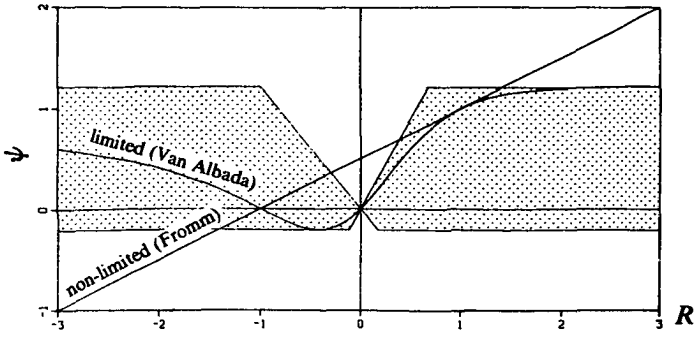

Fig. 2.9. Monotonicity domain with limited and non-limited $\kappa = 0$-scheme.

2.3.3. τ-extrapolation

In a multigrid context, where solutions on more grids are available, it is natural to consider the possibilities of e.g. Richardson extrapolation or τ-extrapolation [4,8] to further improve the accuracy of the solution. For τ-extrapolation it is known that it can profitably be done even in cases where Richardson extrapolation cannot be applied.

The accuracy of a converged higher-order iterate q_L^n of the defect correction process (1.20) can be efficiently boosted further by proceeding with the extended solution process

$$N_L(q_L^{n+1}) = N_L(q_L^n) - (N_L^+(q_L^n) - \tau_L), \quad n = 0,1,...,N, \tag{2.16}$$

with N_L^+ the same higher-order operator as in (1.20), q_L^0 the converged higher-order solution as yielded by (1.20), and τ_L the higher-order truncation error

$$\tau_L \equiv N_L^+(\tilde{I}^L q) - I^L(Nq), \tag{2.17}$$

where $\tilde{I}^L$ and I^L represent Ω-to-Ω_L (continuum - to - finest grid) transfer operators, and N and q the continuous operator and solution, respectively. At convergence, the solution q_L of (2.16) coincides with $\tilde{I}^L q$. Of course, τ_L as defined by (2.17) cannot be evaluated because q is unknown. However, τ_L can be approximated by extrapolating the relative truncation error τ_L^{L-1} of the higher-order scheme:

$$\tau_L^{L-1} = N_{L-1}^+(\tilde{I}_L^{L-1} q_L^0) - I_L^{L-1} N_L^+(q_L^0), \tag{2.18}$$

which, as opposed to τ_L, can be evaluated. By assuming the validity of the truncation error relations

$$\tau_{L-1} = I_L^{L-1}\tau_L + \tau_L^{L-1}, \tag{2.19a}$$

$$\tau_{L-1} = 2^p I_L^{L-1}\tau_L, \tag{2.19b}$$

where p is the order of accuracy of the higher-order operators N_L^+ and N_{L-1}^+, we can approximate τ_L as

$$\tau_L = \frac{1}{2^p - 1} I_{L-1}^L \tau_L^{L-1}, \tag{2.20}$$

where I_{L-1}^L is a Ω_{L-1}-to-Ω_L-transfer operator for right-hand sides.

For the transfer operators we take

$$(q_{L-1})_{i,j} = (\tilde{I}_L^{L-1} q_L)_{i,j} \equiv \frac{1}{4}\Big[(q_L)_{2i,2j} + (q_L)_{2i-1,2j} + (q_L)_{2i,2j-1} + (q_L)_{2i-1,2j-1}\Big], \tag{2.21a}$$

$$(r_{L-1})_{i,j} = (I_L^{L-1} r_L)_{i,j} \equiv (r_L)_{2i,2j} + (r_L)_{2i-1,2j} + (r_L)_{2i,2j-1} + (r_L)_{2i-1,2j-1}, \tag{2.21b}$$

$$(I_{L-1}^L r_{L-1})_{2i,2j} = (I_{L-1}^L r_{L-1})_{2i-1,2j} = (I_{L-1}^L r_{L-1})_{2i,2j-1} = (I_{L-1}^L r_{L-1})_{2i-1,2j-1} \equiv \frac{1}{4}(r_{L-1})_{i,j}. \tag{2.21c}$$

So for the right-hand side prolongation operator I_{L-1}^L we take the adjoint of the right-hand side restriction operator I_L^{L-1}.

2.3.4. Results

Grids. For the mono-airfoils to be considered we apply O-type grids with the far-field boundary at an approximate distance from the airfoil of either ~ 25 or ~ 100 chord lengths. Compared to C-type grids, O-type grids have the advantage of smaller mesh sizes around the airfoil's tail. Further, in general, they have a more regular mesh size distribution along the far-field boundary. For moderate downwash (or upwash), C-type grids have of course the advantage of being better adapted to wake flows.

Far-field boundary conditions. For all airfoil flows to be considered here, we simply impose unperturbed far-field boundary conditions, although we do not over-impose. I.e. for a completely subsonic far-field boundary we impose three selected conditions at the inflow part of that boundary and one selected condition at the outflow part. A common practice with upwind discretizations is to simply over-impose along the complete far-field boundary, arguing that the upwind scheme imposes by itself the correct number of boundary conditions. However, though imposing by itself the correct *number*, in subsonic cases any existing upwind scheme cannot impose by itself the physically most correct *type* of conditions. It cannot make any selection for physical correctness among all conditions available. In case of e.g. uniformly constant over-specification across a subsonic wake leaving the domain, an upwind scheme imposes somehow that the velocity is constant across that wake, which is physically incorrect. Without introducing essential difficulties, it would be much better here to impose one physically correct condition only, e.g. a uniformly constant pressure. Concerning the choice to impose unperturbed far-field boundary conditions, by properly accounting for perturbations, of course, much can be gained in both accuracy and efficiency, the latter by reduction of the far-field distance. Though much work has been done on far-field perturbations (see e.g. [2]), properly introducing these perturbations in the algorithm without affecting its accuracy and efficiency may still be difficult. To avoid extra difficulties and to be on a par with standard reference work, here we impose free-stream conditions only.

In all cases we simply divide, a-priori, the far-field boundary into an inflow part and an outflow part. In all cases, at the inflow part we prescribe u,v and c to be uniformly constant, whereas at outflow we prescribe p to be uniformly constant. The combination u,v,c at inflow is convenient for airfoil cases with, standard, the far-field Mach number and angle of attack (M_∞ and α, respectively) specified. Imposing p at outflow is mathematically well-posed (section 2.2.3), and does not conflict, as just mentioned, with the commonly occurring situation of a subsonic wake flow leaving the domain.

Kutta condition. In all cases to be considered we assume that, without taking any precaution, no flow around trailing edges will occur, i.e. the Kutta condition is satisfied automatically. A support for this assumption is the fact that the different discretization methods to be employed, by being dissipative, all generate spurious increases of entropy and hence changes (decreases) in total pressure. As a consequence, flow around an airfoil's tail will in general result in a stagnation at two different pressures, which is an impossible situation. Hence in general, the Kutta condition will be satisfied automatically.

Multigrid schedule. For each test case we apply here - standard - a V-cycle with a single pre- and post-relaxation per level. For all mono-airfoils to be considered we use a coarsest grid with eight volumes tangentially to the airfoil and either four or two volumes radially. We notice that this is extremely coarse if seen in the light of doubts raised in [6] concerning the applicability of multigrid to airfoil flow problems with discontinuities.

NACA0012, $M_\infty = 0.8$, $\alpha = 1.25^0$. We first consider the case which, for some time, was most widely used for inviscid airfoil flow computations. The airfoil considered is the NACA0012-airfoil, and the far-field boundary conditions specified are $M_\infty = 0.8$, $\alpha = 1.25^0$. Leaving the stagnation region out of account, over the complete computational domain the flow speed is in the neighbourhood of the local speed of sound, making the flow of transonic type. The solution shows a rather pronounced lee-side shock, a very weak wind-side shock, and, consequently, a weak contact discontinuity shed from the trailing edge. The test case is generally assumed to be at the limit of what is possible with a potential flow model.

First we investigate the multigrid behaviour, applying as coarsest grid, Ω_1, an 8×4-grid, and as finest finest-grid, the 128×64-grid given in Fig. 2.10, $\Omega_L = \Omega_5$.

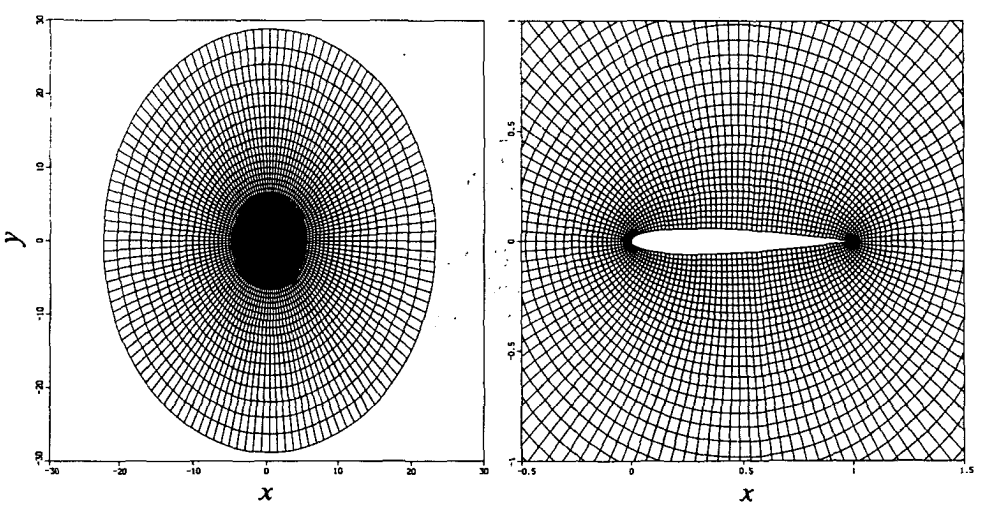

a. In full. b. In detail.

Fig. 2.10. 128×64-grid (Ω_5) NACA0012-airfoil.

In Fig. 2.11, the multigrid behaviour is presented by a graph of the residual ratios $\Sigma_{k=1}^{4}|(N_L(q_L^n))_k|/\Sigma_{k=1}^{4}|(N_L(q_L^0))_k|$, $L=3,4,5$ versus the number of cycles performed, one multigrid cycle being the V-cycle mentioned, and, for Ω_5 only, one single-grid cycle being the equivalent number of finest-grid relaxation sweeps. $|(N_L(q_L^n))_k|$ is defined in the same way as for the transonic wind tunnel flow (section 2.2.4). The convergence rates and the measure of grid independence are satisfactory. They are comparable with those obtained in [13] for the simply-connected, moderately perturbed channel flow. For Ω_5, we also add the multigrid convergence rate as obtained with Van Leer's scheme (instead of Osher's). Here (for the worse grid-aligned airfoil flow), though not significant, Osher's scheme appears to yield a better multigrid performance.

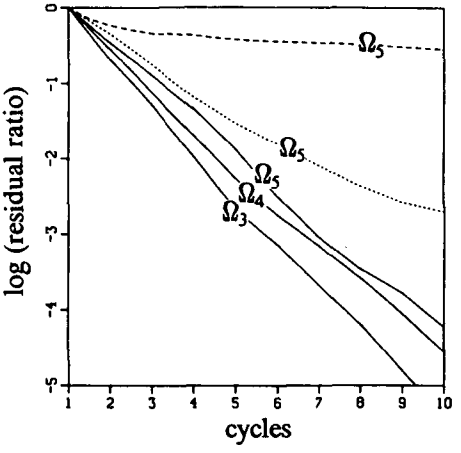

Fig. 2.11. Multigrid behaviour (NACA0012, $M_\infty=0.8$, $\alpha=1.25^0$), (------ : single-grid Osher, —— : multigrid Osher, ····· : multigrid Van Leer).

Next we investigate the convergence properties of iterative defect correction for the following five higher-order discretizations: (i) the centred scheme ($\kappa=1$), (ii) the one-sided scheme ($\kappa=-1$), (iii) the third-order scheme ($\kappa=\frac{1}{3}$), (iv) the superbox scheme, and (v) the Van Albada scheme. For this purpose, we perform for each scheme ten IDeC-cycles, with five FAS-cycles per IDeC-cycle. As finest grid, we apply the 32×16-grid given in Fig. 2.12, yielding a three-level multigrid schedule, $\Omega_L=\Omega_3$.

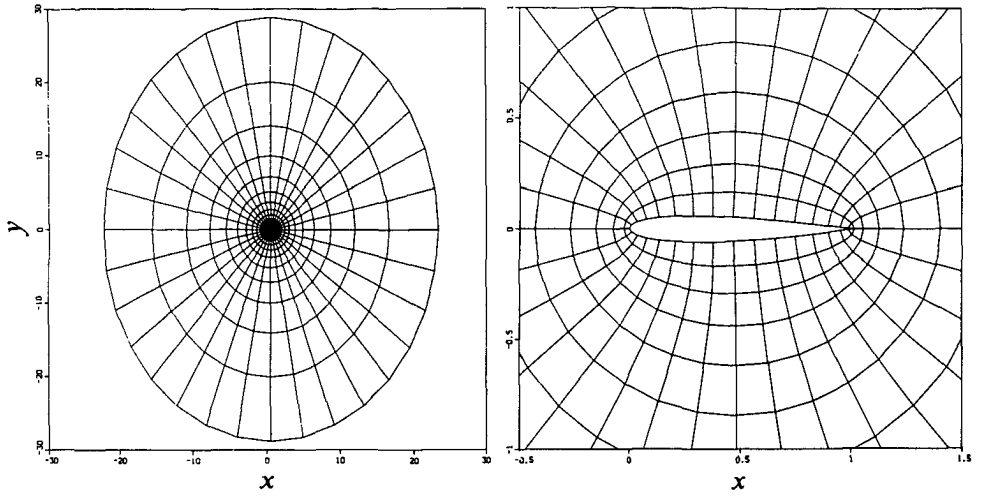

a. In full. b. In detail.

Fig. 2.12. 32×16-grid (Ω_3) NACA0012-airfoil.

In Fig. 2.13a, convergence histories are given by graphs of the residual ratio $\Sigma_{k=1}^{4}|(N_3^+(q_3^n))_k|/\Sigma_{k=1}^{4}|(N_3^+(q_3^0))_k|$, N_3^+ denoting the higher-order operator indicated near each graph, n the n-th FAS-cycle, and q_3^0 the first-order approximation as obtained at the end of the FAS-stage, the latter being, just as in Fig. 1.5, one FAS-cycle long only. The vertical lines in Fig. 2.13a mark the beginnings (and ends) of the IDeC-cycles. To avoid misunderstanding, we remark that each separate nonlinear multigrid iteration (i.e. each iteration corresponding with the history between two neighbouring vertical lines) does not converge to a solution of $N_3^+(q_3)=0$, because it solves $N_3(q_3)=N_3(q_3^n)-N_3^+(q_3^n)$. In Fig. 2.13b, graphs are given of the converged surface distribution of the entropy ratio s/s_∞, with $s\equiv p\rho^{-\gamma}$. For this, the curves with circular markers indicate the upper surface distributions, and those with triangular markers the lower surface distributions. Except for the superbox scheme, the markers correspond with the x-locations of the volume wall centres at the airfoil's surface. For the superbox scheme, due to the averaging mentioned (section 2.3.2), they correspond with the volume wall vertices at the airfoil's surface. It appears that both extreme schemes, the centred and one-sided scheme, lead to an early divergence of IDeC. For the centred scheme, the shock behaves as source of instability. For the one-sided scheme, the stagnation region behaves as such.

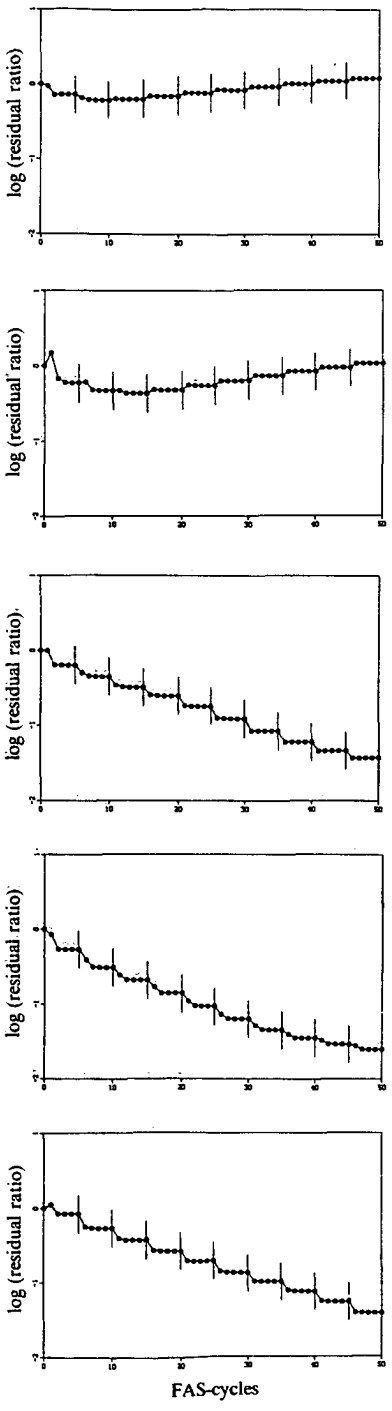

Centred

One-sided

Third-order

Superbox

Van Albada

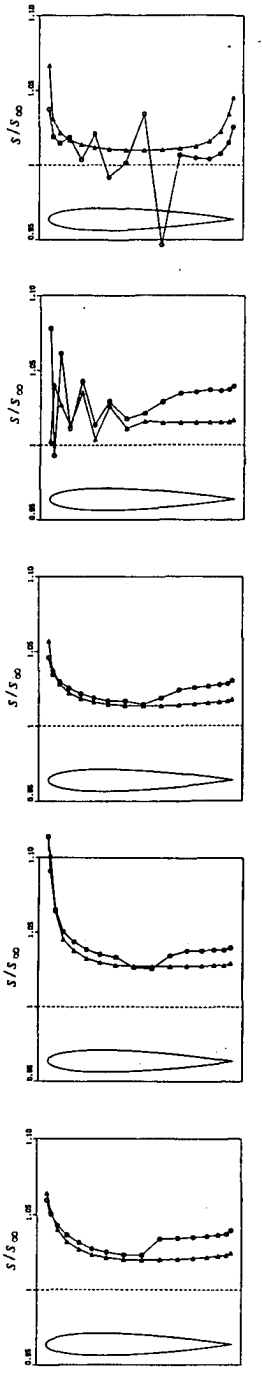

a. Convergence histories. b. Surface entropy distributions.

Fig. 2.13. Results higher-order schemes (NACA0012, $M_\infty = 0.8$, $\alpha = 1.25^0$).

From Fig. 2.13a it appears that the third-order scheme, the superbox scheme, and the Van Albada scheme all give convergence. Their convergence histories suggest that the use of one or two FAS-cycles per IDeC-cycle is sufficient. To investigate the optimal number of FAS-cycles per IDeC-cycle, we perform for these converging schemes successively: 20 IDeC-cycles with one FAS-cycle per IDeC-cycle, and 10 IDeC-cycles with two FAS-cycles per IDeC-cycle. As finest grid, we use again the 32×16-grid as shown in Fig. 2.12. The convergence histories obtained are given in Fig. 2.14. As starting point, we use the same first-order approximation q_3^0 as before. It clearly appears from Fig. 2.14 that the schedule with one FAS-cycle per IDeC-cycle is most efficient for each of the three schemes considered.

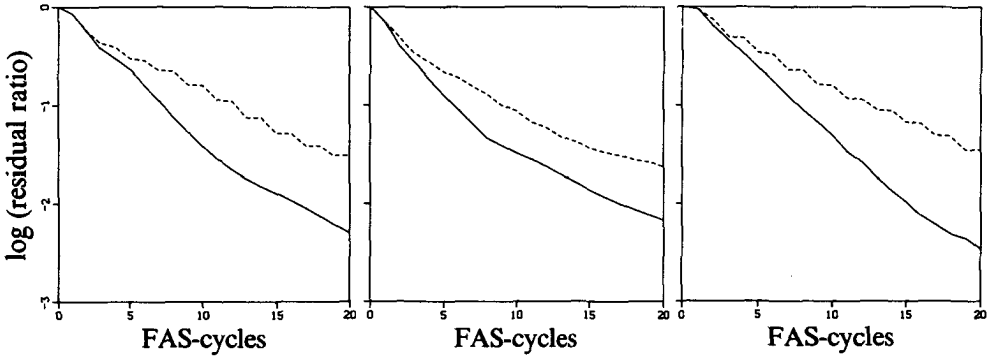

a. Third-order. b. Superbox. c. Van Albada.

Fig. 2.14. Convergence histories for one FAS-cycle (——) and two FAS-cycles (----) per IDeC-cycle (NACA0012, $M_\infty=0.8$, $\alpha=1.25^0$).

Next, we compare some qualitative properties of the fully converged first-order, third-order, superbox and Van Albada solution. As finest grid, we apply again the 32×16-grid. To be sure that the higher-order solutions are fully converged, we apply 50 IDeC-cycles (with one FAS-cycle per IDeC-cycle) for all three schemes. The pressure distributions obtained are given in Fig. 2.15. In each graph, the upper dashed line indicates the critical pressure, and the lower the stagnation pressure. The meaning of the markers is the same as in Fig. 2.13b. Clearly visible in Fig. 2.15 is the strong under- and overshoot at the shock wave, as obtained with the third-order and superbox scheme. The small wiggle upstream of the shock, as generated by the Van Albada scheme must be due to the centred and one-sided scheme that are used near boundaries. Compared with the first-order scheme, all three higher-order schemes give a significant improvement of the stagnation pressure.

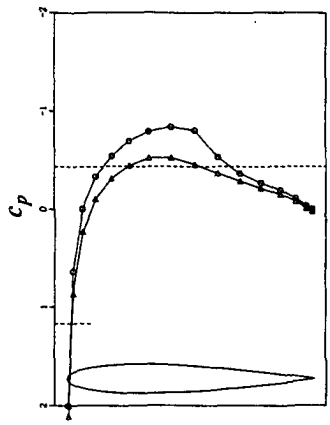

a. First-order.

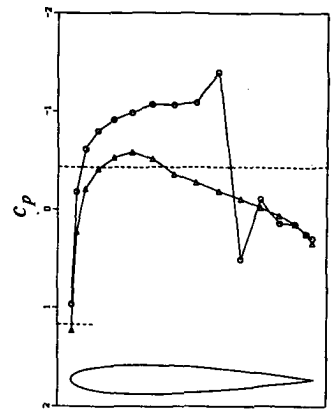

b. Third-order.

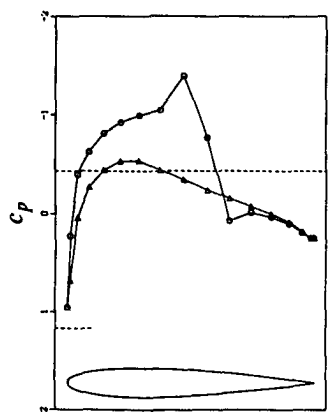

c. Superbox.

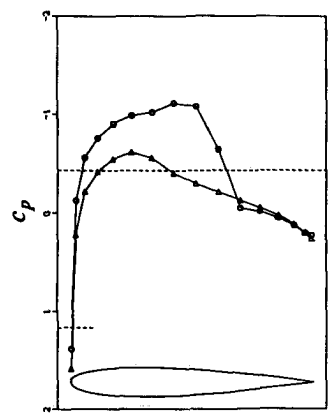

d. Van Albada.

Fig. 2.15. Converged surface pressure distributions (NACA0012, $M_\infty = 0.8$, $\alpha = 1.25^0$).

When we take monotonicity at full convergence as a requirement to be fulfilled, only the first-order scheme and Van Albada scheme can be used. However, since only a few IDeC-cycles might be necessary (and are desired of course), the question arises how spurious non-monotonicity at the shock develops in the first IDeC-cycles. To investigate this, we recompute the flow for both the first-order scheme and the three higher-order schemes. As finest grid we use now the corresponding, four times finer grid, the 128×64-grid already given in Fig. 2.10. As solution schedule, we apply ten IDeC-cycles with one FAS-cycle per IDeC-cycle. The results obtained are given in Fig. 2.16 and 2.17. Fig 2.16a and 2.16b show the first-order pressure distribution as obtained after one and ten FAS-cycles, respectively. The meaning of the markers and dashed lines in the graphs is the same as before. The pressure distribution in Fig. 2.16a shows in fact the first-order solution which is used as initial estimate for (1.20). The distribution in Fig. 2.16b is that of the fully converged first-order solution. (We notice that the solution as obtained after one FAS-cycle is already converged to truncation error accuracy.) Fig. 2.17 shows for the three higher-order schemes the pressure distribution, as obtained after successively one, two, three and ten IDeC-cycles. From Fig. 2.17 an opposite behaviour after the first IDeC-cycle becomes clear. The small wiggles, as obtained with all three schemes after the first IDeC-cycle, grow in the following IDeC-cycles for the third-order and superbox scheme, but shrink for the Van Albada scheme. The Van Albada scheme yields a nearly wiggle-free solution after the third IDeC-cycle already. Remarkable for all three schemes is the excellent improvement of the stagnation pressure which is obtained in the first IDeC-cycle.

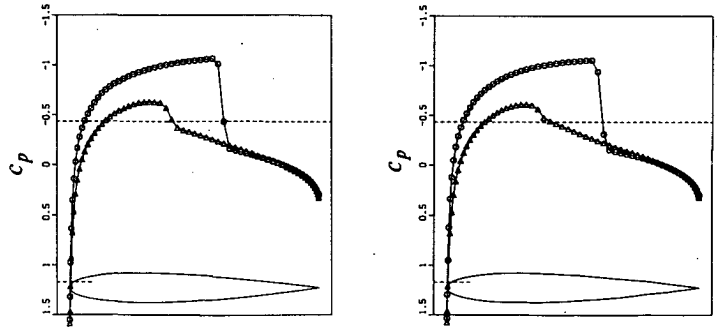

a. After one FAS-cycle. b. After ten FAS-cycles.

Fig. 2.16. First-order surface pressure distributions (NACA0012, $M_\infty = 0.8$, $\alpha = 1.25^0$).

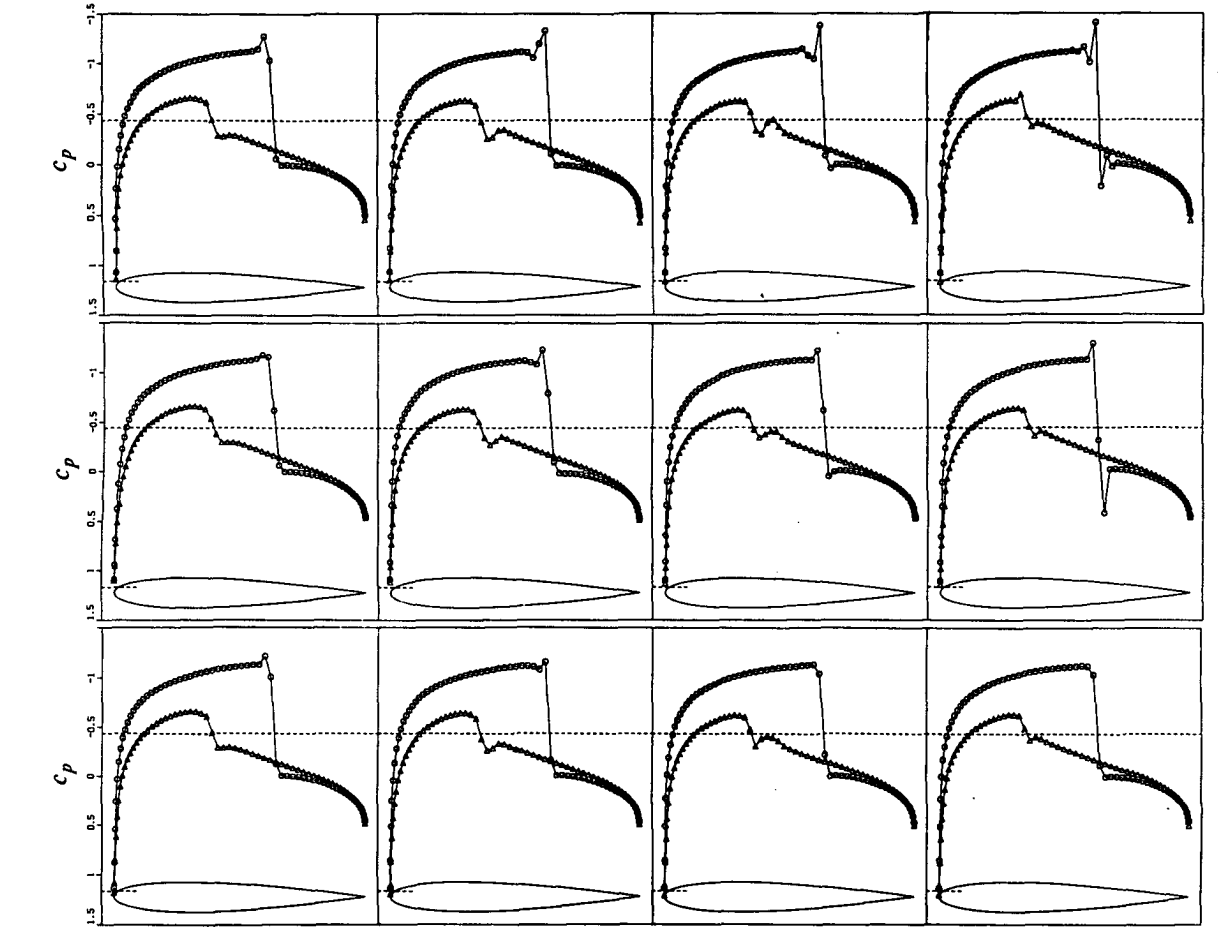

Fig. 2.17. Higher-order surface pressure distributions (NACA0012, $M_\infty = 0.8$, $\alpha = 1.25^0$).

In Fig. 2.18 we give the converged, higher-order surface entropy distributions. All three higher-order schemes lead to an excellent improvement of the entropy distribution, the third-order, as expected, to the best.

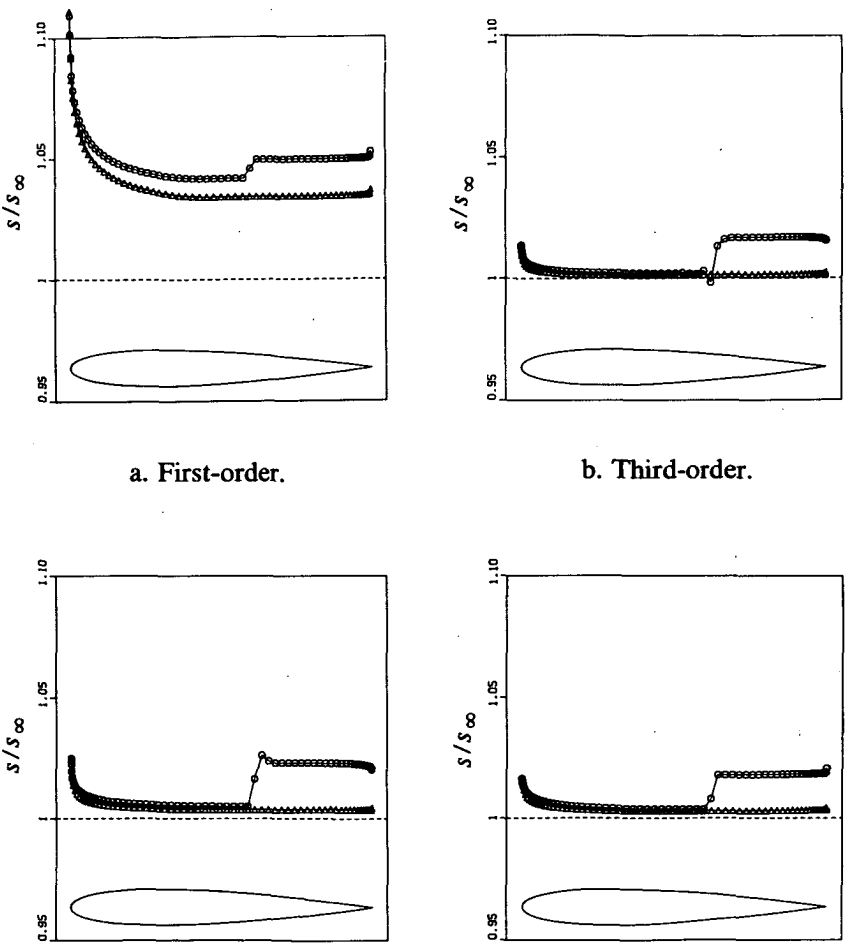

a. First-order.

b. Third-order.

c. Superbox.

d. Van Albada.

Fig. 2.18. Surface entropy distributions after tenth FAS-cycle (first-order scheme) and tenth IDeC-cycle (higher-order schemes), (NACA0012, $M_\infty = 0.8$, $\alpha = 1.25^0$).

In Fig. 2.19 we make a comparison with reference results. In Fig. 2.19a, the left graph shows the pressure distributions that we obtained after ten IDeC-cycles, whereas the right graph shows all Euler flow results stemming from [32]. In Fig. 2.19b we do the same, using here only the best Euler flow results from [36]. In Fig. 2.19a, the agreement between the various reference results is poor. This is partly caused by wiggles, but mostly by a large scattering in shock position. A smaller scattering is found in the more recent reference results given in Fig. 2.19b. The agreement between our results and these very fine grid results is good, with the exception of the under- and overshoots, as generated by the third-order and superbox scheme. In Fig. 2.19c, we present for the Van Albada scheme the convergence history of the lift and drag coefficient and make a comparison with (converged) reference results, which are spread over the shaded areas. One shading represents all five Euler results from [32], the other shading all seven Euler results from [36]. Clearly visible in Fig. 2.19c, is the excellent improvement of the drag, which is obtained in the first IDeC-cycle. (The main cause of this is of course the strong improvement of the stagnation pressure in the first IDeC-cycle, Fig. 2.16 and 2.17.) When we take the results from [32] as a standard, we see that we only need one IDeC-cycle to reach the standard. With the results from [36] as a standard, we end up with a lift which is slightly too low. The cause of this discrepancy is thought to be the fact that the outer boundary is not far enough ($\sim$25 chord lengths) from the airfoil. Applying a finest grid with an outer boundary at $\sim$100 chord lengths, but yet with a twice smaller number of volumes in the radial direction (32 instead of 64) and a twice smaller volume height at the airfoil (Fig. 2.20), we obtain the results given in Fig. 2.21 and 2.22. The solution improvements are evident (Fig. 2.22). Though slightly less grid-independent than that in Fig. 2.11, the corresponding multigrid behaviour is still very satisfactory (Fig. 2.21). (Remarkable, but fortunately not important, is the worse single-grid history in comparison with that in Fig. 2.11.)

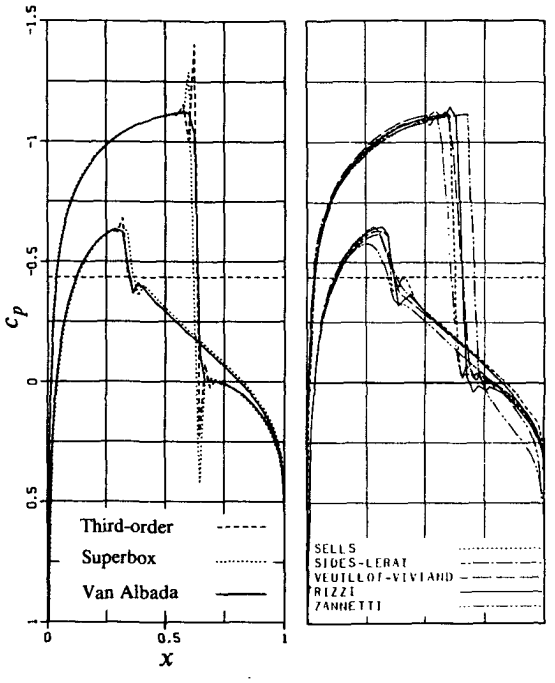

a. Surface pressure distributions, present results (left) and reference results from [32] (right).

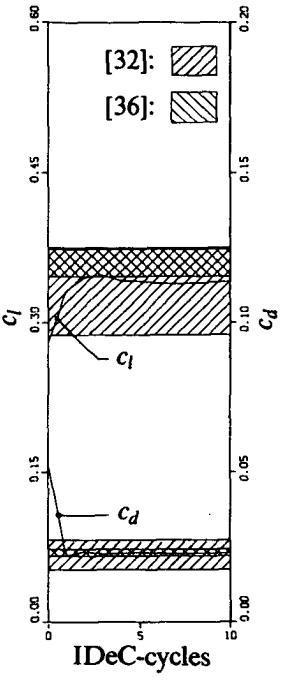

c. Convergence history lift and drag coefficient (Van Albada scheme).

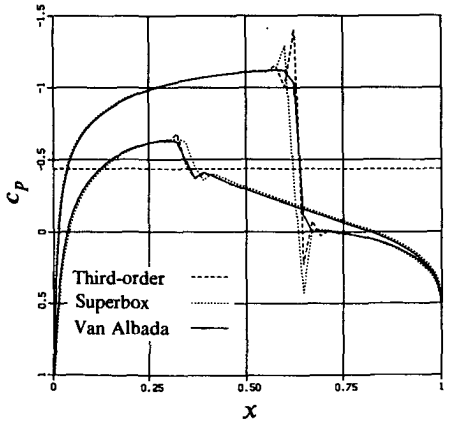

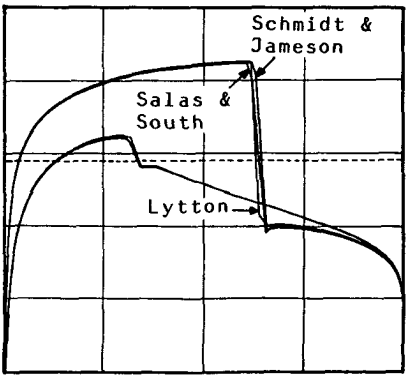

b. Surface pressure distributions, present results (left) and reference results from [36] (right).

Fig. 2.19. Results NACA0012-airfoil at $M_\infty = 0.8$, $\alpha = 1.25^0$.

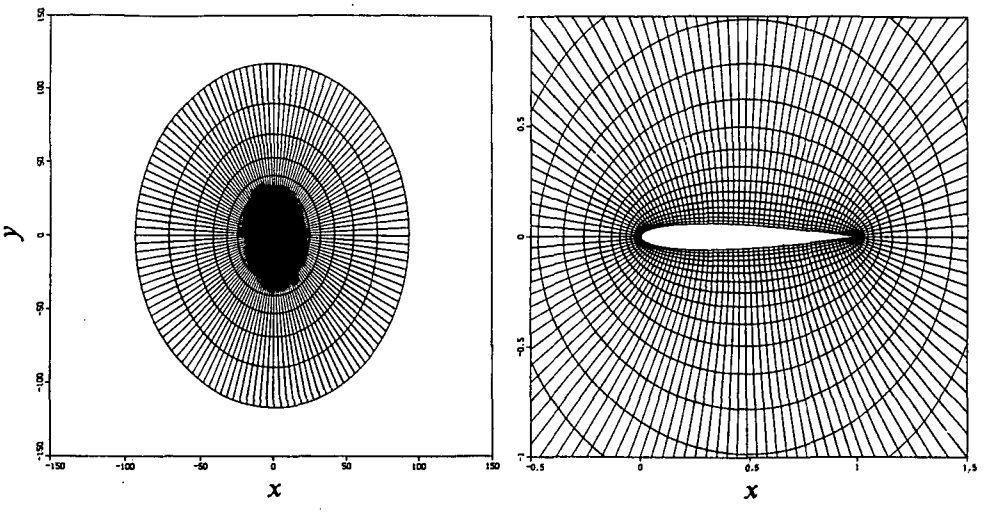

a. In full. b. In detail.

Fig. 2.20. 128×32-grid (Ω_5) NACA0012-airfoil.

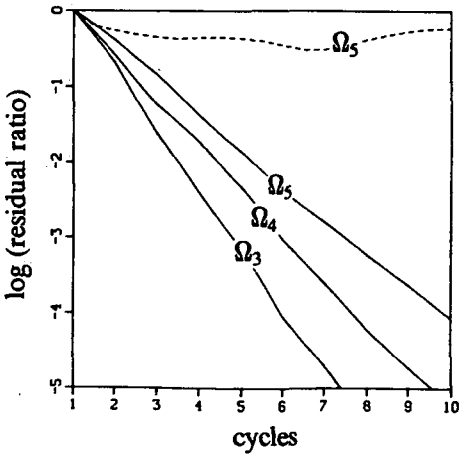

Fig. 2.21. Multigrid behaviour NACA0012-airfoil at $M_\infty = 0.8$, $\alpha = 1.25^0$ for new grid (------ : single-grid, —— : multigrid).

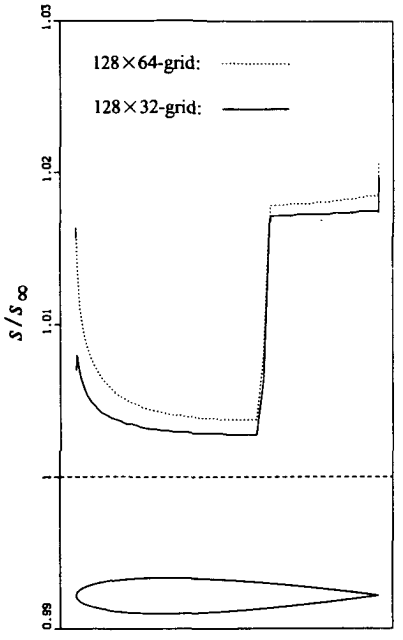

a. Upper surface entropy distributions.

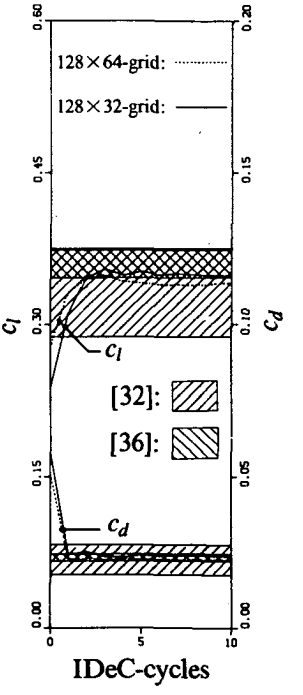

b. Convergence histories lift and drag coefficient.

Fig. 2.22. Results 128×64- and 128×32-grid, NACA0012-airfoil at $M_\infty = 0.8$, $\alpha = 1.25^0$ (Van Albada scheme).

NACA0012, $M_\infty = 0.63$, $\alpha = 2^0$. Before considering typical Euler test cases for the NACA0012-airfoil, we first consider the standard subsonic potential flow case with $M_\infty = 0.63$, $\alpha = 2^0$. This case is considered mainly for verifying how close we can approximate d'Alembert's exact zero-drag for a given grid, the 128×32-grid just considered (Fig. 2.20). Given the relative smoothness of the flow, for this purpose, we will also investigate the possibilities of τ-extrapolation.

First, in Fig. 2.23 we show the multigrid behaviour with the 128×32-grid as finest finest-grid and the corresponding 8×2-grid as coarsest grid. Multigrid performs well. Despite the rather large physical differences, the multigrid behaviour for this subsonic test case shows a very good resemblance with that of the transonic one in Fig. 2.21.

In Fig. 2.24, for a schedule without τ-extrapolation, we make a comparison with reference results, among the reference surface pressure distributions (Fig. 2.24a) also potential flow results, the reference results for lift and drag (Fig. 2.24b) being Euler flow results only. Remarkable is the excellent agreement between the surface pressure distributions of the three higher-order schemes. Further, very good (already) is the drag yielded by the third-order and super-box scheme. For the rather coarse finest-grid applied, both approach the zero-drag significantly better than any of the Euler results from [32], the super-box scheme even slightly better than the third-order scheme. Moreover, for all three higher-order schemes, the convergence of IDeC is fast. Within a few IDeC-cycles their corresponding lift and drag values seem to be converged for practical purposes.

In Tab. 2.1 we present the c_d-history for the converged $\kappa = \frac{1}{3}$-solution (Fig. 2.24a) and τ-extrapolation. Four different combinations of I_{L-1}^L and p are investigated. (The restriction operators $\tilde{I}_L^{L-1}$ and I_L^{L-1} are not varied but taken the same as in (2.21).) It clearly appears that the approach with I_{L-1}^L according to (2.21c) ($I_{L-1}^L = O(h)$) and with $p = 3$, is the best. With this approach, only three additional IDeC-cycles are sufficient to reduce the converged $\kappa = \frac{1}{3}$-c_d from four counts to one count only. A comparison of the corresponding surface pressure distribution with the $\kappa = \frac{1}{3}$-distribution does not show any qualitative difference. (Only very slight quantitative differences can be observed such as a slightly higher suction peak in the τ-extrapolation case.)

n	I_{L-1}^L	$O(h)$	$O(h)$	$O(h^2)$	$O(h^2)$
	p	2	3	2	3
0		4	4	4	4
1		−7	−1	−44	−16
2		−5	0	−29	−10
3		−3	1	−24	−8
4		−3	1	−22	−7
5		−3	1	−22	−7

Tab. 2.1. Convergence history drag coefficient ($\times 10^{-4}$) NACA0012-airfoil at $M_\infty = 0.63$, $\alpha = 2^0$, for different τ-extrapolation techniques.

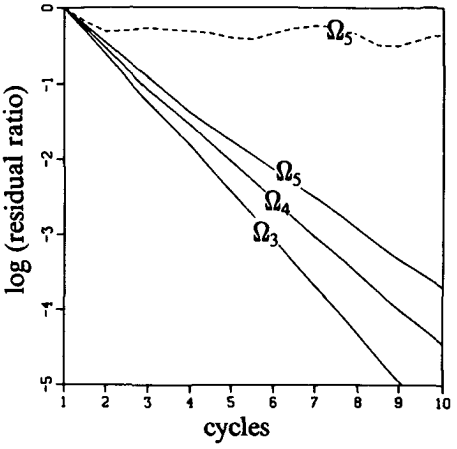

Fig. 2.23. Multigrid behaviour NACA0012-airfoil at $M_\infty = 0.63$, $\alpha = 2^0$ (------ : single-grid, —— : multigrid).

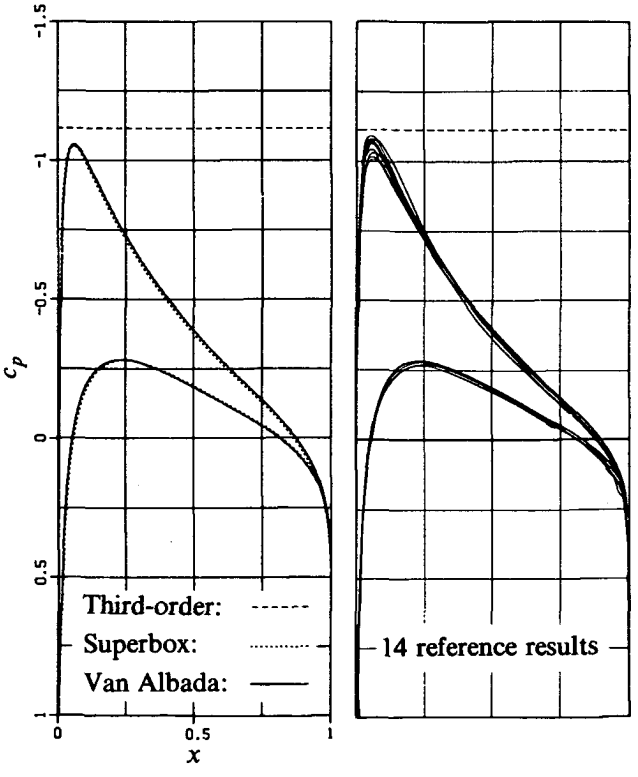

a. Surface pressure distributions, present results (left) and reference results from [32] (right).

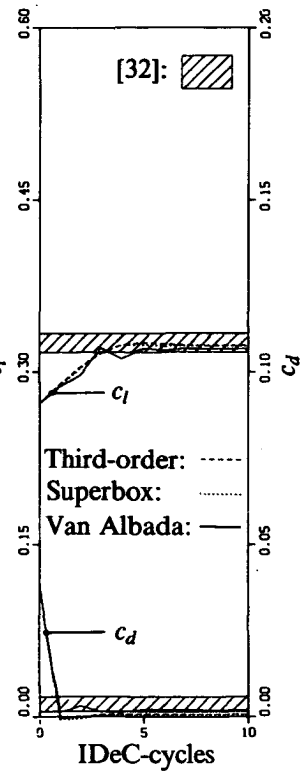

b. Convergence histories lift and drag coefficient.

Fig. 2.24. Results NACA0012-airfoil at $M_\infty = 0.63$, $\alpha = 2^0$ (without τ-extrapolation).

NACA0012, $M_\infty = 0.85$, $\alpha = 1^0$. At present, this seems to be the most popular airfoil test case for Euler flow methods. Its flow is probably at the limit of what may still be called transonic. It has a rather strong lee-side shock and a significantly less strong wind-side shock, resulting in a strong contact discontinuity. Potential flow methods are definitely not suited for this test case.

For the same family of grids as with the previous test case, the multigrid behaviour is given in Fig. 2.25. Despite the rather strong discontinuities, no significant deterioration is observed in comparison with the two milder previous cases.

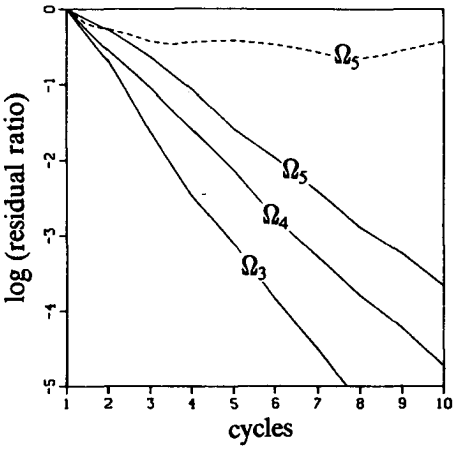

Fig. 2.25. Multigrid behaviour NACA0012-airfoil at $M_\infty = 0.85$, $\alpha = 1^0$ (------ : single-grid, —— : multigrid).

We compare our solution with those of Salas and South [36], and Schmidt and Jameson [36]. They use an O-type grid of 192×39 points and 320×64 cells, respectively. Although no evidence can be given that they both really needed such a fine grid, it can be seen that we can use a significantly coarser grid (128×32 O-type, Fig. 2.20). Our lift and drag agree well with theirs. Salas and South find $c_l = 0.3472$, $c_d = 0.0557$, and Schmidt and Jameson find $c_l = 0.3584$, $c_d = 0.0580$, whereas we find $c_l = 0.3565$, $c_d = 0.0582$. All three discontinuities occurring in the flow are captured about equally well in our results and the reference results (Fig. 2.26a and 2.26c). Our entropy distribution (Fig. 2.26d, no comparable results available) shows furthermore a very modest entropy error (0.002) just upstream of the foot of both shock waves. (The smearing of the entropy layer in radial direction is only due to the grid enlargement in this direction.) The lift and drag seem to be converged for practical purposes within (again) only a few IDeC-cycles (Fig. 2.26b).

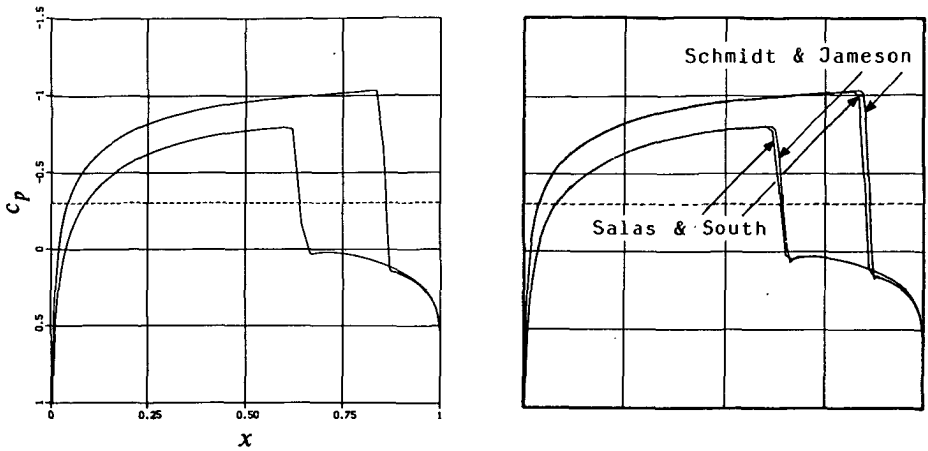

a. Surface pressure distributions, present result (left) and reference results from [36] (right).

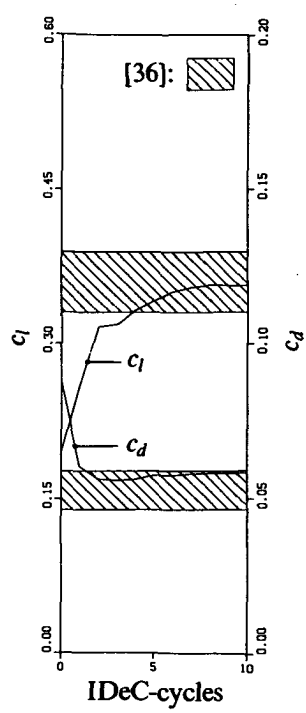

b. Convergence history lift and drag coefficient.

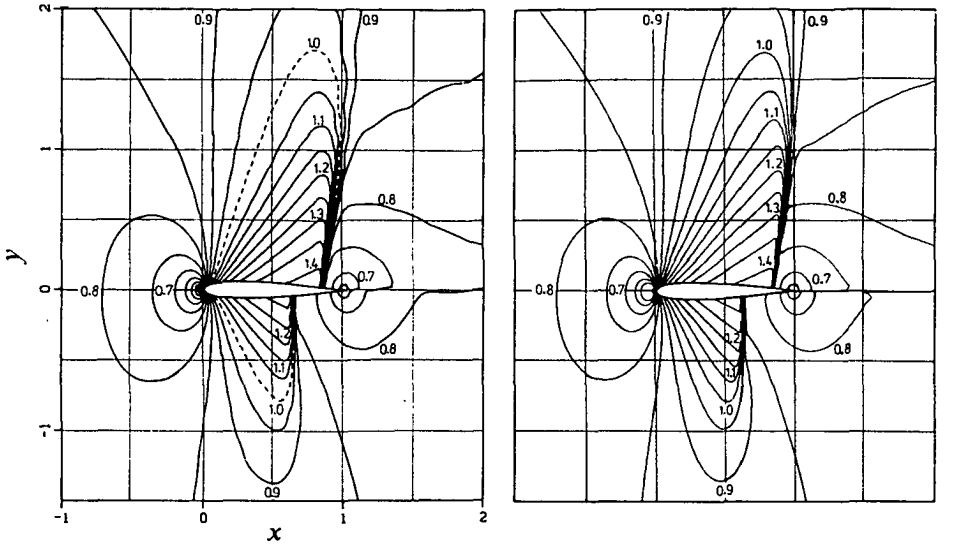

c. Mach number distributions,
present result (left) and
result Schmidt and Jameson [36] (right).

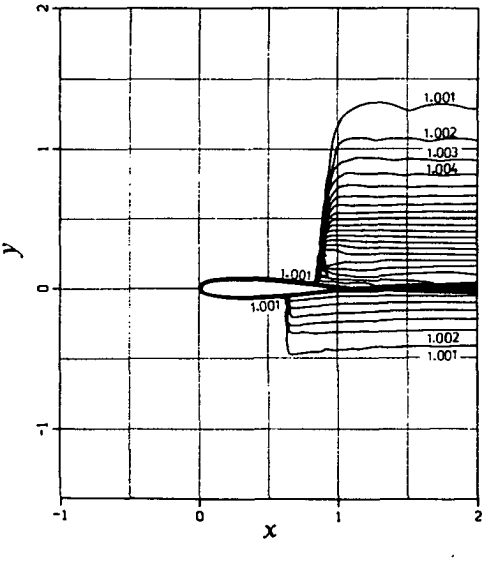

d. Present entropy distribution (s/s_∞).

Fig. 2.26. Results NACA0012-airfoil at $M_\infty = 0.85$, $\alpha = 1^0$
(Van Albada scheme).

NACA0012, $M_\infty = 1.2$, $\alpha = 7^0$. This standard test case is definitely no longer transonic, and, given the presence of a curved detached bow shock, the flow is completely rotational along the airfoil. (For this case, estimates of surface distributions assuming any irrotationality are absolutely unreliable.)

For an unaltered family of grids, the multigrid method behaves as shown in Fig. 2.27. The better convergence rates than those obtained for the previous cases are due to the fact that the relaxation method is a perfect smoother whenever sweeping in a supersonic flow direction.

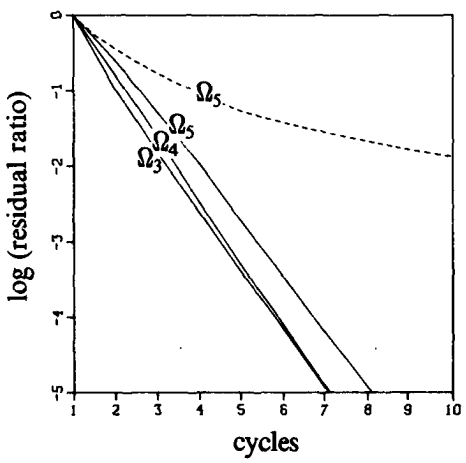

Fig. 2.27. Multigrid behaviour NACA0012-airfoil at $M_\infty = 1.2$, $\alpha = 7^0$ (------ : single-grid, —— : multigrid).

Our solution is compared with those of Schmidt and Jameson [36], and Veuillot and Vuillot [36]. They use a 320×64-cells O-type grid and a 201×55-points C-type grid, respectively. They find $c_l = 0.5138$, $c_d = 0.1538$ and $c_l = 0.5280$, $c_d = 0.1536$, respectively, whereas we find $c_l = 0.5237$, $c_d = 0.1551$. Except for a slight difference in drag and upstream location of the bow shock (Fig. 2.28c), the agreement between our results and the reference results is good. With our worse adapted and coarser 128×32-grid, we obtain a solution of the same quality. Our entropy distribution finally (Fig. 2.28d, no comparable results available) shows again a very modest entropy error; it is again 0.002 just upstream of the airfoil's tail.

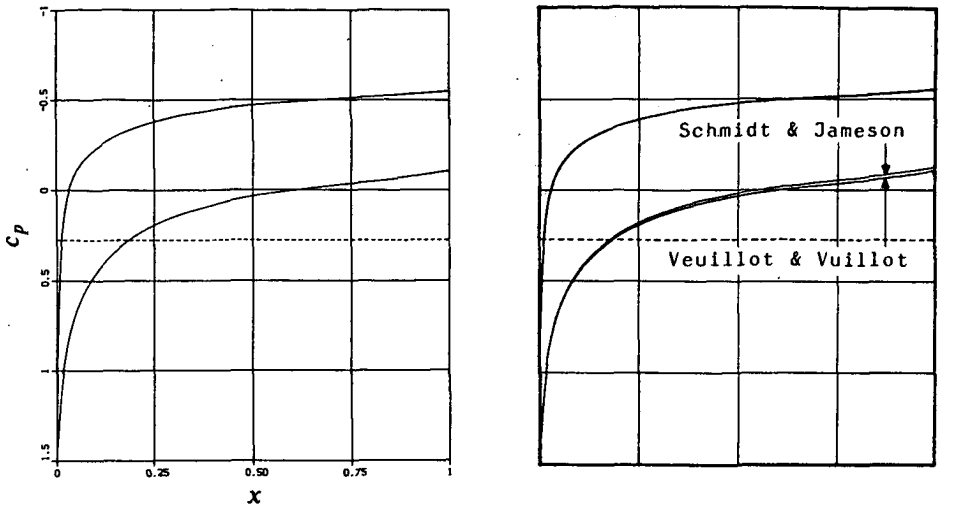

a. Surface pressure distributions, present result (left) and reference results from [36] (right).

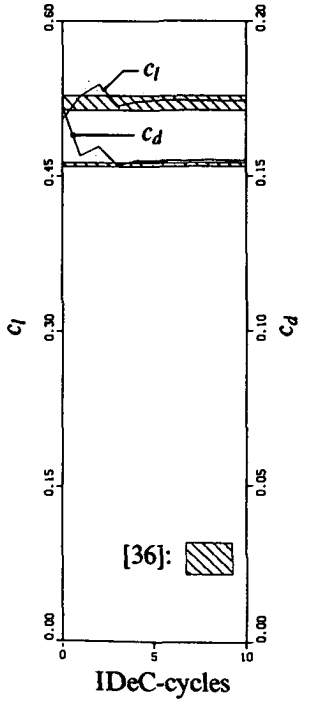

b. Convergence history lift and drag coefficient.

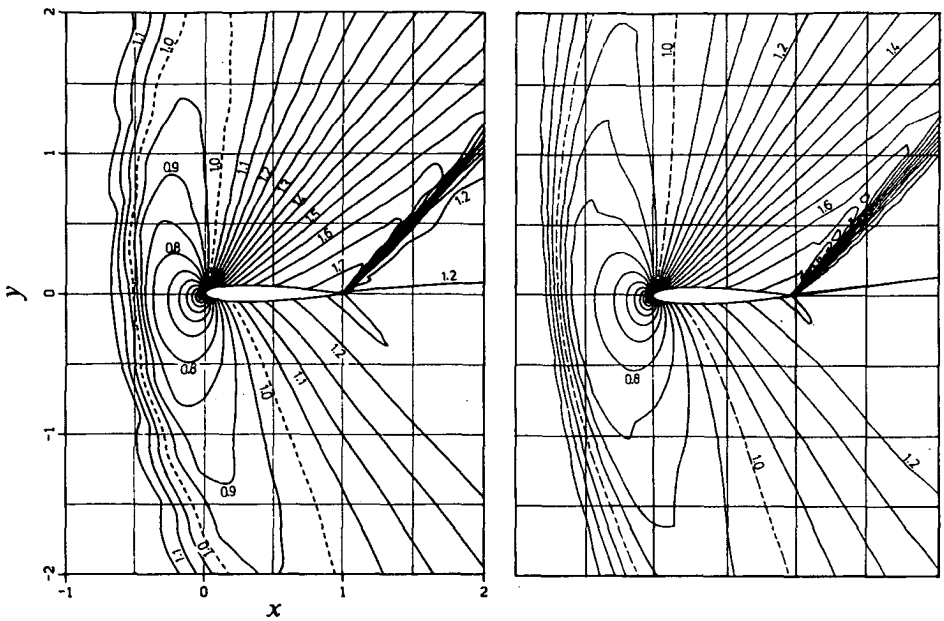

c. Mach number distributions,
present result (left) and
result Veuillot and Vuillot [36] (right).

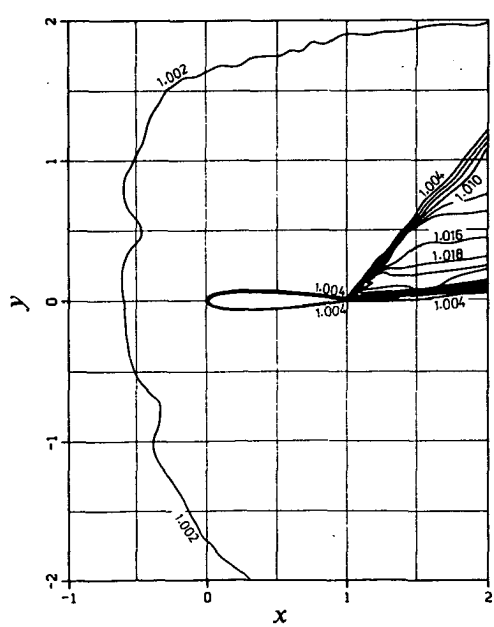

d. Present entropy distribution (s/s_∞).

Fig. 2.28. Results NACA0012-airfoil at $M_\infty = 1.2$, $\alpha = 7^0$
(Van Albada scheme).

NLR7301, $M_\infty = 0.721$, $\alpha = -0.194^0$. Though supercritical flows with shock waves and contact discontinuities are very relevant for developing accurate and efficient Euler flow methods, although rare, supercritical shock-free flows are not less relevant. The absence of exact reference solutions for the first flows but the availability of such results for supercritical shock-free flows makes the latter more rigorous test cases. A major difficulty in the numerical computation of transonic shock-free airfoil flows is to avoid shock wave formation in the isentropic compression flow along the airfoil's lee side. This holds in particular when applying an upwind shock capturing scheme, because of the tendency of such schemes to create shock waves in regions of converging characteristics.

A standard and well-documented supercritical, shock-free airfoil flow is the NLR7301-airfoil at the design conditions $M_\infty = 0.721$, $\alpha = -0.194^0$ [3]. In the first instance we investigate how close we can approximate its hodograph solution with the same numerical schedule as applied for the previous two NACA0012-cases; 128×32 O-type finest-grid (Fig. 2.29) with the far-field boundary again at ~100 chord lengths, 8×2 coarsest grid, unperturbed far-field boundary conditions, ten IDeC-cycles with one FAS-cycle per IDeC-cycle, and so on. As higher-order scheme we apply the superbox scheme, the motivation being its most close approximation of zero-drag for the subcritical airfoil flow considered before.

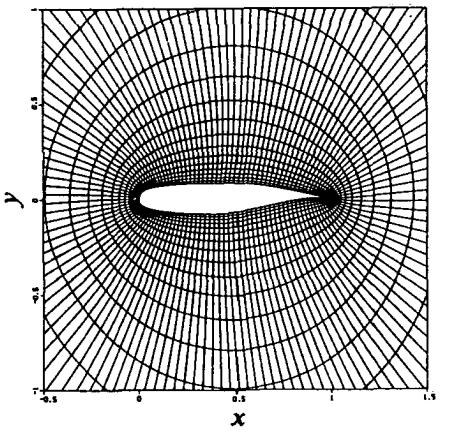

Fig. 2.29. 128×32-grid NLR7301-airfoil, in detail.

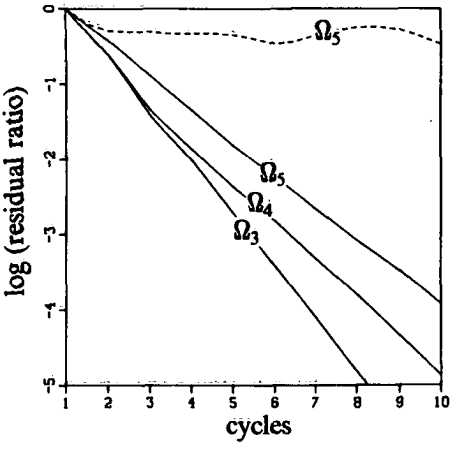

Fig. 2.30. Multigrid behaviour NLR7301-airfoil at $M_\infty = 0.721$, $\alpha = -0.194^0$ (----- : single-grid, —— : multigrid).

The multigrid behaviour, given in Fig. 2.30, is satisfactory. Though the higher-order lift and drag history (Fig. 2.31b) are satisfactory as well (both in regard to convergence rate and accuracy of converged values), the corresponding surface presure distribution (Fig. 2.31a) is not. It clearly shows a potential flow break-down. Continuing with τ-extrapolation and this imperfect solution does not help; the initial solution (Fig. 2.31a) is not sufficiently smooth. The $\kappa = \frac{1}{3}$-solution obtainable on the underlying 64×16-grid is, but unfortunately it is not accurate enough to obtain a satisfactory solution by means of τ-extrapolation.

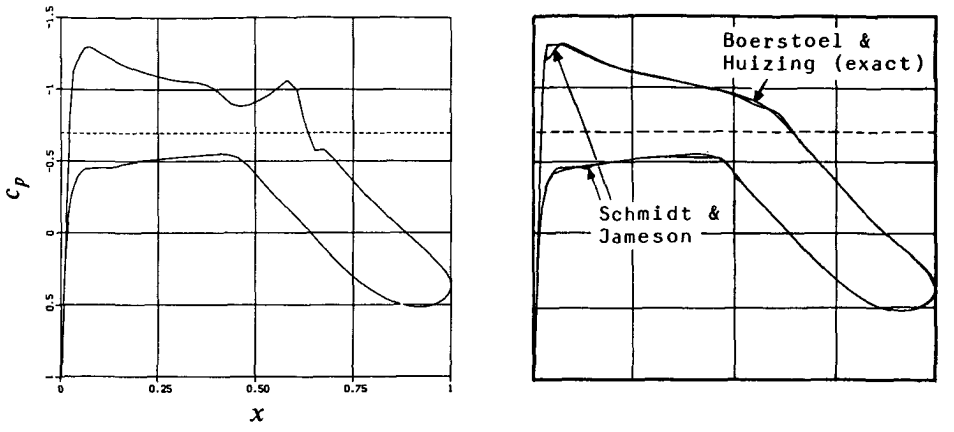

a. Surface pressure distributions,
present result (left) and
reference results from [36] (right).

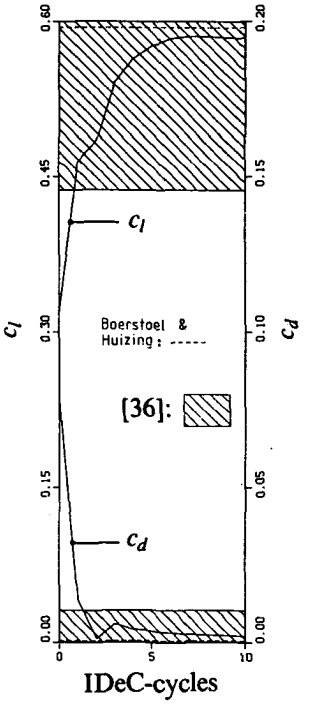

b. Convergence history
lift and drag coefficient.

Fig. 2.31. Results NLR7301-airfoil at $M_\infty = 0.721$, $\alpha = -0.194^0$
(superbox scheme, without τ-extrapolation).

First we assumed the cause of the break-down to be an accumulation of discretization errors in the most downstream part of the supersonic zone. This accumulation might be explained with the mechanism of Mach lines emanating from the airfoil along the entire supersonic zone, reflecting at the sonic line, and finally focusing in the most downstream part of the supersonic zone. Yet, with an adapted grid as shown in Fig. 2.32, we did not obtain any significant improvement.

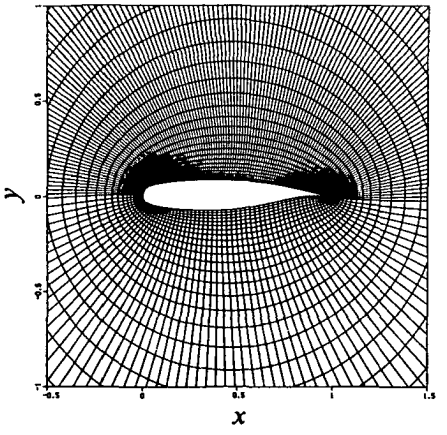

Fig. 2.32. 192×48-grid NLR7301-airfoil, in detail.

Besides τ-extrapolation and grid adaptation, some other possible remedies have been investigated. We applied other higher-order schemes, a rotated version of Osher's scheme [11], a device against sonic glitches [5], and solid wall boundary condition treatments taking into account surface curvature [18,34]. None of these remedies worked, neither alone nor in combination with others. Concerning the reference results [36], it was noticed that most of them show some sort of break-down. Further, it was remarkable to see that Schmidt and Jameson [36], who most closely approach the exact solution (Fig. 2.31a), also used the finest grid (322×66-cells O-type). It finally seemed that if no elegant means of improvement could be found, just like Schmidt and Jameson, strong overall grid refinement needed to be applied. So it seemed, until at NLR, with the present numerical method though with perturbed far-field boundary conditions, a very satisfactory solution was obtained on a 128×32-grid only [27]. Our confidence in the numerical method was restored. Unfortunately, for the corresponding twice as fine grid, though for the rest exactly identical numerical schedule, the potential flow broke down again [27], this time not eroding our confidence in the method, but that in the mathematical posedness of the corresponding continuous problem. Our present opinion is that an existency analysis, analogous to that performed by Morawetz [22,23,24,25] but now for the Euler equations, might well yield that steady, transonic shock-free solutions for the Euler - continuum - boundary value problem are isolated points as well. (If so, because of Pearcey's experimental work [31], no transonic controversy can re-arise of course.)

bi-NACA0012, $M_\infty = 0.5$, $\alpha = 2^0$. To finish, we show the method's feasibility for computing flows with sources of any of the conserved quantities. Here we will consider momentum and energy sources which model a propulsion system. The configuration considered is composed of two NACA0012-airfoils and a propeller disk. The NACA0012-airfoils are placed in parallel formation, and the propeller disk is placed between the airfoil noses (Fig. 2.33). The configuration may be interpreted as a model for a bi-plane with airscrew(s) between its leading edges. The propeller is modelled as a line distribution of x-momentum and energy sources. The configuration has not been considered elsewhere.

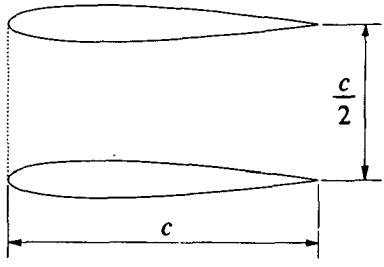

Fig. 2.33. bi-NACA0012-airfoil with propeller disk.

As finest grid we apply the 128×48-grid as shown in Fig. 2.34. The non-smooth grid at the airfoil noses will lead to a solution of worse quality than in the case of a body-fitted grid. Yet, to avoid extensive grid generation efforts we prefer the present grid to the alternative of a smooth, body-fitted grid in a multi-domain approach. The outer boundary of the grid is taken at an approximate distance from the configuration of ten chord lengths. For the solution schedule, five IDeC-iterations and four coarser grids are taken.

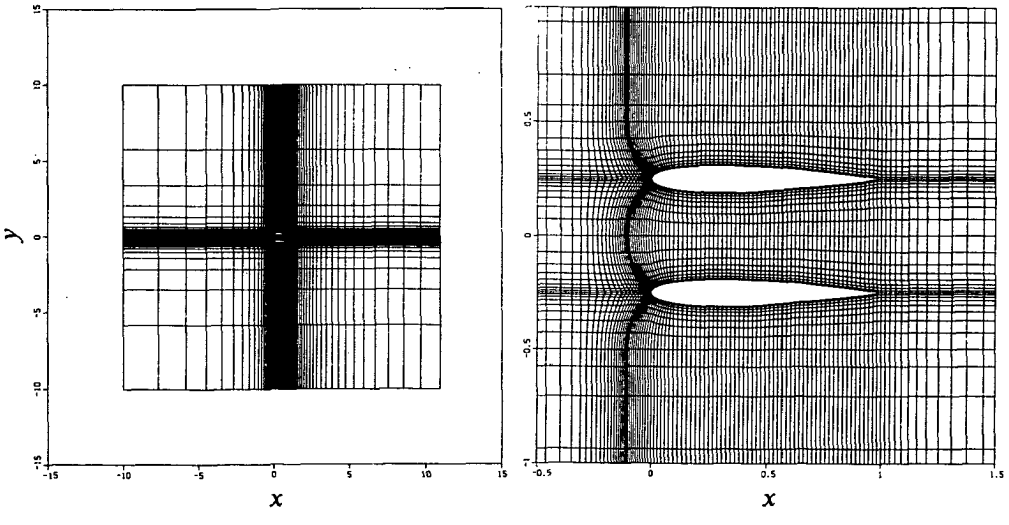

a. In full. b. In detail.

Fig. 2.34. 128×48-grid bi-NACA0012-airfoil.

The configuration is considered twice at $M_\infty = 0.5$, $\alpha = 2^0$; namely with the propeller disk switched off and with the propeller disk switched on. In both cases we impose unperturbed conditions at the outer boundary: u, v, c constant at inflow and p constant at outflow. (Notice that p = constant across a jet leaving the computational domain is physically correct.) We assume the propeller disk to be located inside the finite volumes, i.e. it does not coincide with any cell face. In each volume $\Omega_{i,j}$ which is intersected by the propeller disk, a local line source of x-momentum and energy per unit of length and time, $(s_2)_{i,j}$ and $(s_4)_{i,j}$, respectively, are computed in the following way. Introducing in each such $\Omega_{i,j}$ the hypothetical states $q^u_{i,j}$ and $q^d_{i,j}$ up- and downstream of the propeller, respectively, we prescribe an isentropic pressure jump:

$$p^d_{i,j} = (1+\delta)p^u_{i,j}, \quad \delta > 0, \tag{2.22a}$$

$$(p\rho^{-\gamma})^d_{i,j} = (p\rho^{-\gamma})^u_{i,j}, \tag{2.22b}$$

with δ constant. Besides these two propeller relations we have the steady jump relations

$$\begin{bmatrix} \rho u \\ \rho u^2 + p \\ \rho uv \\ \rho u(e + \frac{p}{\rho}) \end{bmatrix}^d_{i,j} - \begin{bmatrix} \rho u \\ \rho u^2 + p \\ \rho uv \\ \rho u(e + \frac{p}{\rho}) \end{bmatrix}^u_{i,j} = \begin{bmatrix} 0 \\ s_2 \\ 0 \\ s_4 \end{bmatrix}_{i,j}, \tag{2.23}$$

Taking $q^u_{i,j} = q_{i,j}$, we have obtained a system of six equations with six unknowns: $\rho^d_{i,j}, u^d_{i,j}, v^d_{i,j}, p^d_{i,j}$, $(s_2)_{i,j}$ and $(s_4)_{i,j}$, from which $(s_2)_{i,j}$ and $(s_4)_{i,j}$ can be computed. (So in each finite volume which is intersected by the propeller disk, the x-momentum and energy source are functions of δ and $q_{i,j}$ only.) To solve the system of discretized equations with source terms, we simply apply the defect correction iteration

$$N_L(q_L^{n+1}) = N_L(q_L^n) - (N_L^+(q_L^n) - r_L(q_L^n)), \quad n = 0,1,...,N, \tag{2.24}$$

with

$$(r_L(q_L))_{i,j} = (0, s_2, 0, s_4)^T_{i,j} l_{i,j}, \tag{2.25}$$

where $l_{i,j}$ is the length of the propeller part inside $\Omega_{i,j}$. (Difficult source terms depending on the solution fit perfectly well in an IDeC-process.)

For the case with working propeller we arbitrarily take $\delta = 0.1$. For both cases (propeller on and off) convergence to the solution of $N_L^+(q_L) = r_L(q_L)$ is obtained. The converged values of lift and drag of the upper and lower airfoil (yielded by the fifth IDeC-cycle) are given in Tab. 2.2.

	propeller disk off ($\delta=0$)	propeller disk on ($\delta=0.1$)
$c_{l_{upper}}$	−0.24	−0.89
$c_{l_{lower}}$	0.59	1.26
$c_{d_{upper}}$	−0.01	0.01
$c_{d_{lower}}$	0.02	0.06

Tab. 2.2. Lift and drag coefficients for NACA0012-bi-airfoil with propeller disk, at $M_\infty=0.5$, $\alpha=2^0$.

Clearly visible is the large influence of the working propeller on the lift force acting on each of the two airfoils. In Fig. 2.35 we give the Mach number, pressure and entropy distribution as obtained for both cases. In the Mach number distribution (Fig. 2.35a) for the case with working propeller one clearly observes the Mach number increase and shock wave as introduced in the internal flow part, and the Mach number decrease in the external flow part. The imposed sources are such that the flow has developed from fully subsonic into transonic. In the pressure distribution (Fig. 2.35b) for the case with working propeller we observe that the assumed pressure jump appears indeed. Further, the corresponding entropy distribution (Fig. 2.35c) shows the assumed isentropy through the propeller. For both cases (propeller on and off), the entropy which is spuriously generated at the airfoil noses and convected downstream, is one order of magnitude larger than for the mono-airfoil cases. Cause of this is the non-smoothness of the grid at the noses of the bi-airfoil.

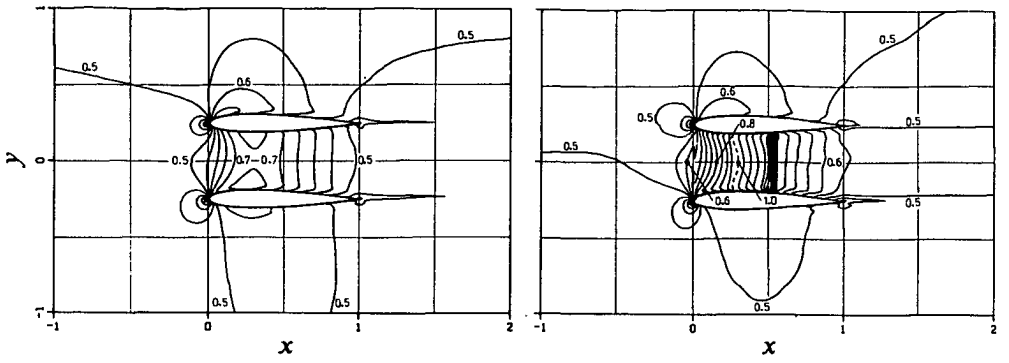

a. Mach number distributions.

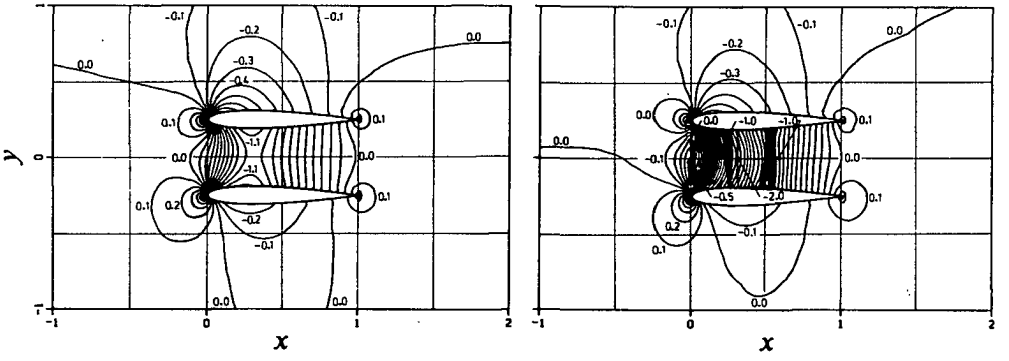

b. Pressure distributions (c_p).

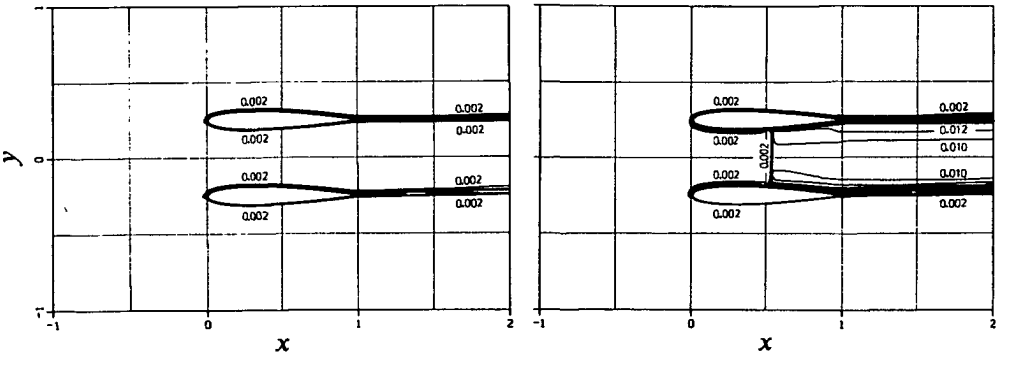

c. Entropy distributions ($s/s_\infty - 1$).

Fig. 2.35. Results bi-NACA0012-airfoil at $M_\infty = 0.5$, $\alpha = 2^0$, propeller off (left) and propeller on (right).

Efficiency. For all airfoil flows computed, we needed on an average five IDeC-cycles to drive the lift coefficients to within ½ % of their final values. On a CDC Cyber 205 on which we performed all our computations, in scalar mode, this took us $\sim 25\,ms$ per finite volume. Using a VAX 11/780, Jespersen with his nonlinear multigrid approach converges to a second-order accurate airfoil flow solution in $\sim 1100\,ms$ per grid point [14]. Taking into account the difference in performance between the CDC Cyber 205 and the VAX 11/780, both efficiencies seem to be about the same. Our solution quality, however, is better than Jespersen's. (Not expecting significant acceleration by vectorization, we did not optimize our code for efficient use on vector computers.) For large-scale computations, where all data cannot be kept in core, the small number of iteration cycles required (five IDeC-cycles on an average) results in a small number of out-of-core data transports and hence in low IO-times.

2.4. Concluding remarks

For the steady, two-dimensional Euler equations, an outlet boundary condition with total enthalpy or flow direction specified may easily yield a mathematically ill-posed problem. This is not the case for an outlet boundary condition with static pressure specified.

Grid adaptation by simply shifting the finite volumes in the nested iteration, without modifying the corresponding states, seems to work well for transonic applications.

The predicted better multigrid performance with Van Leer's flux splitting instead of Osher's flux difference splitting, in case of overall grid alignment of the flow [26], did come true. However, the better performance of Van Leer's flux splitting is not very significant.

Studying the behaviour of the nonlinear multigrid method for various smooth and non-smooth airfoil flow problems, it appears that a satisfactory degree of grid independence is obtained, as well as a satisfactory convergence to truncation error accuracy within a few cycles only. Although not significant, for airfoil flows Osher's scheme seems to lead to better multigrid convergence than Van Leer's.

Studying the behaviour of the defect correction iteration for various higher-order schemes, it appears that the centred and one-sided scheme lead to divergence for the basic flow problem considered: a transonic airfoil flow with shock wave. For this problem, the other schemes considered; the third-order scheme, the superbox scheme, and the Van Albada scheme, all give convergence. These converging schemes give sharp discontinuities, but they introduce wiggles, already after the first IDeC-cycle. However, for the Van Albada scheme the wiggles disappear within only a few IDeC-cycles. Comparison with standard reference results shows that for flows with discontinuities, within a few IDeC-cycles only, we obtain solutions of the same good quality with a finest grid which may be twice as coarse (in both directions) than those applied for the reference results. For smooth subcritical problems the third-order, the superbox, and the Van Albada scheme behave in the same way; within a few IDeC-cycles only, they yield solutions of good quality. For all airfoil flows considered, the Kutta condition is satisfied automatically.

τ-extrapolation appears to be a very useful multigrid tool for improving the solution accuracy. Studying its possibilities for shock-free airfoil flows, it appears that it can drastically reduce spurious drag. (Disregarding the non-smooth flow parts, the accuracy of a non-smooth flow solution might also benefit of it.)

Looking back at the Euler flow results obtained, especially at those obtained for the practically relevant and mathematically well-posed NACA0012-cases, it can be concluded, in particular when making comparisons with reference results, that the Hemker-Spekreijse method probably is a good starting point for the development of an accurate and efficient numerical method for the steady, two-dimensional Navier-Stokes equations, within the Reynolds number range and Mach number range indicated (section 1.4.1).

REFERENCES

1. G.D. VAN ALBADA, B. VAN LEER AND W.W. ROBERTS, *A Comparative Study of Computational Methods in Cosmic Gasdynamics,* Astron. Astrophys. 108, 76-84 (1982).
2. A. BAYLISS AND E. TURKEL, *Numerical Boundary Condition Procedures,* NASA-CP-2201 (NASA, Moffett Field, 1981).
3. J.W. BOERSTOEL AND G.H. HUIZING, *Transonic Shock-Free Aerofoil Design by an Analytic Hodograph Method,* AIAA paper 74-539 (1974).
4. A. BRANDT, *Guide to Multigrid Development,* in Multigrid Methods, Proceedings, Köln-Porz, 1981, Lecture Notes in Mathematics Vol. 960, 220-312, edited by W. Hackbusch and U. Trottenberg (Springer, Berlin, 1982).
5. S.R. CHAKRAVARTHY AND S. OSHER, *Computing with High-Resolution Upwind Schemes for Hyperbolic Equations,* in Large-Scale Computations in Fluid Mechanics, Proceedings of the 15th AMS-SIAM Summer Seminar on Applied Mathematics, Scripps Institution of Oceanography, 1983, Lectures in Applied Mathematics Vol. 22, Part 1, 57-86, edited by B.E. Engquist et al. (Amer. Math. Soc., Providence, RI, 1985).
6. L.E. ERIKSSON AND A. RIZZI, *Computer-Aided Analysis of the Convergence to Steady State of Discrete Approximations to the Euler Equations,* J. Comput. Phys. 57, 90-128 (1985).
7. P.M. GRESHO AND R.L. LEE, *Don't suppress the Wiggles - They're telling You Something !* Comput. and Fluids 9, 223-253 (1981).
8. W. HACKBUSCH, *Multi-Grid Methods and Applications* (Springer, Berlin, 1985).
9. P.W. HEMKER, *Defect Correction and Higher Order Schemes for the Multi Grid Solution of the Steady Euler Equations,* in Multigrid Methods II, Proceedings of the Second European Conference on Multigrid Methods, Cologne, 1985, Lecture Notes in Mathematics Vol. 1228, 149-165, edited by W. Hackbusch and U. Trottenberg (Springer, Berlin, 1986).
10. P.W. HEMKER AND B. KOREN, *A Non-Linear Multigrid Method for the Steady Euler Equations,* in Notes on Numerical Fluid Mechanics Vol. xx, edited by A. Dervieux et al. (Vieweg, Braunschweig, to appear).

11. P.W. HEMKER, B. KOREN AND B. VAN LEER, *A Grid-Decoupled, Rotated Upwind Scheme for the Multi-Dimensional Euler Equations* (in preparation).
12. P.W. HEMKER, B. KOREN AND S.P. SPEKREIJSE, *A Nonlinear Multigrid Method for the Efficient Solution of the Steady Euler Equations,* in Proceedings of the 10th International Conference on Numerical Methods in Fluid Dynamics, Beijing, 1986, Lecture Notes in Physics Vol. 264, 308-313, edited by F.G. Zhuang and Y.L. Zhu (Springer, Berlin, 1986).
13. P.W. HEMKER AND S.P. SPEKREIJSE, *Multiple Grid and Osher's Scheme for the Efficient Solution of the Steady Euler Equations,* Appl. Numer. Math. 2, 475-493 (1986).
14. D.C. JESPERSEN, *Design and Implementation of a Multigrid Code for the Euler Equations,* Appl. Math. Comput. 13, 357-374 (1983).
15. B. KOREN, *Defect Correction and Multigrid for an Efficient and Accurate Computation of Airfoil Flows,* J. Comput. Phys. 77, 183-206 (1988).
16. B. KOREN, *Euler Flow Solutions for a Transonic Wind Tunnel Section,* in Proceedings of High Speed Aerodynamics II, Aachen, 1987, edited by A. Nastase (Haag und Herchen, Frankfurt, to appear).
17. B. KOREN, *Euler Flow Solutions for Transonic Shock Wave - Boundary Layer Interaction,* Int. J. Numer. Methods in Fluids 9, 59-73 (1989).
18. B. KOREN, Centre for Mathematics and Computer Science, Amsterdam, private communication (1986).
19. B. KOREN AND S.P. SPEKREIJSE, *Multigrid and Defect Correction for the Efficient Solution of the Steady Euler Equations,* in Research in Numerical Fluid Mechanics, Proceedings of the 25th Meeting of the Dutch Association for Numerical Fluid Mechanics, Delft, 1986, Notes on Numerical Fluid Mechanics Vol. 17, 87-100, edited by P. Wesseling (Vieweg, Braunschweig, 1987).
20. B. KOREN AND S.P. SPEKREIJSE, *Solution of the Steady Euler Equations by a Multigrid Method,* in Multigrid Methods, Theory, Applications, and Supercomputing, Proceedings of the Third Copper Mountain Conference on Multigrid Methods, Copper Mountain, 1987, Lecture Notes in Pure and Applied Mathematics Vol. 110, 323-336, edited by S.F. McCormick (Dekker, New York, 1988).
21. B. VAN LEER, *Flux-Vector Splitting for the Euler Equations,* in Proceedings of the Eighth International Conference on Numerical Methods in Fluid Dynamics, Aachen, 1982, Lecture Notes in Physics Vol. 170, 507-512, edited by E. Krause (Springer, Berlin, 1982).
22. C. MORAWETZ, *On the Non-Existence of Continuous Transonic Flows past Airfoils I,* Comm. Pure Appl. Math. 9, 45-68 (1956).
23. C. MORAWETZ, *On the Non-Existence of Continuous Transonic Flows past Airfoils II,* Comm. Pure Appl. Math. 10, 107-131 (1957).
24. C. MORAWETZ, *On the Non-Existence of Continuous Transonic Flows past Airfoils III,* Comm. Pure Appl. Math. 11, 129-144 (1958).
25. C. MORAWETZ, *Non-Existence of Transonic Flow past a Profile,* Comm. Pure Appl. Math. 17, 357-367 (1964).

26. W.A. MULDER, *Analysis of a Multigrid Method for the Euler Equations of Gas Dynamics in Two Dimensions,* in Multigrid Methods, Theory, Applications, and Supercomputing, Proceedings of the Third Copper Mountain Conference on Multigrid Methods, Copper Mountain, 1987, Lecture Notes in Pure and Applied Mathematics Vol. 110, 467-489, edited by S.F. McCormick (Dekker, New York, 1988).
27. M. VAN DER NAT, *De Stationaire, Compressibele, Niet-Viskeuze Stroming om het Profiel NLR7301 bij Ma* $=.721$ *en* $\alpha = -.194^0$ *(2-dimensionaal),* National Aerospace Laboratory, Amsterdam, Memorandum AT-88-009 U (unpublished, 1988).
28. C. NEBBELING AND W.J. BANNINK, *A Curved Test Section for Research on Transonic Shock Wave - Boundary Layer Interaction,* Delft University of Technology, LR-414 (unpublished, 1984).
29. C. NEBBELING AND B. KOREN, *Transonic Shock Wave - Turbulent Boundary Layer Interaction on a Curved Surface,* Delft Progr. Rep. 12, 365-380 (1988).
30. S. OSHER AND F. SOLOMON, *Upwind Difference Schemes for Hyperbolic Systems of Conservation Laws,* Math. Comput. 38, 339-374 (1982).
31. H.H. PEARCEY, *The Aerodynamic Design of Section Shapes for Swept Wings,* Advances in Aeronautical Sciences, 3, 277 (1962).
32. A. RIZZI AND H. VIVIAND, *Numerical Methods for the Computation of Inviscid Transonic Flows with Shock Waves,* Notes on Numerical Fluid Mechanics Vol. 3 (Vieweg, Braunschweig, 1981).
33. S.P. SPEKREIJSE, *Multigrid Solution of Monotone Second-Order Discretizations of Hyperbolic Conservation Laws,* Math. Comput. 49, 135-155 (1987).
34. S.P. SPEKREIJSE, Centre for Mathematics and Computer Science, Amsterdam, private communication (1986).
35. P.K. SWEBY, *High Resolution Schemes using Flux Limiters for Hyperbolic Conservation Laws,* SIAM J. Numer. Anal. 21, 995-1011 (1984).
36. H. VIVIAND, *Numerical Solutions of Two-Dimensional Reference Test Cases,* in AGARD-AR-211 (AGARD, Neuilly sur Seine, 1985).
37. J. ZIEREP, *Der Senkrechte Verdichtungsstoss am Gekrümmten Profil,* ZAMP, 9b, 764-776 (1958).

Chapter 3

Numerical Method for the Steady Navier-Stokes Equations

3.1. Introductory remarks

Taking the Hemker-Spekreijse method as a point of departure for developing an accurate and efficient numerical method for the steady Navier-Stokes equations, two existing Navier-Stokes methods stand out immediately; (i) the highly accurate method as introduced by Chakravarthy et al. [1], and (ii) the highly efficient method as introduced by Shaw and Wesseling [17].

The method presented in [1] applies monotone, high-accurate upwind schemes for the convective terms and, consistently, a high-accurate biased scheme for the diffusive terms; the bias taking into proper account the preferential direction of the cross derivative terms. Although this particular diffusive discretization is favourable for the diagonal dominance and hence the solvability of the complete discrete system, from a viewpoint of efficiency, due to its complexity, it is unfavourable.

About the opposite holds for the method presented in [17]. There, only first-order discretized Navier-Stokes equations are considered, but for solving these equations a very efficient technique is applied. The technique is basically the same as that applied by Hemker and Spekreijse to the first-order discretized Euler equations [7], but has much better vectorization properties. Analogous to the Hemker-Spekreijse method, it applies collective symmetric point Gauss-Seidel relaxation as the smoothing technique and nonlinear multigrid as the acceleration technique. For an additional speed-up by vectorization, instead of Osher's scheme [15], Shaw and Wesseling apply Van Leer's scheme [12] with its less extensive conditional branching. Further, they avoid the recursiveness of the point Gauss-Seidel relaxation by discretizing on seven-point stencils and by making relaxation sweeps over diagonal grid lines.

In this chapter we introduce and analyze a middle-of-the-road method when compared to the previous two; it finds a better compromise between accuracy and efficiency. The analyses to be presented have appeared (or will soon appear) in [6,8,9,10,11].

3.2. Discretization method

To still allow Euler flow solutions with discontinuities, we also discretize the full Navier-Stokes equations (1.6) in their integral form. Analogous to the Euler equations, a straightforward and simple discretization of this form is obtained by subdividing the computational domain Ω into quadrilateral finite volumes $\Omega_{i,j}$ $i=1,2,...,I$, $j=1,2,...,J$, and by requiring the conservation laws to hold for each finite volume separately:

$$\oint_{\partial\Omega_{i,j}} (f(q)n_x + g(q)n_y)ds - \frac{1}{Re} \oint_{\partial\Omega_{i,j}} (r(q)n_x + s(q)n_y)ds = 0, \ \forall i,j. \tag{3.1}$$

This discretization requires an evaluation of convective and diffusive fluxes at each volume wall. Since we are interested in high-Reynolds number flows, the evaluation of the convective fluxes requires most attention. To simplify the optimization of the latter, it is convenient that the less important evaluation of the diffusive fluxes is already fixed.

3.2.1. Diffusion

For the evaluation of the diffusive fluxes, it is necessary to compute ∇u, ∇v and ∇c^2 at each cell face. To compute for instance $(\nabla u)_{i+\frac{1}{2},j}$, where $i+\frac{1}{2},j$ refers to the cell face separating $\Omega_{i,j}$ and $\Omega_{i+1,j}$, we use the Gauss theorem

$$\nabla u_{i+\frac{1}{2},j} = \frac{1}{A_{i+\frac{1}{2},j}} \oint_{\partial\Omega_{i+\frac{1}{2},j}} und s, \tag{3.2}$$

with $\partial\Omega_{i+\frac{1}{2},j}$ the boundary, n the outward unit normal and $A_{i+\frac{1}{2},j}$ the area of a shifted quadrilateral finite volume $\Omega_{i+\frac{1}{2},j}$ (Fig. 3.1), of which the vertices $z \equiv (x,y)^T$ are defined by

$$z_{i,j\pm\frac{1}{2}} \equiv \frac{1}{2}(z_{i-\frac{1}{2},j\pm\frac{1}{2}} + z_{i+\frac{1}{2},j\pm\frac{1}{2}}), \tag{3.3}$$

and a similar expression for $z_{i+1,j\pm\frac{1}{2}}$.

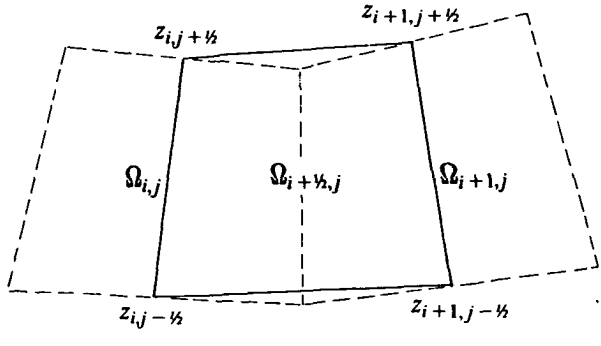

Fig. 3.1. Shifted finite volume $\Omega_{i+\frac{1}{2},j}$.

The line integral in (3.2) is approximated by

$$\begin{aligned}\oint_{\partial\Omega_{i+\frac{1}{2},j}} u n ds = \; & u_{i+1,j} \quad (z^{\perp}_{i+1,j+\frac{1}{2}} - z^{\perp}_{i+1,j-\frac{1}{2}}) + \\ & u_{i+\frac{1}{2},j+\frac{1}{2}} \quad (z^{\perp}_{i,j+\frac{1}{2}} - z^{\perp}_{i+1,j+\frac{1}{2}}) + \\ & u_{i,j} \quad (z^{\perp}_{i,j-\frac{1}{2}} - z^{\perp}_{i,j+\frac{1}{2}}) + \\ & u_{i+\frac{1}{2},j-\frac{1}{2}} \quad (z^{\perp}_{i+1,j-\frac{1}{2}} - z^{\perp}_{i,j-\frac{1}{2}}),\end{aligned} \tag{3.4}$$

with $z^{\perp} \equiv (y, -x)^T$ and with for $u_{i+\frac{1}{2},j\pm\frac{1}{2}}$ the central expression

$$u_{i+\frac{1}{2},j\pm\frac{1}{2}} = \frac{1}{4}(u_{i,j} + u_{i,j\pm1} + u_{i+1,j} + u_{i+1,j\pm1}). \tag{3.5}$$

Similar expressions are used for the other gradients and other walls. For sufficiently smooth grids this central diffusive flux computation is second-order accurate. Notice that by using central expressions, like (3.5), the directional dependence coming from the cross derivative terms is neglected. For high-Reynolds number flows, our interest, no significant gain in solution quality is expected from a biased approach as proposed in [1]. For these flows, such a sophisticated discretization of the diffusion operator seems to be a little bit over-abundant in addition to an already sophisticated treatment of convection. Because of the fact that the present diffusive flux evaluation is rather cheap, use of rotational invariance for the diffusive operator is hardly advantageous and therefore not applied.

3.2.2. Convection

Based on our experience with the Euler equations (see [5] for an overview), for the evaluation of the convective fluxes we prefer an upwind approach following the Godunov principle [2]. So - again - along each finite volume wall, the convective flux is assumed to be constant and to be determined by a uniformly constant left and right state only. To the one-dimensional Riemann problem thus obtained, an approximate Riemann solver is applied again. The choice of the left and right state, to be used as input for the approximate Riemann solver, determines again the accuracy of the convective discretization. Analogous to the Euler equations, first-order accuracy is obtained by taking the left and right state equal to that in the corresponding adjacent volume, and higher-order accuracy by applying low-degree piecewise polynomial state interpolation, using two or three adjacent volume states for the left and right state separately. Monotonicity is guaranteed again by applying an appropriate limiter. For the convective flux evaluation, we do make use of the rotational invariance of the Navier-Stokes equations in order to reduce the number of these evaluations per cell face from two to one. We proceed in analyzing the convective discretization in more detail.

Approximate Riemann solver. As approximate Riemann solver, we prefer again a scheme which is continuously differentiable, and which is consistent along boundaries, like Osher's scheme. The question arises whether it is still a good choice to use an approximate Riemann solver like Osher's when, besides discontinuities, also typical Navier-Stokes features such as shear, separation and heat conduction have to be resolved. We therefore reconsider the choice of an approximate Riemann solver for the present application.

Since continuous differentiability is an absolute requirement for the success of our solution method, and since the only known approximate Riemann solvers with this property are Osher's and Van Leer's, our choice is confined to these two only. So far, Van Leer's scheme is more widespread in the field of Navier-Stokes than Osher's [16,17,20]. Probably, the main reason for this is its greater conceptual and operational simplicity.

Given the moderate differences observed between both schemes with respect to multigrid performance (chapter 2), only the requirement of accurate modelling of physical diffusion will determine our choice. In [12], Van Leer stated already that his flux vector splitter cannot preserve steady contact discontinuities. It diffuses contact discontinuities which, as linear wave phenomena, have no intrinsic steepening mechanism counteracting this diffusion. Since a discrete shear layer may be interpreted as a layer of contact discontinuities, doubt arose about the suitability of Van Leer's scheme for Navier-Stokes codes. Recently, this doubt was confirmed in [13], in which a qualitative analysis is presented (supplemented with numerical experiments) for various upwind schemes. There, for the resolution of boundary layer flows, Osher's scheme turns out to be better than Van Leer's scheme indeed.

To shed some more light on the difference in quality, here we present a quantitative error analysis for both Osher's and Van Leer's scheme. The analysis is confined to the steady, two-dimensional, isentropic Euler equations for a perfect gas with $\gamma=1$:

$$\frac{\partial f(q)}{\partial x} + \frac{\partial g(q)}{\partial y} = 0, \tag{3.6a}$$

with

$$f(q) = \begin{bmatrix} \rho u \\ \rho(u^2+c^2) \\ \rho uv \end{bmatrix}, \quad g(q) = \begin{bmatrix} \rho v \\ \rho vu \\ \rho(v^2+c^2) \end{bmatrix}, \tag{3.6b}$$

where the speed of sound c is constant. (The choice of two-dimensional equations allows us to consider a boundary layer flow in the analysis.) For both upwind schemes, we derive the system of modified equations, considering (i) a first-order accurate, finite volume discretization on a square grid with mesh size h (Fig. 2.8), and (ii) a subsonic flow with u and v positive, and $\rho \approx$ constant. (The discretization is first-order accurate for simplicity and for allowing a good display of the differences between both upwind schemes.)

To construct the Osher scheme for the above flux vector $f(q)$, we consider the quasilinear form

$$\frac{\partial}{\partial t}\begin{bmatrix}\rho\\ u\\ v\end{bmatrix}+\begin{bmatrix}u & \rho & 0\\ c^2/\rho & u & 0\\ 0 & 0 & u\end{bmatrix}\frac{\partial}{\partial x}\begin{bmatrix}\rho\\ u\\ v\end{bmatrix}=0. \tag{3.7}$$

From this form, we find directly as the eigenvalues of the Jacobian $\frac{df(q)}{dq}$:

$$\lambda_1=u-c, \qquad \lambda_2=u, \qquad \lambda_3=u+c, \tag{3.8}$$

and as corresponding eigenvectors:

$$r_1=\begin{bmatrix}\rho\\ -c\\ 0\end{bmatrix}, \quad r_2=\begin{bmatrix}0\\ 0\\ 1\end{bmatrix}, \quad r_3=\begin{bmatrix}\rho\\ c\\ 0\end{bmatrix}. \tag{3.9}$$

For the Riemann invariants ψ_k^1, $k=2,3$, satisfying

$$\rho\frac{\partial\psi_k^1}{\partial\rho}-c\frac{\partial\psi_k^1}{\partial u}=0, \tag{3.10a}$$

we find directly: $\psi_2^1=v$, and by separation of variables: $\psi_3^1=\rho e^{u/c}$. For ψ_k^2, $k=1,3$, satisfying

$$\frac{\partial\psi_k^2}{\partial v}=0, \tag{3.10b}$$

we find directly: $\psi_1^2=\rho$ and $\psi_3^2=u$. Similar to ψ_k^1, for ψ_k^3, $k=1,2$, satisfying

$$\rho\frac{\partial\psi_k^3}{\partial\rho}+c\frac{\partial\psi_k^3}{\partial u}=0, \tag{3.10c}$$

we find: $\psi_1^3=v$ and $\psi_2^3=\rho e^{-u/c}$. Using then the P-arrangement of subpaths [7], for the flux $f(q)$ given in (3.6b), Osher's scheme can be represented schematically as in Fig. 3.2.

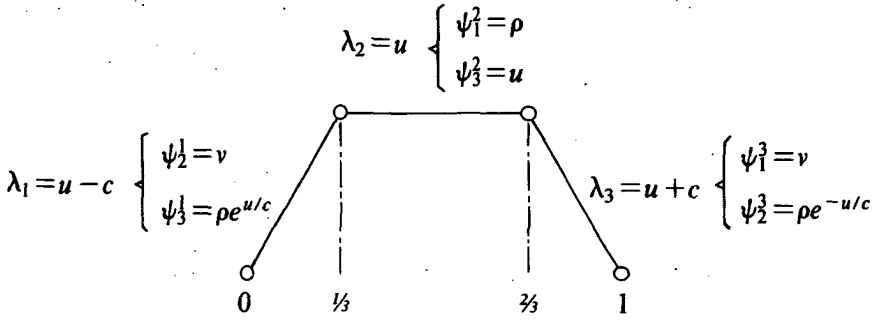

Fig. 3.2. Osher path (P-variant) for $f=(\rho u,\rho(u^2+c^2),\rho uv)^T$, $c=$constant.

Writing Osher's flux function $F(q_0,q_1)$ as

$$F(q_0,q_1) = f(q_0) + \int_{q_0}^{q_1} \frac{df^-(q)}{dq} dq, \tag{3.11}$$

$\frac{df^-(q)}{dq}$ being the part of $\frac{df(q)}{dq}$ which corresponds with the negative eigenvalue λ_1, for the given P-type arrangement of subpaths and for the subsonic flow considered, we find directly

$$F(q_0,q_1) = f(q_{1/2}). \tag{3.12}$$

For $q_{1/2} = (\rho_{1/2}, u_{1/2}, v_{1/2})^T$, by straightforward arithmetic we find

$$q_{1/2} = \begin{bmatrix} \sqrt{\rho_0 \rho_1 e^{(u_0-u_1)/c}} \\ \frac{1}{2}\{u_0+u_1+c\ln(\rho_0/\rho_1)\} \\ v_0 \end{bmatrix}. \tag{3.13}$$

With the simple finite-volume grid proposed, and with the neglect of density variation in the error terms, we find then as system of modified equations for Osher's scheme

$$\frac{\partial f(q)}{\partial x} + \frac{\partial g(q)}{\partial y} - h\frac{\rho}{2c}\left[\frac{\partial}{\partial x}\begin{bmatrix} \frac{1}{2}\frac{\partial(u^2)}{\partial x} \\ (u^2+c^2)\frac{\partial u}{\partial x} \\ uv\frac{\partial u}{\partial x} + uc\frac{\partial v}{\partial x} \end{bmatrix} + \frac{\partial}{\partial y}\begin{bmatrix} \frac{1}{2}\frac{\partial(v^2)}{\partial y} \\ vu\frac{\partial v}{\partial y} + vc\frac{\partial u}{\partial y} \\ (v^2+c^2)\frac{\partial v}{\partial y} \end{bmatrix}\right] + O(h^2) = 0. \tag{3.14}$$

With Van Leer's scheme the flux $f(q)$ is split in a forward flux $f^+(q)$ and a backward flux $f^-(q)$, such that $\frac{df^+(q)}{dq}$ has all positive eigenvalues and $\frac{df^-(q)}{dq}$ all negative eigenvalues. (The additional restrictions imposed on the splitting are listed in [12].) For the subsonic flow and the specific $f(q)$ considered, Van Leer's splitting yields

$$f^+(q) = \frac{1}{4}\rho\frac{(u+c)^2}{c}\begin{bmatrix} 1 \\ 2c \\ v \end{bmatrix}, \tag{3.15}$$

with $f^-(q) \equiv f(q) - f^+(q)$. Then, with the square model grid and with the neglect of density variation, we find the following system of modified equations for Van Leer's scheme

$$\frac{\partial f(q)}{\partial x} + \frac{\partial g(q)}{\partial y} -$$

$$h\frac{\rho}{2c}\left[\frac{\partial}{\partial x}\begin{bmatrix}\frac{1}{2}\frac{\partial(u^2)}{\partial x}\\ 2c^2\frac{\partial u}{\partial x}\\ \frac{1}{2}\frac{\partial((u^2+c^2)v)}{\partial x}\end{bmatrix} + \frac{\partial}{\partial y}\begin{bmatrix}\frac{1}{2}\frac{\partial(v^2)}{\partial y}\\ \frac{1}{2}\frac{\partial((v^2+c^2)u)}{\partial y}\\ 2c^2\frac{\partial v}{\partial y}\end{bmatrix}\right] + O(h^2) = 0. \qquad (3.16)$$

To compare now the error terms in (3.14) and (3.16), we consider an incompressible, semi-infinite flat plate flow (Fig. 3.3).

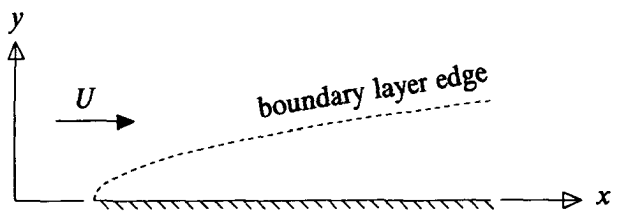

Fig. 3.3. Semi-infinite, incompressible flat plate flow.

As flow solution, instead of the analytically intractable Blasius solution, we use Lamb's approximate solution. Lamb's approximation, which shows a better resemblance with the Blasius solution than for instance Pohlhausen's (Fig. 3.4), reads

$$\begin{bmatrix}\rho\\ u\\ v\end{bmatrix} = \begin{bmatrix}P\\ U\sin\left(\frac{\pi}{2}\frac{\sqrt{Re/x}}{5}y\right)\\ \frac{y}{2x}u(x,y)+\frac{5}{\pi}\frac{U}{\sqrt{Rex}}\left\{\cos\left(\frac{\pi}{2}\frac{\sqrt{Re/x}}{5}y\right)-1\right\}\end{bmatrix}, \qquad (3.17)$$

with P and U constant.

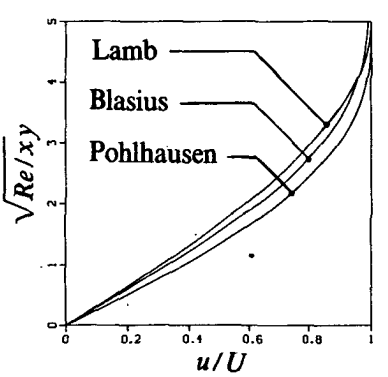

Fig. 3.4. Velocity profiles; exact (Blasius) and approximate (Lamb and Pohlhausen).

Substituting the solution vector (3.17) into the O(h)-error vector of both (3.14) and (3.16), considering the boundary layer edge

$$y = \delta(x) \equiv \frac{5}{\sqrt{Re/x}} \tag{3.18}$$

at $x=1$, and taking componentwise the ratio of absolute values of both error vectors, using $Re \gg 1$ (our interest), we find

$$\frac{\text{error Osher}}{\text{error Van Leer}} = \begin{bmatrix} 1 \\ (1-\frac{2}{\pi})\frac{5}{\sqrt{Re}}\frac{U}{c} \\ 1/2 \end{bmatrix}, \tag{3.19}$$

From (3.19) it appears that Van Leer's scheme deteriorates compared to Osher's scheme for increasing Re. Assuming (3.19) to be still reliable for small Re, it appears that already for $Re > \{5(1-2/\pi)U/c\}^2$, where $U/c < 1$, Osher's scheme is to be preferred above Van Leer's scheme.

As can be seen from (3.19), the cause of the deterioration of Van Leer's scheme lies in the discretization of the x-momentum equation. Recently, Hänel [4] introduced a remedy for this deficiency. The remedy consists of a modification of Van Leer's splitting of the x-momentum flux.

Solid wall boundary condition treatment. To ensure a continuous transition along a solid wall boundary from the Navier-Stokes flow regime to the Euler flow regime, for Van Leer's scheme it might be necessary to impose on the convective part only the Euler boundary condition. For a non-permeable solid wall this means that one should only impose a zero normal velocity component on the convective part (in contrast to the diffusive part on which all boundary conditions are to be imposed, i.e. a zero normal and tangential velocity component, and a temperature condition). By not imposing the no-slip and temperature boundary condition on the convective part, we avoid that it 'feels' the severe contact discontinuity in the realistic case of a boundary layer flow on a coarse grid and an outer flow with M not small. Such a contact discontinuity might be erroneously spread by Van Leer's scheme, and cause the solution to be insensitive to Re-variation above some finite, rather low value of Re. Osher's scheme can preserve a steady contact discontinuity, as long as it is aligned with the grid. Application of (commonly used) body-fitted grids guarantees this alignment along solid walls. Therefore, with a body-fitted grid, Osher's scheme probably does not need this careful solid wall - boundary condition treatment.

On the other hand, for hypersonic flow computations Osher's boundary condition treatment at solid, impermeable walls [7,14] needs to be protected against an extrapolation leading to an unphysical expansion beyond vacuum; cavitation. For the situation with a solid wall boundary at the left e.g., Osher's scheme yields

$$(u_B, v_B, c_B, z_B)^T = (0, v_1, c_1 - \frac{\gamma-1}{2}u_1, z_1)^T, \tag{3.20}$$

where $(u_B,v_B,c_B,z_B)^T$ is the unknown boundary state, and $(u_1,v_1,c_1,z_1)^T$ the known inner state. In a qualitatively correct way, (3.20) leads to a compression towards the wall for $u_1<0$, and vice versa an expansion for $u_1>0$. However, for $\gamma=7/5$ and $u_1/c_1>5$, a situation that may easily occur at the beginning of the solution process when considering a di-atomic gas and a uniformly constant, hypersonic initial solution, (3.20) yields: $c_B<0$. If $u_1/c_1>2/(\gamma-1)$, as a safeguard against cavitation, we switch from (3.20) to the less sophisticated but safer mirror principle

$$(u_B, v_B, c_B, z_B)^T = (-u_1, v_1, c_1, z_1)^T. \tag{3.21}$$

Higher-order accuracy. Analogous to the Euler equations (section 1.5.3 and 2.3.2), higher-order accuracy is obtained by applying low-degree piecewise polynomial functions through two or three adjacent volume states, namely the polynomials given by (1.17). (Since consistency along boundaries is already affected by the discretization chosen for the diffusive terms, here we refrain from applying the superbox scheme.)

The aim now is to optimize κ from the viewpoint of accuracy, just like in section 2.3.2. For this purpose, here we consider the scalar model equation

$$\frac{\partial u}{\partial x} + \frac{\partial u}{\partial y} - \epsilon\left(\frac{\partial^2 u}{\partial x^2}+\frac{\partial^2 u}{\partial x\partial y}+\frac{\partial^2 u}{\partial y^2}\right) = 0. \tag{3.22}$$

On a square grid (Fig. 2.8), a finite volume discretization using the κ-scheme for convection and the central scheme for diffusion, yields as modified equation

$$\begin{aligned}&\frac{\partial u}{\partial x} + \frac{\partial u}{\partial y} - \epsilon\left(\frac{\partial^2 u}{\partial x^2}+\frac{\partial^2 u}{\partial x\partial y}+\frac{\partial^2 u}{\partial y^2}\right) + \\ &h^2\left[\frac{\kappa-\frac{1}{3}}{4}\left(\frac{\partial^3 u}{\partial x^3}+\frac{\partial^3 u}{\partial y^3}\right)-\right. \\ &\left.\frac{\epsilon}{12}\left(\frac{\partial^4 u}{\partial x^4}+2\frac{\partial^4 u}{\partial x^3\partial y}+2\frac{\partial^4 u}{\partial x\partial y^3}+\frac{\partial^4 u}{\partial y^4}\right)\right]+O(h^3) = 0.\end{aligned} \tag{3.23}$$

Assuming the reliability of the underlying Taylor series expansion, from (3.23) we find as the highest-accuracy value of κ:

$$\kappa = \frac{1}{3}\left[1+\epsilon\frac{\frac{\partial^4 u}{\partial x^4}+2\frac{\partial^4 u}{\partial x^3\partial y}+2\frac{\partial^4 u}{\partial x\partial y^3}+\frac{\partial^4 u}{\partial y^4}}{\frac{\partial^3 u}{\partial x^3}+\frac{\partial^3 u}{\partial y^3}}\right], \tag{3.24}$$

leading to third-order truncation error accuracy. So even with the second-order accurate diffusive discretization, the complete discretization can be made third-order accurate by choosing this diffusion-dependent κ. (We notice that with (3.24), for the evaluation of the higher-order cell face fluxes over the complete computational domain, it is convenient to do this volume by volume in a checkerboard-fashion, instead of cell face by cell face.) However, since convection dominated problems, problems with $\epsilon\ll 1$, are our interest, we will simply neglect the above diffusion-dependence of κ, which leads us again to $\kappa=\frac{1}{3}$.

Monotonicity. To preserve monotonicity of the solution, we construct a limiter which is consistent with the $\kappa=\frac{1}{3}$-scheme. For this, we apply the monotonicity theory of Spekreijse [18], an extension of Sweby's theory [19], allowing more freedom in the limiter construction.

For the limited, higher-order, left and right state vector components we consider (2.13). Then, the limited $\kappa=\frac{1}{3}$-scheme can be written as

$$q_{i+\frac{1}{2},j}^{l(k)} = q_{i,j}^{(k)} + \frac{1}{2}\xi(R_{i,j}^{(k)})(\frac{1}{3}+\frac{2}{3}R_{i,j}^{(k)})(q_{i,j}^{(k)}-q_{i-1,j}^{(k)}), \tag{3.25a}$$

$$q_{i+\frac{1}{2},j}^{r(k)} = q_{i+1,j}^{(k)} + \frac{1}{2}\xi(\frac{1}{R_{i+1,j}^{(k)}})(\frac{1}{3}+\frac{2}{3}\frac{1}{R_{i+1,j}^{(k)}})(q_{i+1,j}^{(k)}-q_{i+2,j}^{(k)}). \tag{3.25b}$$

Notice that for $\xi(R)\equiv 1$ we have the (non-limited) $\kappa=\frac{1}{3}$-scheme, and that $\xi(R)$ defines the limiter $\psi(R)$ by

$$\psi(R) = \xi(R)(\tfrac{1}{3}+\tfrac{2}{3}R). \tag{3.26}$$

General requirements to be fulfilled by $\xi(R)$ are: $\xi(1)=1$ to preserve higher-order accuracy, and: $\xi(0)=0$ and boundedness for large $|R|$ to preserve monotonicity. For the latter, we require that $\lim_{R\to\pm\infty}\xi(R)(\frac{1}{3}+\frac{2}{3}R)=1$. To make the limiter now consistent with the $\kappa=\frac{1}{3}$-scheme, we require that $\xi'(1)=0$. (This makes the limiter tangent to the $\kappa=\frac{1}{3}$-scheme at $R=1$ in the monotonicity domain.) Imposing these five requirements on the general form

$$\xi(R) = \frac{\alpha_1 R^2+\alpha_2 R+\alpha_3}{\alpha_4 R^2+\alpha_5 R+1}, \tag{3.27}$$

we find with (3.26)

$$\psi(R) = \frac{2R^2+R}{2R^2-R+2}. \tag{3.28}$$

An illustration of this new limiter is given in Fig. 3.5.

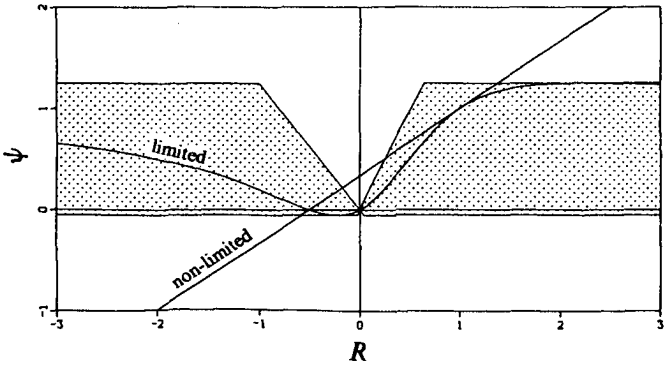

Fig. 3.5. Monotonicity domain with limited and non-limited $\kappa=\frac{1}{3}$-scheme.

3.3. SOLUTION METHOD

3.3.1. Relaxation

Derivative matrix. The first change that we propose for going from Euler to full Navier-Stokes is the extension of the derivative matrix (applied in the Newton iteration) with the full diffusive part coming from the Navier-Stokes equations. Notice that the state $(u,v,c,z)^T$ and the corresponding differential operator $(\partial/\partial u, \partial/\partial v, \partial/\partial c, \partial/\partial z)^T$, as conveniently introduced in [7] for the particular discretization of convection considered, are also very convenient for the diffusive part of the Navier-Stokes equations. We refrain here from listing all derivatives that are needed for the full Navier-Stokes relaxation.

Switch to evolution. The second change that we propose is a protection of the local Newton iteration against possible divergence. Divergence may occur in e.g. the very first visit to the stagnation region in case of (already) a medium-supersonic blunt body flow computation with as initial solution the uniform solution which continuously fits to the supersonic far-field boundary conditions. For supersonic flow computations starting with a poor initial solution, one may gain in robustness by introducing a continuation process preceding the nested iteration. In such a process, usually a single upstream boundary condition, for instance M_∞, is increased from some low initial value to its correct high value, while performing relaxation sweeps. Continuation processes like this require a tuning of both the initial value and the increment. For hypersonic flow problems e.g., proper tuning is difficult because of the fact that in these flows the condition number of the 4×4-derivative matrices used may be quite large. The larger the condition numbers, the larger are the perturbations in the iterates as induced by perturbations in the right-hand sides; right-hand side perturbations which may be quite large by themselves in hypersonic flow computations. The ill-conditioning occurring in hypersonic flow computations can be illustrated for the 4×4-derivative matrix $\nabla(\rho u, \rho u^2 + p, \rho uv, \rho u(e + p/\rho))$, where $\nabla \equiv (\partial/\partial u, \partial/\partial v, \partial/\partial c, \partial/\partial z)^T$, the differential operator applied in our solution method. Considering for simplicity $v = 0$ and $p = 1$, it clearly appears from Fig. 3.6 that the condition of $\nabla(\rho u, \rho u^2 + p, \rho uv, \rho u(e + p/\rho))$ becomes worse for $u/c \gtrsim 1.5$.

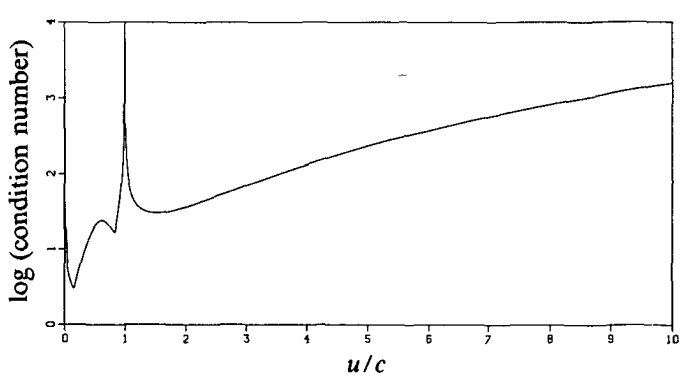

Fig. 3.6. Condition of typical derivative matrix to be inverted.

In all our (final) algorithms we want to avoid any tuning. Therefore, as a remedy for failure of the Newton process in the point relaxation method, we propose a local switched-relaxation-evolution technique. In this technique, we simply start applying the relaxation method, and take measures only as soon as the local Newton iteration fails. To discuss these measures for robustness improvement, we consider the local, first-order discrete Navier-Stokes system

$$\mathcal{F}_{i,j}(q_{i,j}) \equiv 0. \tag{3.29}$$

As a non-failing Newton iteration to solve $q_{i,j}$ from (3.29) we define now: a Newton iteration for which: (i)

$$\frac{|\mathcal{F}_{i,j}^{(k)}(q_{i,j}^{n+1})|}{|\mathcal{F}_{i,j}^{(k)}(q_{i,j}^{n})|} \leqslant 1, \quad k=1,2,3,4, \quad \forall_{i,j}, \tag{3.30}$$

for any n-th Newton iterate ($n=0,1,...,N$) and each of the four residual components, and for which (ii) each iterate $q_{i,j}^n$ is physically correct, with physical correctness defined in the following way. Considering the local iterate $q_{i,j}^n=(u_{i,j}^n, v_{i,j}^n, c_{i,j}^n, z_{i,j}^n)^T$ and the corresponding, possibly hypersonic, upstream state vector $q_\infty=(u_\infty, v_\infty, c_\infty, z_\infty)^T$, we know that the flow speed may not exceed the value corresponding with adiabatic expansion to vacuum, starting from upstream conditions:

$$(u_{i,j}^n)^2+(v_{i,j}^n)^2 \leqslant u_\infty^2+v_\infty^2+\frac{2}{\gamma-1}c_\infty^2, \quad \forall_{i,j}. \tag{3.31}$$

Further, we know that after this expansion, the speed of sound equals zero, its minimally allowable value:

$$c_{i,j}^n \geqslant 0, \quad \forall_{i,j}. \tag{3.32}$$

The maximally allowable value of the speed of sound is that corresponding with the stagnation temperature (which is the same for both isentropic and non-isentropic compression). For adiabatic flows we can write:

$$c_{i,j}^n \leqslant \sqrt{c_\infty^2+\frac{\gamma-1}{2}(u_\infty^2+v_\infty^2)}, \quad \forall_{i,j}. \tag{3.33}$$

For the lower limit of $z_{i,j}^n$ we can write directly with the entropy condition:

$$z_{i,j}^n \geqslant z_\infty, \quad \forall_{i,j}. \tag{3.34}$$

For the upper limit of $z_{i,j}^n$ we have to consider the state q_2 at the downstream side of a normal shock wave which has at its upstream side a state q_1 which has expanded to vacuum, departing from upstream conditions. Given the gas-dynamical relations

$$p_2 = \frac{2\gamma M_1^2-(\gamma-1)}{\gamma+1}\, p_1, \tag{3.35a}$$

$$\rho_2 = \frac{(\gamma+1)M_1^2}{(\gamma-1)M_1^2+2}\, \rho_1, \tag{3.35b}$$

$$p_1\rho_1^{-\gamma} = p_\infty\rho_\infty^{-\gamma}, \tag{3.35c}$$

it is clear that

$$z_{i,j}^n \leqslant \lim_{M_1 \to \infty} \ln(p_2 \rho_2^{-\gamma}) = \infty, \quad \forall_{i,j}. \tag{3.36}$$

Summarizing, we see that in adiabatic flows both the flow speed and the speed of sound have a physical lower and upper limit. The entropy only has a lower limit.

In the algorithm, (3.30)-(3.34) may be checked after each update in the Newton iteration. As soon as one or more of these five requirements are not satisfied, the Newton iteration is said to have failed, and any correction made is rejected. As the alternative for a failing Newton iteration, we apply then one or possibly two explicit time stepping schemes to the local, semi-discrete system

$$\frac{\partial q_{i,j}}{\partial t} + \frac{1}{A_{i,j}} \mathcal{F}_{i,j}(q_{i,j}) = 0. \tag{3.37}$$

where $A_{i,j}$ denotes the area of finite volume $\Omega_{i,j}$. As time stepping scheme to be applied first, we take the following version of Wambecq's explicit two-step rational Runge-Kutta scheme [21]:

$$q_{i,j}^{n+1} = q_{i,j}^n - \omega \frac{\tau_{i,j}^n}{A_{i,j}} \frac{\mathcal{F}_{i,j}^2(q_{i,j}^n)}{2\mathcal{F}_{i,j}(q_{i,j}^n) - \mathcal{F}_{i,j}(q_{i,j}^n - \tfrac{1}{2}\omega\tau_{i,j}^n / A_{i,j} \mathcal{F}_{i,j}(q_{i,j}^n))}, \quad n = 0, 1, \ldots, N, \tag{3.38}$$

with ω a possible damping factor for which we initially take $\omega = 1$, and with $\tau_{i,j}^n$ the local time step for which we safely take the one which is maximally allowed for the forward Euler scheme:

$$\tau_{i,j}^n = \frac{A_{i,j} h_{i,j}}{\sup \left| \dfrac{d\mathcal{F}_{i,j}(q_{i,j}^n)}{dq_{i,j}} \right|}, \tag{3.39}$$

with $h_{i,j}$ a characteristic local mesh size. Modelling the unsteady full Navier-Stokes operator as the scalar linear operator

$$\frac{\partial}{\partial t} + (\sqrt{u^2 + v^2} + c) \frac{\partial}{\partial x} - \frac{\gamma}{Pr} \frac{1}{Re} \frac{\partial^2}{\partial x^2}, \tag{3.40}$$

it can be verified that with a first-order upwind discretization of the convective term, $\tau_{i,j}^n$ satisfies

$$\tau_{i,j}^n = \min \left| \frac{h_{i,j}^2}{(\sqrt{(u_{i,j}^n)^2 + (v_{i,j}^n)^2} + c_{i,j}^n) h_{i,j} + 2 \dfrac{\gamma}{Pr} \dfrac{1}{Re}}, \right.$$

$$\left. \frac{(\sqrt{(u_{i,j}^n)^2 + (v_{i,j}^n)^2} + c_{i,j}^n) h_{i,j} + 2 \dfrac{\gamma}{Pr} \dfrac{1}{Re}}{(\sqrt{(u_{i,j}^n)^2 + (v_{i,j}^n)^2} + c_{i,j}^n)^2} \right|. \tag{3.41}$$

Notice that for $1/Re=0$ (the Euler equations), (3.41) correctly reduces to the relation

$$\tau_{i,j}^n = \frac{h_{i,j}}{\sqrt{(u_{i,j}^n)^2+(v_{i,j}^n)^2}+c_{i,j}^n}. \tag{3.42}$$

For the evaluation of the denominator in (3.38) we use the Samelson inverse of a vector:

$$\mathcal{G}^{-1} \equiv |\mathcal{G}|^{-2}\,\mathcal{G}, \tag{3.43}$$

$\mathcal{G}$ being a vector, whereas for the norm of a vector, we simply use the Cartesian inner product. As initial solution we take the same $q_{i,j}^0$ that just failed for the Newton iteration. The motivation for applying Wambecq's scheme is its good efficiency as demonstrated in [21] for a stiff and coupled system of four equations, which is what we may easily have in case of Newton's failure. However, a potential danger of (3.38) is that there is no guarantee for the denominator to be non-zero.

To protect Wambecq's scheme against a possibly too large time step, and against a (nearly) zero denominator, in each time step we require both the predictor and corrector to satisfy (3.31)-(3.34). As soon as a physically unrealistic value occurs, the time stepping is stopped immediately, rejecting any update made. Then, at first we assume that the unphysical result is due to a too large time step. Therefore, as a remedy we take $\omega=\frac{1}{2}$ and restart the time stepping with Wambecq's scheme, using the same $q_{i,j}^0$. In case of re-occurrence of something unphysical, we assume that the denominator was the problem. Therefore, as a new remedy, we restart with an explicit time stepping scheme which is safe in this sense; the simple forward Euler scheme

$$q_{i,j}^{n+1} = q_{i,j}^n - \omega\frac{\tau_{i,j}^n}{A_{i,j}}\mathcal{F}_{i,j}(q_{i,j}^n), \quad n=0,1,...,N. \tag{3.44}$$

For $\tau_{i,j}^n$ in (3.44), we apply again (3.41). Further, for ω we continue with $\omega=\frac{1}{2}$, and for $q_{i,j}^0$ we also take the same as before. When a physically unrealistic value (according to (3.31)-(3.34)) occurs again, ω is halved for the second time and the time stepping with forward Euler is restarted, still using the same $q_{i,j}^0$. In case of something unphysical once more, the time stepping is stopped and the finite volume visited is left without any update being made. (Notice that for both time stepping schemes, we do not require (3.30) to be satisfied.)

With the present switched-relaxation-evolution approach we expect that in those volumes where Newton possibly fails, the local evolution technique will bring the solution into the attraction domain of Newton (for the next sweep), and make itself quickly superfluous.

Since the monitoring proposed for the point relaxation increases the computational cost, at first one may perform a computation *without* any monitoring, so *without* a possible switch to point evolution. (We notice that the Euler flow results presented in chapter 2 were all obtained with this strategy.) If the strategy without switch to point evolution fails one may restart *with* the monitoring and *with* the possibility to switch to point evolution. In the next chapter we will follow this practice of doing at first a computation without any monitoring and any switch.

3.3.2. Multigrid

Transfer operators. The only change in the grid transfer operators that we introduce is the replacement of the piecewise constant correction prolongation by a bilinear prolongation, thus satisfying the multigrid rule that the sum of the order of prolongation and restriction should exceed the order of the differential equation [3]:

$$m_p + m_r > 2m, \tag{3.45}$$

with m_p and m_r denoting the order of accuracy of the prolongation and restriction, respectively, and with $2m$ denoting the order of the differential equation.

Smoothing analysis. For the first-order discretized Euler equations, collective symmetric point Gauss-Seidel relaxation turned out to be a good smoother, thus enabling a good multigrid acceleration. However, in general, for higher-order discretized Euler equations the good smoothing property is lost. As mentioned in section 1.5.3, the cause of this difference is the fact that the system of first-order discretized equations is always weakly diagonal dominant, whereas the system of higher-order discretized equations is not. Obviously, this difference will also exist for Navier-Stokes flows with high Reynolds number. We do not yet look for some remedy, but first, for both the first- and second-order discretized Navier-Stokes equations, we investigate how smoothing behaves as a function of the ratio between convection and diffusion.

To investigate the smoothing properties of point Gauss-Seidel relaxation, we perform Fourier analysis for a model equation. Since Fourier analysis cannot be applied to the full, steady, two-dimensional Navier-Stokes equations, here we can only obtain an indication of the smoothing properties that may be expected. For this purpose, we consider again the scalar, linear convection diffusion equation (3.22) of which the coefficient ϵ will be varied. We notice that the choice of both the convective operator's characteristic direction and the diffusive operator's eigendirection is arbitrary and fixed. The loss of generality by taking both directions fixed is compensated for by considering the four extreme relaxation directions; the downwind, the upwind and the two crosswind ones. Rigorous convergence studies are supposed to be possible only by performing numerical experiments with the full Navier-Stokes equations. Yet, pronounced (negative) results obtained by Fourier analysis will be taken sufficiently decisive to refrain from such experiments. As the integral form of (3.22) for finite volume $\Omega_{i,j}$, we consider

$$\oint_{\partial\Omega_{i,j}} (un_x + un_y)ds - \epsilon \oint_{\partial\Omega_{i,j}} \left(\frac{\partial u}{\partial x}n_x + \frac{\partial u}{\partial x}n_y + \frac{\partial u}{\partial y}n_y\right)ds = 0, \tag{3.46}$$

with $\partial\Omega_{i,j}$ the boundary of $\Omega_{i,j}$. The two parts of the Navier-Stokes discretization to be modelled further, are: (i) the upwind treatment of convection, either first- or higher-order accurate (non-limited $\kappa = 1/3$), and (ii) the central second-order accurate treatment of diffusion. Assuming again a finite volume grid with cell faces which are equidistant and parallel to the x- and y-axis (Fig. 2.8), the evaluation of convective flux terms yields:

$$\oint_{\partial\Omega_{ij}} un_x ds = (u^l_{i+\frac{1}{2},j} - u^l_{i-\frac{1}{2},j})h,$$
$$\oint_{\partial\Omega_{ij}} un_y ds = (u^l_{i,j+\frac{1}{2}} - u^l_{i,j-\frac{1}{2}})h, \tag{3.47a}$$

with

$$u^l_{i+\frac{1}{2},j} = \alpha_1 u_{i-1,j} + \alpha_2 u_{ij} + \alpha_3 u_{i+1,j},$$
$$u^l_{i,j+\frac{1}{2}} = \alpha_1 u_{ij-1} + \alpha_2 u_{ij} + \alpha_3 u_{ij+1}, \tag{3.47b}$$

and similar expressions for $u^l_{i-\frac{1}{2},j}$ and $u^l_{i,j-\frac{1}{2}}$ (the coefficients α_1, α_2 and α_3 still free). For the diffusive terms we get:

$$\oint_{\partial\Omega_{ij}} \frac{\partial u}{\partial x} n_x ds = \left[\left(\frac{\partial u}{\partial x}\right)_{i+\frac{1}{2},j} - \left(\frac{\partial u}{\partial x}\right)_{i-\frac{1}{2},j} \right] h,$$
$$\oint_{\partial\Omega_{ij}} \frac{\partial u}{\partial x} n_y ds = \left[\left(\frac{\partial u}{\partial x}\right)_{i,j+\frac{1}{2}} - \left(\frac{\partial u}{\partial x}\right)_{i,j-\frac{1}{2}} \right] h, \tag{3.48a}$$
$$\oint_{\partial\Omega_{ij}} \frac{\partial u}{\partial y} n_y ds = \left[\left(\frac{\partial u}{\partial y}\right)_{i,j+\frac{1}{2}} - \left(\frac{\partial u}{\partial y}\right)_{i,j-\frac{1}{2}} \right] h,$$

with

$$\left(\frac{\partial u}{\partial x}\right)_{i+\frac{1}{2},j} = \frac{1}{h^2} \oint_{\partial\Omega_{i+\frac{1}{2},j}} un_x ds = \frac{1}{h}(u_{i+1,j} - u_{ij}),$$
$$\left(\frac{\partial u}{\partial x}\right)_{i,j+\frac{1}{2}} = \frac{1}{h^2} \oint_{\partial\Omega_{ij+\frac{1}{2}}} un_x ds = \frac{1}{h}\left[\frac{1}{4}(u_{ij} + u_{i+1,j} + u_{ij+1} + u_{i+1,j+1}) - \right. \tag{3.48b}$$
$$\left. \frac{1}{4}(u_{i-1,j} + u_{ij} + u_{i-1,j+1} + u_{ij+1})\right] =$$
$$= \frac{1}{4h}(u_{i+1,j} + u_{i+1,j+1} - u_{i-1,j} - u_{i-1,j+1}),$$
$$\left(\frac{\partial u}{\partial y}\right)_{i,j+\frac{1}{2}} = \frac{1}{h^2} \oint_{\partial\Omega_{ij+\frac{1}{2}}} un_y ds = \frac{1}{h}(u_{ij+1} - u_{ij}),$$

and similar expressions for $\left(\frac{\partial u}{\partial x}\right)_{i-\frac{1}{2},j}$, $\left(\frac{\partial u}{\partial x}\right)_{ij-\frac{1}{2}}$ and $\left(\frac{\partial u}{\partial y}\right)_{ij-\frac{1}{2}}$. In (3.48b), $\partial\Omega_{i+\frac{1}{2},j}$ and $\partial\Omega_{ij+\frac{1}{2}}$ denote the boundary of shifted volume $\Omega_{i+\frac{1}{2},j}$ and $\Omega_{ij+\frac{1}{2}}$, respectively (Fig. 3.7).

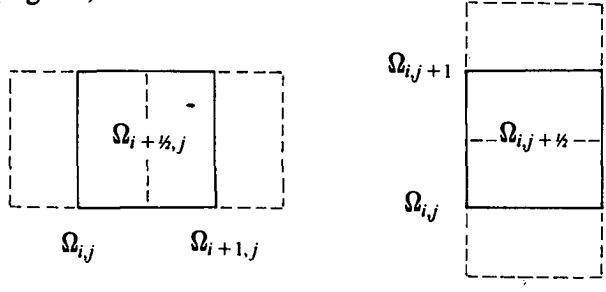

a. $\Omega_{i+\frac{1}{2},j}$. b. $\Omega_{ij+\frac{1}{2}}$.

Fig. 3.7. Shifted finite volumes.

With the previous flux evaluations we get for (3.46) the algebraic equation:

$$\frac{1}{4}\frac{\epsilon}{h}u_{i-1,j+1}+(\alpha_3-\frac{\epsilon}{h})u_{i,j+1}-\frac{1}{4}\frac{\epsilon}{h}u_{i+1,j+1}-$$

$$\alpha_1 u_{i-2,j}+(\alpha_1-\alpha_2-\frac{\epsilon}{h})u_{i-1,j}+(2\alpha_2-2\alpha_3+4\frac{\epsilon}{h})u_{i,j}+(\alpha_3-\frac{\epsilon}{h})u_{i+1,j}-$$

$$\frac{1}{4}\frac{\epsilon}{h}u_{i-1,j-1}+(\alpha_1-\alpha_2-\frac{\epsilon}{h})u_{i,j-1}+\frac{1}{4}\frac{\epsilon}{h}u_{i+1,j-1}-$$

$$\alpha_1 u_{i,j-2}=0, \tag{3.49}$$

with the corresponding stencil:

	$i-2$	$i-1$	i	$i+1$
$j+1$		$\frac{1}{4}\frac{\epsilon}{h}$	$\alpha_3-\frac{\epsilon}{h}$	$-\frac{1}{4}\frac{\epsilon}{h}$
j	$-\alpha_1$	$\alpha_1-\alpha_2-\frac{\epsilon}{h}$	$2\alpha_2-2\alpha_3+4\frac{\epsilon}{h}$	$\alpha_3-\frac{\epsilon}{h}$
$j-1$		$-\frac{1}{4}\frac{\epsilon}{h}$	$\alpha_1-\alpha_2-\frac{\epsilon}{h}$	$\frac{1}{4}\frac{\epsilon}{h}$
$j-2$			$-\alpha_1$	

(3.50)

For point Gauss-Seidel relaxation applied to (3.49), as mentioned, the four extreme sweep directions are considered (downwind, upwind and twice crosswind). Introducing n for the number of sweeps performed, these four possibilities can be illustrated as has been done in Fig. 3.8.

	$i-1$	i	$i+1$
$j+1$	u^n	u^n	u^n
j	$\mathbf{u^{n+1}}$	$\mathbf{u^{n+1}}$	u^n
$j-1$	$\mathbf{u^{n+1}}$	$\mathbf{u^{n+1}}$	$\mathbf{u^{n+1}}$

a. Downwind.

	$i-1$	i	$i+1$
$j+1$	$\mathbf{u^{n+1}}$	$\mathbf{u^{n+1}}$	$\mathbf{u^{n+1}}$
j	u^n	$\mathbf{u^{n+1}}$	$\mathbf{u^{n+1}}$
$j-1$	u^n	u^n	u^n

b. Upwind.

	$i-1$	i	$i+1$
$j+1$	u^n	u^n	u^n
j	u^n	$\mathbf{u^{n+1}}$	$\mathbf{u^{n+1}}$
$j-1$	$\mathbf{u^{n+1}}$	$\mathbf{u^{n+1}}$	$\mathbf{u^{n+1}}$

c. Crosswind.

	$i-1$	i	$i+1$
$j+1$	$\mathbf{u^{n+1}}$	$\mathbf{u^{n+1}}$	$\mathbf{u^{n+1}}$
j	$\mathbf{u^{n+1}}$	$\mathbf{u^{n+1}}$	u^n
$j-1$	u^n	u^n	u^n

d. Crosswind.

Fig. 3.8. Basic sweep directions, convection direction:

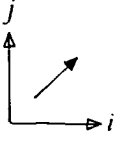

To apply Fourier analysis, we introduce: (i) the iteration error

$$\delta_{i,j}^{n} \equiv u_{i,j}^{*} - u_{i,j}^{n}, \tag{3.51}$$

with $u_{i,j}^{*}$ the converged numerical solution in $\Omega_{i,j}$, and (ii) the Fourier form

$$\delta_{i,j}^{n} = D\mu^{n} e^{\mathrm{i}(\omega_1 i + \omega_2 j)h}, \tag{3.52}$$

with D constant, μ the amplification factor, and ω_1 and ω_2 the error mode in i- and j-direction, respectively. The modes to be considered are: $(|\theta_1|,|\theta_2|) \in \{[0,\pi]\times[0,\pi] \,|\, |\theta_1| \in [\pi/2,\pi] \vee |\theta_2| \in [\pi/2,\pi]\}$, with $\theta_1 \equiv \omega_1 h$, $\theta_2 \equiv \omega_2 h$. Results of the smoothing analysis are given now for successively the first- and second-order discretized model equation (3.49).

First-order discretization. For the first-order accurate model discretization we have $\alpha_1 = \alpha_3 = 0, \alpha_2 = 1$. With this the general 11-point stencil (3.50) reduces to the following 9-point stencil

	$i-1$	i	$i+1$
$j+1$	$\frac{1}{4}\frac{\epsilon}{h}$	$-\frac{\epsilon}{h}$	$-\frac{1}{4}\frac{\epsilon}{h}$
j	$-(1+\frac{\epsilon}{h})$	$2+4\frac{\epsilon}{h}$	$-\frac{\epsilon}{h}$
$j-1$	$-\frac{1}{4}\frac{\epsilon}{h}$	$-(1+\frac{\epsilon}{h})$	$\frac{1}{4}\frac{\epsilon}{h}$

(3.53)

Using the iteration error (3.52) we obtain the smoothing results given in Fig. 3.9. In Fig. 3.9a, for each of the four possible sweep directions, the smoothing factor $\mu_s = \sup|\mu(\theta_1, \theta_2)|$ is given as a function of ϵ/h. In Fig. 3.9b, for $\epsilon/h = 1$, the corresponding distributions $|\mu(\theta_1,\theta_2)|$ are given. (All four distributions are point-symmetric with respect to $\theta_1 = 0, \theta_2 = 0$.) Clearly visible in Fig. 3.9a is the good smoothing for any value of ϵ/h and any convection direction, when sweeping alternatingly in all four different directions (for instance by applying symmetric sweeps and by using a different diagonal sweep direction in pre- and post-relaxation).

Second-order discretization. For the second-order accurate model discretization we have: $\alpha_1 = -1/6, \alpha_2 = 5/6, \alpha_3 = 1/3$. With these values, (3.50) becomes

	$i-2$	$i-1$	i	$i+1$
$j+1$		$\frac{1}{4}\frac{\epsilon}{h}$	$\frac{1}{3}-\frac{\epsilon}{h}$	$-\frac{1}{4}\frac{\epsilon}{h}$
j	$\frac{1}{6}$	$-(1+\frac{\epsilon}{h})$	$1+4\frac{\epsilon}{h}$	$\frac{1}{3}-\frac{\epsilon}{h}$
$j-1$		$-\frac{1}{4}\frac{\epsilon}{h}$	$-(1+\frac{\epsilon}{h})$	$\frac{1}{4}\frac{\epsilon}{h}$
$j-2$			$\frac{1}{6}$	

(3.54)

For the four extreme sweep directions, this yields the smoothing results given in Fig. 3.10. Only for $\epsilon/h > 1$ there appears to be some acceptable smoothing.

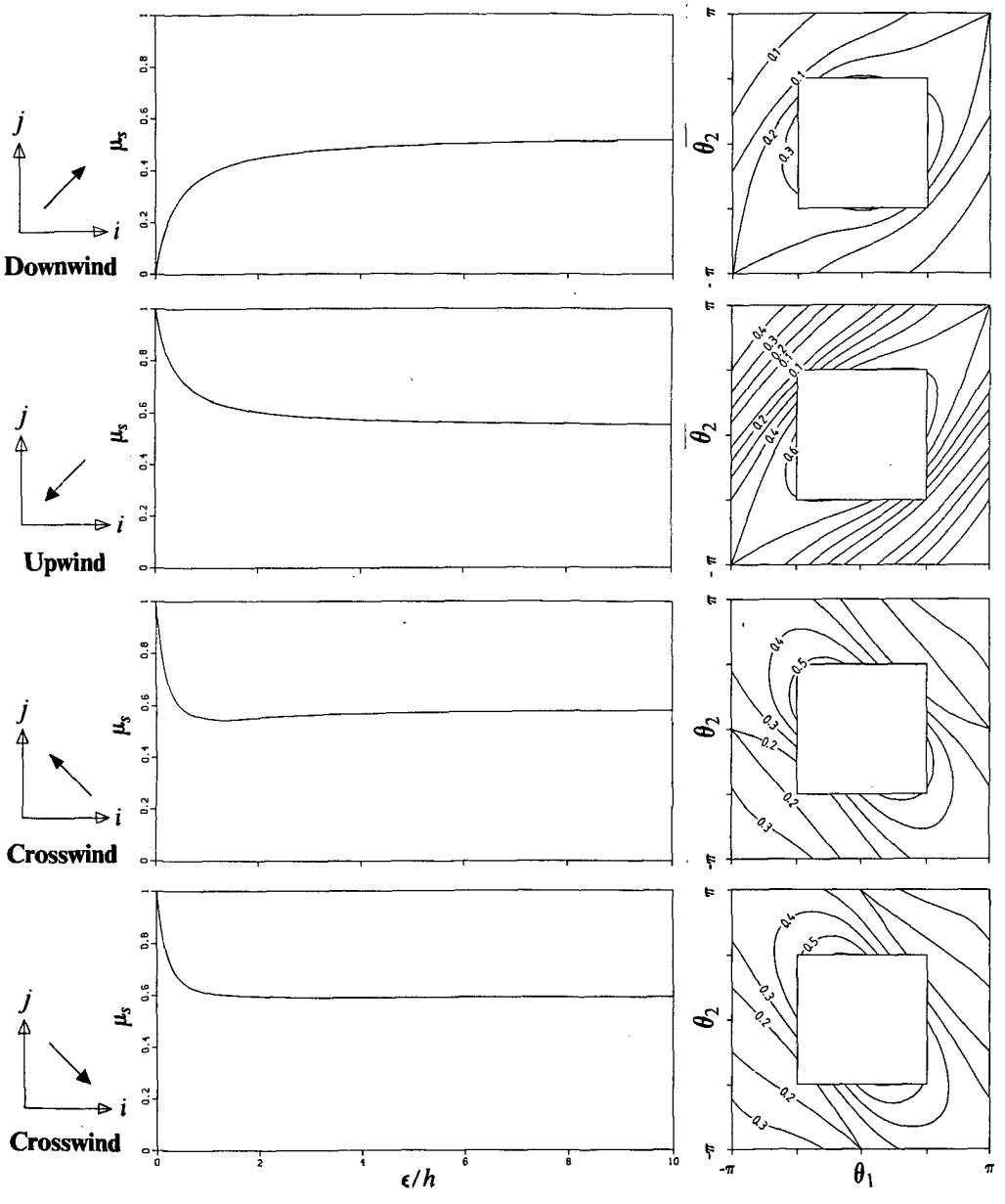

a. Versus ϵ/h.

b. For $\epsilon/h = 1$.

Fig. 3.9. Smoothing factors point Gauss-Seidel relaxation, first-order discretized model equation.

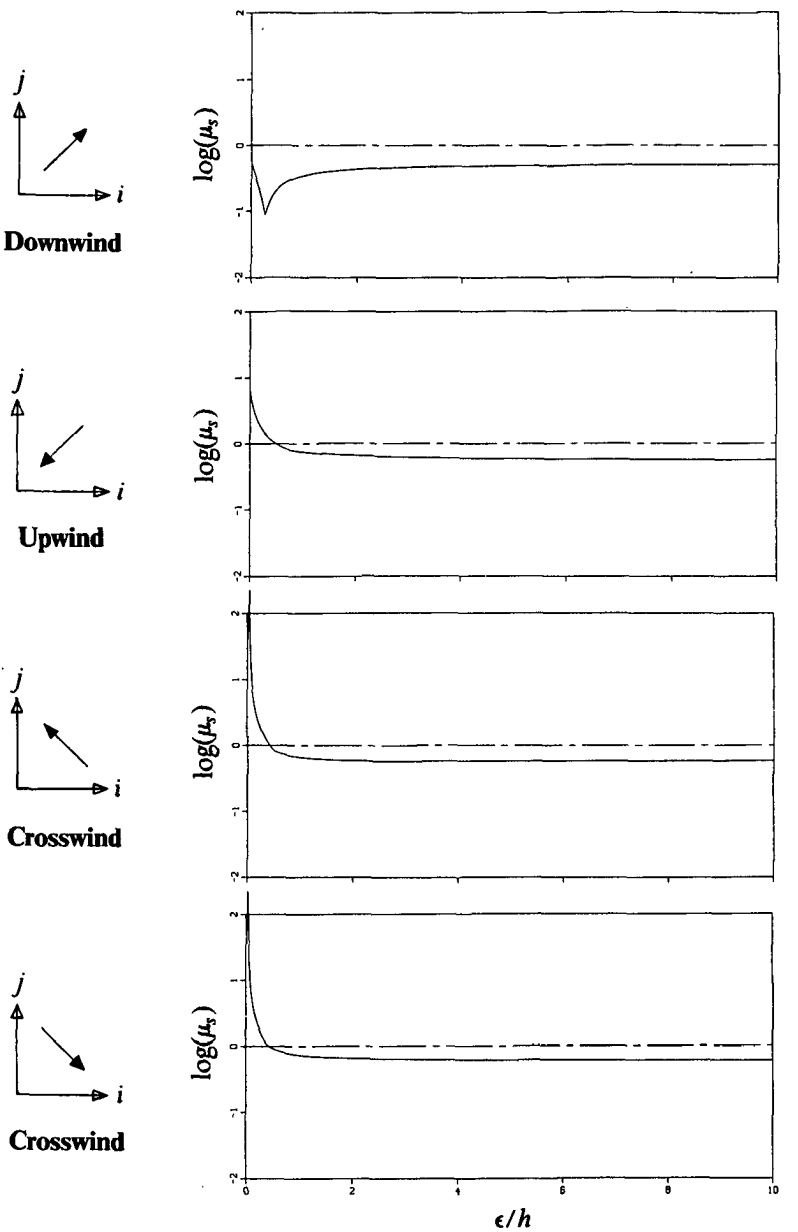

Fig. 3.10. Smoothing factors point Gauss-Seidel relaxation, second-order discretized model equation.

3.3.3. Defect correction

For flow problems which are convection dominated, the smoothing factors presented in Fig. 3.10 are unacceptable, except perhaps for those belonging to the purely downwind sweep. Since purely downwind relaxation sweeps are not feasible in practice, and since no specific alternation of sweep directions is supposed to suffice, as already expected, a remedy for the good smoothing lost has to be found.

Analogous to the Euler equations, we will solve the system of higher-order discretized equations as they stand, by iterative defect correction

$$N_L(q_L^{n+1}) = N_L(q_L^n) - N_L^+(q_L^n), \quad n = 0,1,...,N, \tag{3.55}$$

with N_L^+ the higher-order Navier-Stokes operator (at Ω_L) and N_L the operator to be inverted. A requirement to be fulfilled by N_L, as just seen, is that it must have a first-order accurate convective part. The choice of the diffusive part, however, is taken free. Two extreme possibilities are available already: (i) the operator without diffusive terms as applied in chapter 2 for the Euler equations, and (ii) the operator with second-order accurate diffusion as just studied for model equation (3.22). The advantage of the first approximate operator is its greater simplicity. The advantage of the second operator is its closer resemblance to the target operator N_L^+, and hence its expected better convergence properties. It complies with the theory that for sufficiently smooth problems, the solution will be second-order accurate after a single IDeC-cycle only [3]. (Notice that for the second approximate operator, the greater complexity in the left-hand side of (3.55) is counteracted a little bit by a greater simplicity in the right-hand side, due to cancellation of the diffusive terms in $N_L(q_L^n)$ and $N_L^+(q_L^n)$.) Both possibilities will be analyzed. As an intermediate alternative we also analyze the approximate operator which neglects mixed derivatives. This operator combines, in some intermediate way, simplicity and good resemblance. For the analysis we consider again the scalar, linear convection diffusion equation (3.22). The analysis is done for both the outer and inner iteration; convergence and smoothing analysis, respectively.

Convergence analysis. Concisely written, the three approximate operators to be considered are: (i) the first-order accurate convection operator

$$\begin{array}{cc|c|c|} & & -1 & 2 \\ j & & & -1 \\ j-1 & & & \end{array} \qquad \begin{array}{c} \\ \\ \\ \end{array} \tag{3.56}$$

$$\qquad\qquad i-1 \qquad i$$

(ii) the zeroth-order accurate convection-diffusion operator

$$\begin{array}{ccc|c|c|} & & & -\frac{\epsilon}{h} & \\ j+1 & & & & \\ j & & -(1+\frac{\epsilon}{h}) & 2+4\frac{\epsilon}{h} & -\frac{\epsilon}{h} \\ j-1 & & & -(1+\frac{\epsilon}{h}) & \\ & & & & \end{array} \tag{3.57}$$

$$\qquad\qquad\qquad i-1 \qquad\qquad i \qquad\qquad i+1$$

and, (iii) the first-order accurate convection-diffusion operator (3.53).

For the model equation (3.22), iteration (3.55) is rewritten as

$$L_L(u_L^{n+1}) = (L_L - L_L^+)(u_L^n), \quad n=0,1,...,N, \tag{3.58}$$

L_L^+ and L_L denoting the finest-grid target and approximate operator, respectively. Introducing as before the iteration error (3.51) in its Fourier form (3.52), we can write for the convergence factor μ:

$$\mu(\theta_1,\theta_2) = 1 - L_L^{-1}(\theta_1,\theta_2)L_L^+(\theta_1,\theta_2). \tag{3.59}$$

Convergence results are given in Fig. 3.11 and 3.12. In Fig. 3.11, for each of the three approximate operators (3.56), (3.57) and (3.53), the convergence factor $\mu_c = \sup|\mu(\theta_1,\theta_2)|$ with $(|\theta_1|,|\theta_2|) \in \{[0,\pi]\times[0,\pi]\}$, is given as a function of ϵ/h. In Fig. 3.12, for $\epsilon/h = 4/9$, $\epsilon/h = 1$ and $\epsilon/h = \infty$, the corresponding distributions of $|\mu(\theta_1,\theta_2)|$ are given. From Fig. 3.11 it appears that for small values of ϵ/h, the approximate operator (3.56) yields the best convergence rate. However, as was to be expected, for increasing ϵ/h its convergence starts to deteriorate (from $\epsilon/h = 4/9$) and finally turns into divergence (at $\epsilon/h = 2/3$). Even for high-Reynolds number flows, local regions with diffusion dominating convection may arise. Therefore, approximate operator (3.56) has to be rejected. As far as the convergence rate of the two remaining operators is concerned, the 9-point operator (3.53) clearly is to be preferred above the 5-point alternative (3.57).

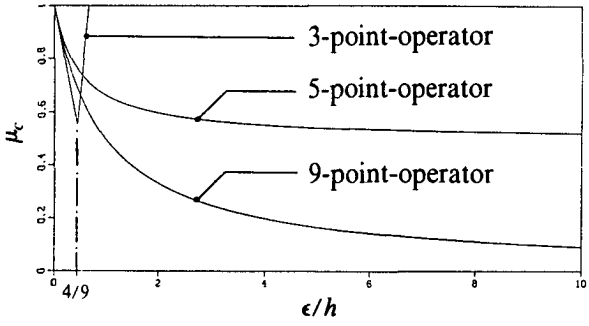

Fig. 3.11. Convergence factors iterative defect correction, second-order discretized model equation.

Smoothing analysis. However, the 5-pointer might behave better in the inner iteration (point Gauss-Seidel accelerated by multigrid). In Fig. 3.13, for the four extreme sweep directions, its smoothing factors μ_s are given as a function of ϵ/h. For comparison, the smoothing factors for the 9-point operator (Fig. 3.9) have been added. It appears that both operators nearly have the same good smoothing behaviour, the 5-pointer being only slightly better. Because of its superior behaviour in IDeC (Fig. 3.11), we prefer the 9-pointer as operator to be inverted. (Its relative complexity is taken for granted.)

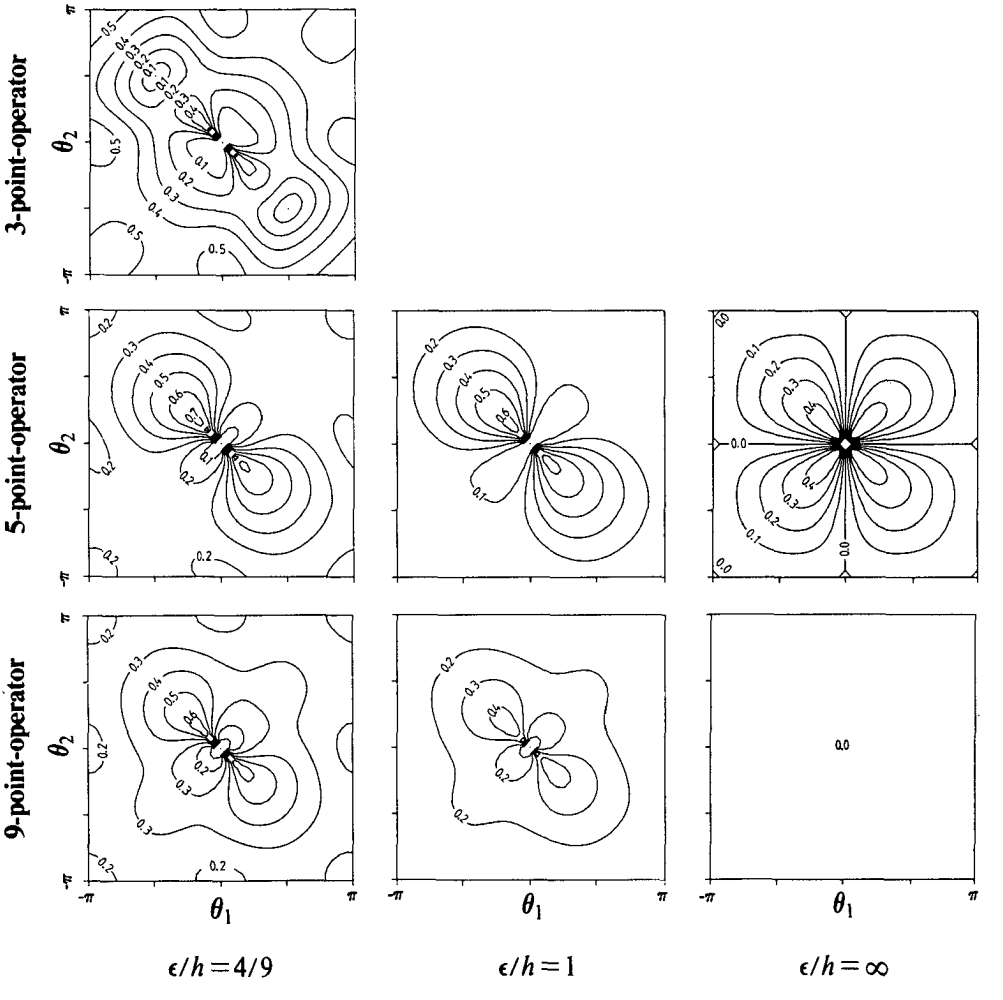

Fig. 3.12. Convergence factors iterative defect correction, second-order discretized model equation.

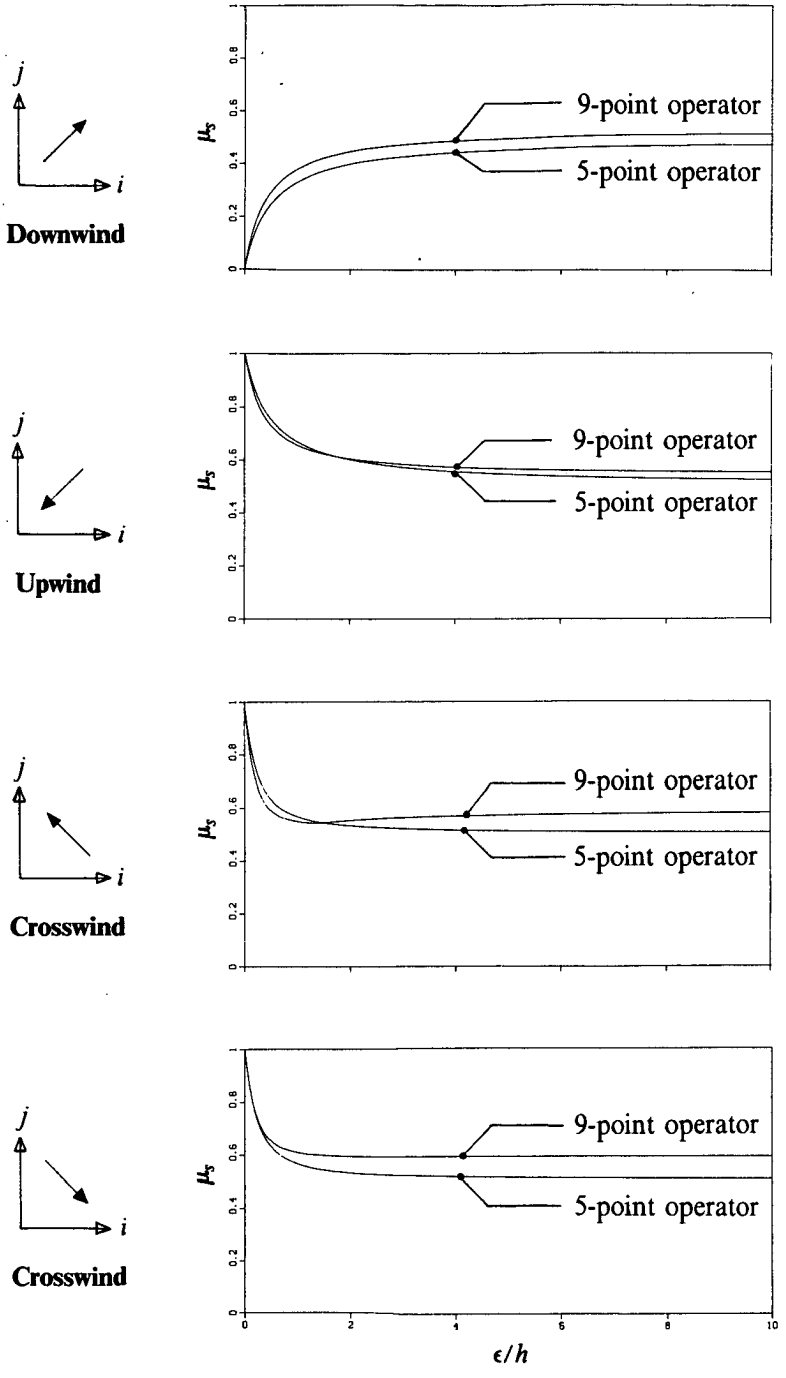

Fig. 3.13. Smoothing factors point Gauss-Seidel relaxation, zeroth- and first-order discretized model equation.

3.4. Concluding remarks

Model analysis indicates that, already for a rather low Reynolds number, Osher's scheme probably leads to a more accurate resolution of boundary layer flows than Van Leer's scheme. The difference in accuracy seems to become larger with increasing Reynolds number.

The second-order truncation error due to the central discretization of the diffusive part may be cancelled by an appropriate, diffusion-dependent, higher-order discretization of the convective part, leading to a third-order truncation error for the full Navier-Stokes operator. For high-Reynolds number flows, our interest, this diffusion-dependent discretization resembles the much simpler $\kappa = \frac{1}{3}$-scheme, which scheme allows a likewise simple construction of a consistent limiter.

For hypersonic flow computations, Osher's boundary condition treatment at solid impermeable walls can be simply protected against an extrapolation beyond vacuum by switching to a boundary condition treatment which applies the safe mirror principle.

Formulating the Navier-Stokes fluxes as functions of $(u,v,c,z)^T$ is not only convenient for the Osher convective fluxes, but also for the central diffusive fluxes.

An efficacious remedy against possible failure of the local Newton iteration is expected to be obtained by a switch to local explicit time stepping. Appropriate monitors of the Newton iteration are supposed to be the error behaviour and the physical relevance of the iterates.

Smoothing analysis indicates that for the higher-order ($\kappa = \frac{1}{3}$) discretized Navier-Stokes equations, point Gauss-Seidel relaxation is only effective if applied in streamwise direction, which is inconvenient for practical purposes.

Analysis suggests that iterative defect correction as the solution method for the higher-order discretized Navier-Stokes equations works well if applied with the first-order Navier-Stokes operator as approximate operator.

In the next chapter we will consider a few discriminating test cases for the present Navier-Stokes method.

References

1. S.R. Chakravarthy, K.-Y. Szema, U.C. Goldberg, J.J. Gorski and S. Osher, *Application of a New Class of High Accuracy TVD Schemes to the Navier-Stokes Equations,* AIAA paper 85-0165 (1985).
2. S.K. Godunov, *Finite Difference Method for Numerical Computation of Discontinuous Solutions of the Equations of Fluid Dynamics,* (Cornell Aeronautical Lab. Transl. from the Russian) Math. Sbornik 47, 271-306 (1959).
3. W. Hackbusch, *Multi-Grid Methods and Applications* (Springer, Berlin, 1985).
4. D. Hänel and R. Schwane, *An Implicit Flux-Vector Splitting Scheme for the Computation of Viscous Hypersonic Flow,* AIAA paper 89-0274 (1989).

5. P.W. HEMKER AND B. KOREN, *Defect Correction and Nonlinear Multigrid for the Steady Euler Equations,* in Lecture Series Computational Fluid Dynamics (Von Karman Institute for Fluid Dynamics, Rhode-Saint-Genèse, 1988).
6. P.W. HEMKER AND B. KOREN, *Multigrid, Defect Correction and Upwind Schemes for the Steady Navier-Stokes Equations,* in Numerical Methods for Fluid Dynamics III, Proceedings of the Third Conference on Numerical Methods for Fluid Dynamics, Oxford, 1988, 153-170, edited by K.W. Morton and M.J. Baines (Clarendon Press, Oxford, 1988).
7. P.W. HEMKER AND S.P. SPEKREIJSE, *Multiple Grid and Osher's Scheme for the Efficient Solution of the Steady Euler Equations,* Appl. Numer. Math. 2, 475-493 (1986).
8. B. KOREN, *Upwind Schemes for the Navier-Stokes Equations,* in Nonlinear Hyperbolic Equations - Theory, Numerical Methods and Applications, Proceedings of the Second International Conference on Hyperbolic Problems, Aachen, 1988, Notes on Numerical Fluid Mechanics Vol. 24, 300-309, edited by J. Ballmann and R. Jeltsch (Vieweg, Braunschweig, 1989).
9. B. KOREN, *Multigrid and Defect Correction for the Steady Navier-Stokes Equations,* J. Comput. Phys. (accepted for publication).
10. B. KOREN, *Upwind Schemes, Multigrid and Defect Correction for the Steady Navier-Stokes Equations,* in Proceedings of the 11th International Conference on Numerical Methods in Fluid Dynamics, Williamsburg, 1988, Lecture Notes in Physics Vol. xx, edited by D.L. Dwoyer and R.G. Voigt (Springer, Berlin, to appear).
11. B. KOREN, *Robustness Improvement of Point Gauss-Seidel Relaxation for Steady, Hypersonic Flow Computations,* Centre for Mathematics and Computer Science, Amsterdam, Note NM-N8805 (unpublished, 1988).
12. B. VAN LEER, *Flux-Vector Splitting for the Euler Equations,* in Proceedings of the Eighth International Conference on Numerical Methods in Fluid Dynamics, Aachen, 1982, Lecture Notes in Physics Vol. 170, 507-512, edited by E. Krause (Springer, Berlin, 1982).
13. B. VAN LEER, J.L. THOMAS, P.L. ROE AND R.W. NEWSOME, *A Comparison of Numerical Flux Formulas for the Euler and Navier-Stokes Equations,* AIAA paper 87-1104 (1987).
14. S. OSHER AND S.R. CHAKRAVARTHY, *Upwind Schemes and Boundary Conditions with Applications to Euler Equations in General Geometries,* J. Comput. Phys. 50, 447-481 (1983).
15. S. OSHER AND F. SOLOMON, *Upwind Difference Schemes for Hyperbolic Systems of Conservation Laws,* Math. Comput. 38, 339-374 (1982).
16. W. SCHRÖDER AND D. HÄNEL, *An Unfactored Implicit Scheme with Multigrid Acceleration for the Solution of the Navier-Stokes Equations,* Comput. and Fluids 15, 313-336 (1987).
17. G. SHAW AND P. WESSELING, *Multigrid Solution of the Compressible Navier-Stokes Equations on a Vector Computer,* in Proceedings of the 10th International Conference on Numerical Methods in Fluid Dynamics, Beijing, 1986, Lecture Notes in Physics Vol. 264, 566-571, edited by F.G. Zhuang and Y.L. Zhu (Springer, Berlin, 1986).

18. S.P. SPEKREIJSE, *Multigrid Solution of Monotone Second-Order Discretizations of Hyperbolic Conservation Laws,* Math. Comput. 49, 135-155 (1987).
19. P.K. SWEBY, *High Resolution Schemes using Flux Limiters for Hyperbolic Conservation Laws,* SIAM J. Numer. Anal. 21, 995-1011 (1984).
20. J.L. THOMAS AND R.W. WALTERS, *Upwind Relaxation Algorithms for the Navier-Stokes Equations,* AIAA paper 85-1501 (1985).
21. A. WAMBECQ, *Rational Runge-Kutta Methods for Solving Systems of Ordinary Differential Equations,* Computing 20, 333-342 (1978).

Chapter 4

Numerical Results for the Steady Navier-Stokes Equations

4.1. Introductory remarks

In this chapter we examine the practical interest of the Navier-Stokes method presented in the previous chapter. For this we consider successively a subsonic and supersonic flat plate flow in the Mach number range of our main interest (section 1.4.1), as well as a hypersonic blunt body flow. Going from the subsonic to the hypersonic case, the variety of flow features increases and also the difficulty in solving the problem. Moreover, the possibility to make comparisons with reference results decreases. For the simplest test case among the three, the subsonic flat plate flow, the Blasius solution [2] is used as a reliable reference solution. The supersonic flat plate flow to be considered is the well-known experiment for oblique shock wave - boundary layer interaction performed by Hakkinen et al. [5]. For this test case, the experimental results themselves will serve as a reference. For the hypersonic blunt body flow, a new standard test case in hypersonics, reliable reference solutions do not yet exist. For this problem, our main interest is merely to investigate the robustness of the solution method. In all three cases the perfect gas considered is di-atomic; $\gamma=1.4$. For the Prandtl number we take the value for laminar air flow; $Pr=0.71$. The results to be presented have appeared (or will soon appear) in [7,8,9,10,11,12].

4.2. Subsonic flat plate flow

4.2.1. Purpose

Because of the availability of the Blasius solution as an exact reference solution for incompressible half-infinite-flat-plate flows, and because of their simplicity, subsonic finite-flat-plate-flows at sufficiently low Mach numbers and sufficiently high Reynolds numbers are well-suited for a first evaluation of compressible Navier-Stokes methods. We will investigate the first- and second-order discretization as well as the convergence to the corresponding solutions.

Geometry and boundary conditions as chosen for this flow problem are given in Fig. 4.1. As far as convection is concerned, the eastern boundary is assumed to be an outflow boundary. For diffusion, the northern, southern and eastern boundary are assumed to be far-field boundaries with zero diffusion. The grids applied are composed of square finite volumes. As coarsest grid Ω_1, in all multigrid computations we use the 4×2-grid given in Fig. 4.1.

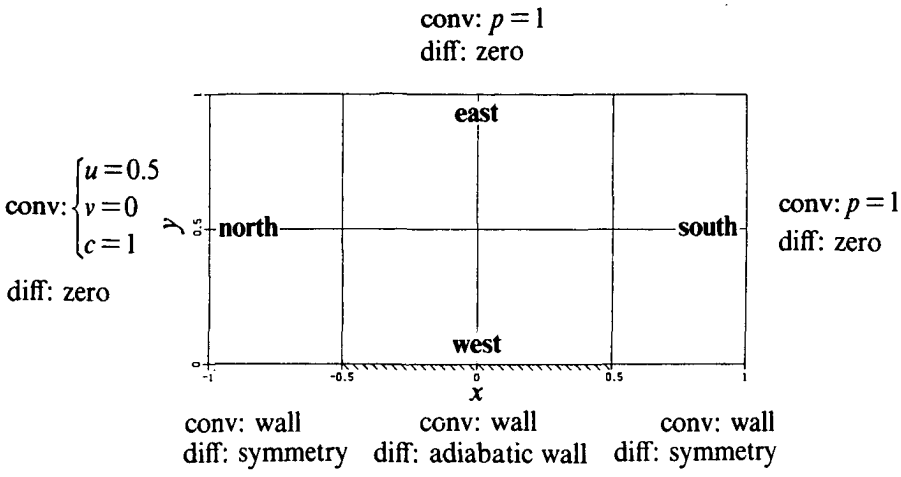

Fig. 4.1. Geometry, boundary conditions and coarsest grid (Ω_1) subsonic flat plate flow (conv: convection, diff: diffusion).

4.2.2. First-order accurate results

Osher versus Van Leer. To show at first the benefit of the careful solid wall - boundary condition treatment as proposed for Van Leer's scheme in section 3.2.2, we consider the subsonic flat plate flow at $Re=10^{100}$. For both Osher's and Van Leer's scheme we compute the flow on a 64×32-grid (Ω_5, Fig. 4.2), using the first-order accurate discretization and imposing on the convective part, successively: (i) non-permeability, no-slip and no-heat-transfer, and - carefully - (ii) non-permeability only. As the numerical results, we show converged velocity profiles obtained at the middle of the plate ($x=0$). For the case with all Navier-Stokes boundary conditions imposed, it appears that Van Leer's scheme severely thickens the thin layer, whereas Osher's scheme preserves it (Fig. 4.3a). With the careful approach, both schemes preserve the layer (Fig. 4.3b).

Using the careful boundary condition treatment, for both schemes we perform next an experiment with *h*- and *Re*-variation, using again the first-order accurate discretization. Numerical results obtained - again velocity profiles at $x=0$ - are given in Fig. 4.4. The results show the superiority of Osher's scheme, in particular for high mesh Reynolds numbers. The deterioration of Van Leer's scheme with respect to Osher's scheme which occurs in Fig. 4.4b for increasing *Re*, is in qualitative agreement with the theoretical results presented in section 3.2.2.

All further numerical results will be obtained with Osher's scheme only.

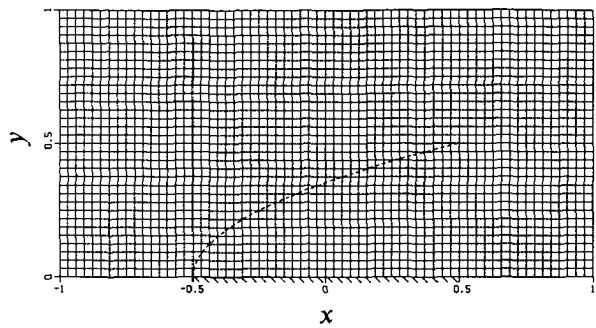

Fig. 4.2. 64×32-grid (Ω_5) subsonic flat plate flow
(------ : boundary layer edge Blasius solution at $Re = 100$).

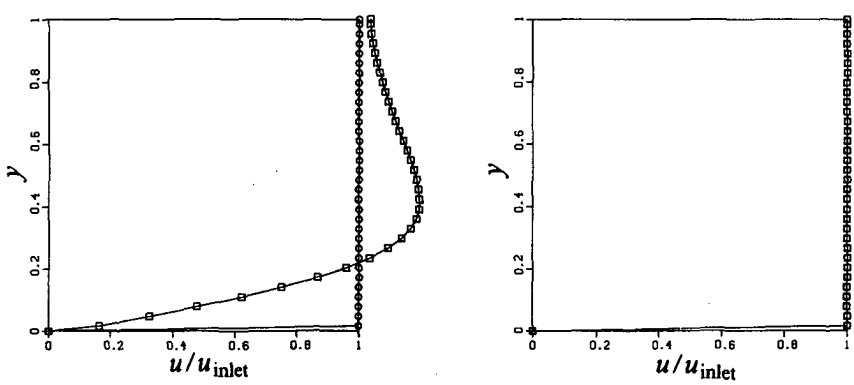

a. $u = v = 0, \quad \dfrac{\partial c}{\partial y} = 0.$ b. $v = 0$ only.

Fig. 4.3. Velocity profiles at $x = 0$ for the subsonic flat plate flow at $Re = 10^{100}$ and $h = 1/32$, for two solid wall boundary condition treatments
(○ : Osher, □ : Van Leer).

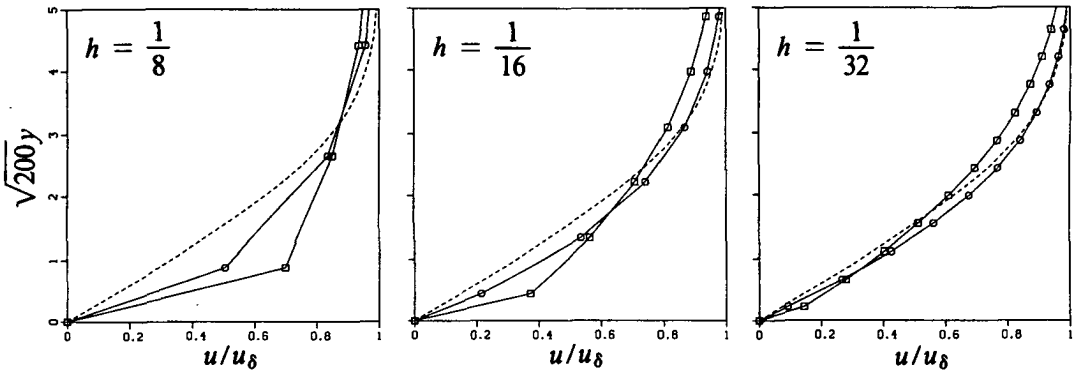

a. h-variation at $Re = 100$, $h = 1/8, 1/16, 1/32$
(○ : Osher, □ : Van Leer).

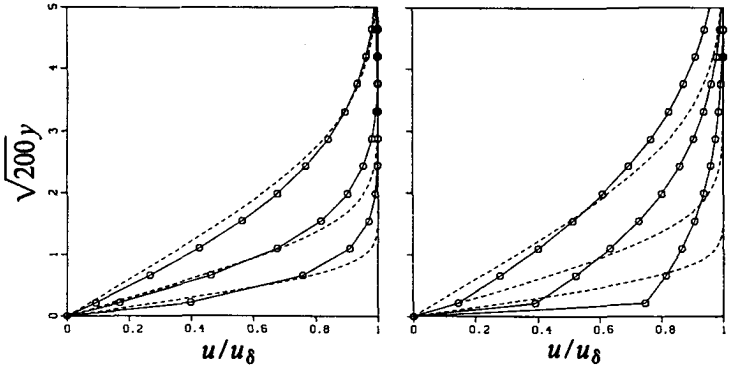

b. Re-variation at $h = 1/32$, $Re = 100, 400, 1600$
(left: Osher, right: Van Leer).

Fig. 4.4. Velocity profiles at $x = 0$ for the subsonic flat plate flow
(------ : Blasius solution).

Multigrid behaviour. To investigate the convergence properties of the nonlinear multigrid technique for the subsonic flat plate flow, we consider it at $Re = 100$. The convergence results obtained are given in Fig. 4.5 by a graph of the residual ratios $\Sigma_{k=1}^{4}|(N_L(q_L^n))_k| / \Sigma_{k=1}^{4}|(N_L(q_L^0))_k|$, $L = 3,4,5$ versus the number of cycles performed, one multigrid cycle being again a V-cycle with $p = q = 1$, $\forall l$, and - for Ω_5 only - one single-grid cycle being the equivalent number of finest-grid relaxation sweeps. $|(N_L(q_L^n))_k|$ denotes the summation - over all volumes at Ω_L - of the absolute values of the k-th component in the first-order Navier-Stokes defects, with q_L^n denoting again the n-th iterate at Ω_L and q_L^0 the approximate solution obtained by the nested iteration. For the present flow problem the method appears to be nearly grid-independent. Considering the single-grid convergence history, the effectiveness of the multigrid method is clear. In the same figure, the influence of the higher-order accuracy of the correction prolongation is illustrated by giving also the convergence history for a strategy with $m_p = 1$, so violating multigrid rule (3.45). Already for this moderately convection dominated flow ($Re = 100$), the positive influence of the second-order prolongation appears to be negligible. In [14], for another convection diffusion equation, Wesseling finds a similar result.

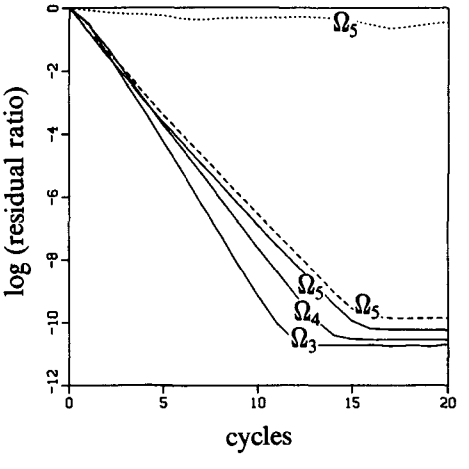

Fig. 4.5. Multigrid behaviour for the subsonic flat plate flow at $Re = 100$
(····· : single-grid, —— : multigrid $m_p = 2$, ------ : multigrid $m_p = 1$).

Theory predicts that a single FAS-cycle may be sufficient for obtaining first-order accuracy [6]. To investigate the present multigrid method's performance with respect to this prediction we loosely compare first-order solutions obtained for $Re = 100$ at Ω_3, Ω_4 and Ω_5. In Fig. 4.6 we give velocity profiles at the middle of the plate, as obtained after one FAS-cycle. Assuming the Blasius solution to be the exact solution, it can be verified that the results obtained (more or less) satisfy the prediction. Furthermore, for all three grids the fully converged velocity profile (that obtained after 20 FAS-cycles) is also given. Just like with the Euler results shown in Fig. 2.16 - also here - it appears that only one FAS-cycle is sufficient for converging to first-order truncation error accuracy. For Ω_5 (Fig. 4.6c), the velocity profiles as obtained after 1 and 20 FAS-cycles cannot even be distinguished. Additionally, for comparison, in Fig. 4.6c the single-grid profile as obtained after one, two, three and four symmetric relaxation sweeps is also given. This clearly shows once more the effectiveness of the multigrid technique.

In none of these first-order accurate computations the switched-relaxation-evolution approach needed to be invoked. Pure relaxation worked in all cases.

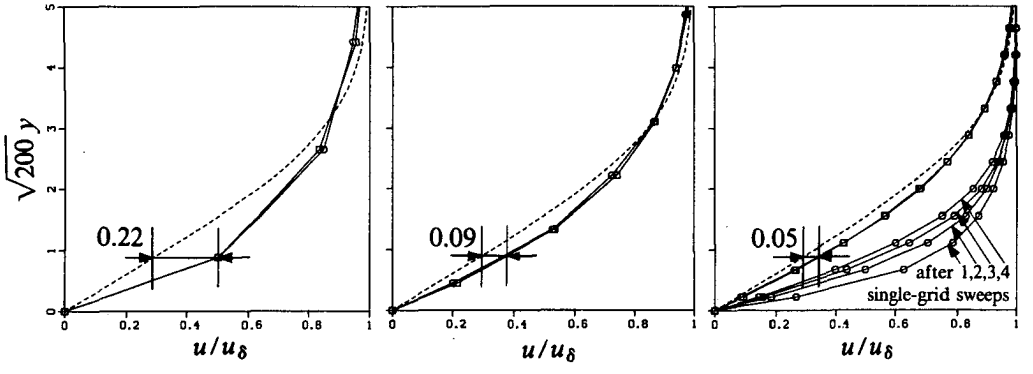

a. On Ω_3. b. On Ω_4. c. On Ω_5.

Fig. 4.6. Velocity profiles at $x = 0$ for the subsonic flat plate flow at $Re = 100$, first-order discretized Navier-Stokes equations
(------ : Blasius solution, ○ : after 1 FAS-cycle, □ : after 20 FAS-cycles).

4.2.3. Second-order accurate results

As mentioned before, for sufficiently smooth problems, theory also predicts that a single IDeC-cycle will be sufficient for obtaining second-order accuracy [4]. To investigate the convergence properties with respect to this prediction, we investigate now second-order accurate solutions obtained on Ω_3,Ω_4 and Ω_5. In Fig. 4.7 we give velocity profiles at the middle of the plate as obtained after one IDeC-cycle. Assuming again the Blasius solution to be the exact solution, it can be verified that the results satisfy the prediction pretty well. Just as with the first-order discretization, the fully converged profiles (those obtained after 50 IDeC-cycles) are also given. They can hardly be distinguished from those obtained after one IDeC-cycle, indicating the likewise fast convergence of IDeC.

Also here, for none of the computations, the switched-relaxation-evolution approach needed to be invoked.

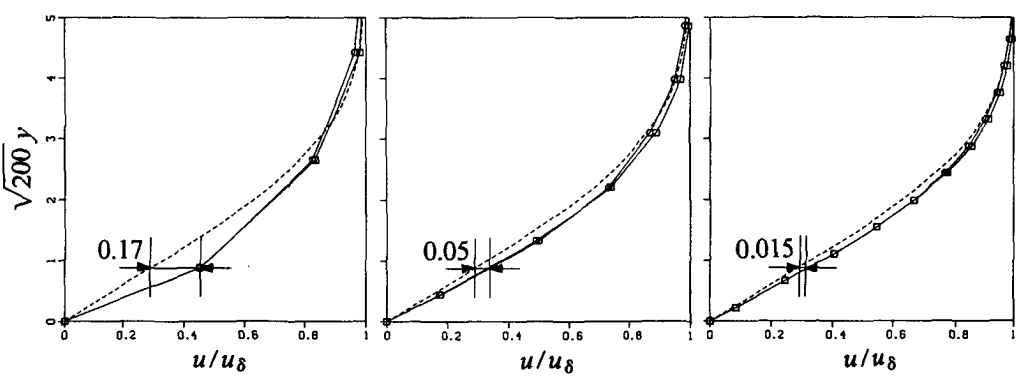

a. On Ω_3. b. On Ω_4. c. On Ω_5.

Fig. 4.7. Velocity profiles at $x=0$ for the subsonic flat plate flow at $Re=100$, non-limited second-order discretized Navier-Stokes equations
(------ : Blasius solution, ○ : after 1 IDeC-cycle, □ : after 50 IDeC-cycles).

4.3. SUPERSONIC FLAT PLATE FLOW

4.3.1. Purpose

The specific experiment by Hakkinen to be considered is that at $Re = 2.96\ 10^5$ [5]. Though more accurate and better documented shock wave - boundary layer experiments are available now (such as e.g. [3]), at present the Hakkinen experiment at $Re = 2.96\ 10^5$ still is the most popular test case for Navier-Stokes codes. Many numerical results are available for it. In particular because of the latter circumstance we consider this case; it allows us to make efficiency comparisons with other methods. The most delicate flow feature in the problem is a shock induced separation followed by a re-attachment.

Geometry and boundary conditions to be applied are given globally in Fig. 4.8. In all multigrid computations a 5×2-grid is applied as the coarsest grid Ω_1 (Fig. 4.8). The grid is optimized for convection by a stretching in flow direction and, in particular, by alignment with the impinging shock wave. A grid adaptation for diffusion is realized by a stretching in crossflow direction.

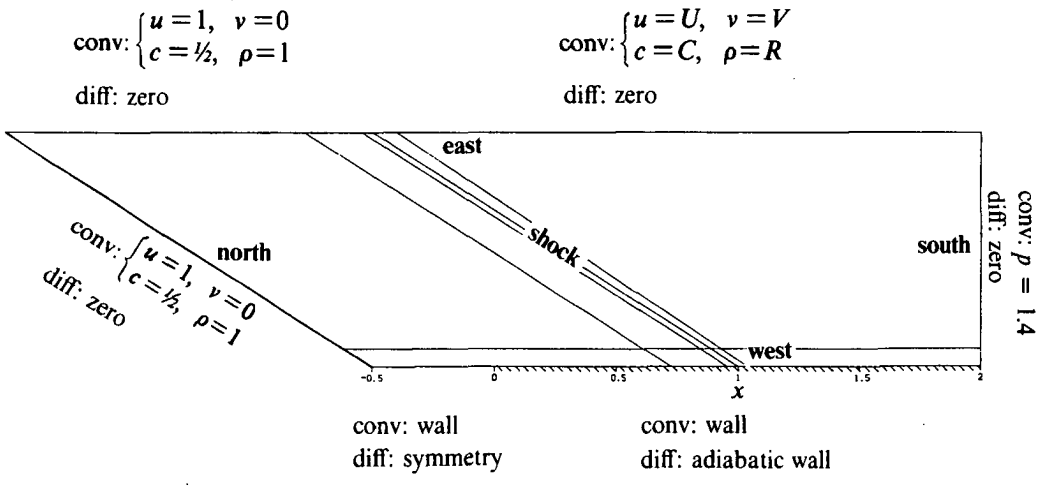

Fig. 4.8. Geometry, boundary conditions and coarsest grid (Ω_1) supersonic flat plate flow (conv: convection, diff: diffusion).

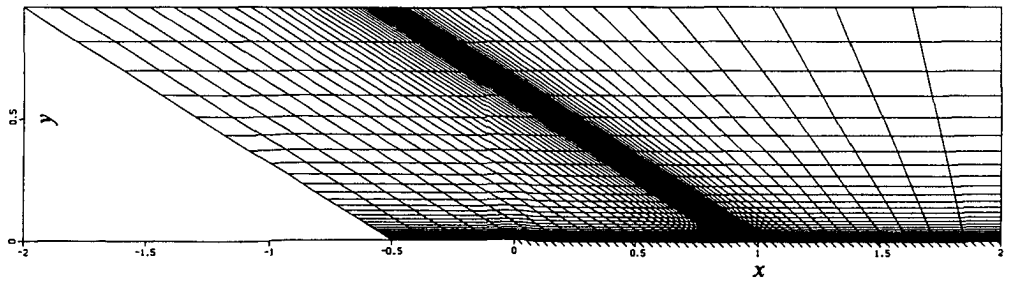

Fig. 4.9. 80×32-grid (Ω_5) supersonic flat plate flow.

4.3.2. First-order accurate results

Multigrid behaviour. Applying as finest finest-grid so far: the 80×32-grid given in Fig. 4.9, and applying as correction prolongation the first-order one only ($m_p=1$), we obtain the convergence results given in Fig. 4.10. The cause of the irregularities (bumps) in the convergence histories obtained for Ω_3 and Ω_4 is unclear. Despite the somewhat deteriorated multigrid convergence rates compared with those obtained for the subsonic flat plate flow (Fig. 4.5), multigrid still appears to be much faster than single-grid. The relatively strong deterioration of the multigrid method's convergence behaviour when going from Ω_4 to Ω_5 may be due to essential differences between the Ω_5-solution on the one hand and the underlying coarser grid solutions on the other hand. Comparison of the corresponding velocity profiles at $x=1$ shows e.g. that the Ω_5-solution is separated whereas the Ω_4-solution is still attached. (If desired, application of more sophisticated grid transfer operators might be efficacious for matching the subsonic flat plate flow's convergence rates.)

In none of these first-order computations the switched-relaxation-evolution approach needed to be invoked.

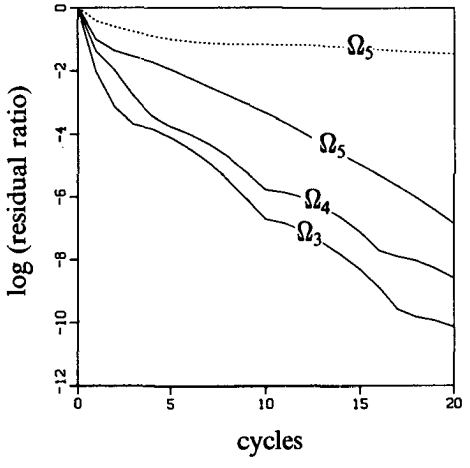

Fig. 4.10. Multigrid behaviour supersonic flat plate flow, $Re=2.96\ 10^5$, $m_p=1$ (····· : single-grid, —— : multigrid).

Efficiency. Despite the deterioration with respect to the subsonic flat plate flow, the multigrid method's performance for this problem is already competitive with two well-established solution methods for the full Navier-Stokes equations; those of Beam and Warming [1], and MacCormack [13]. Using a CDC 7600, Beam and Warming, and MacCormack converge to a comparably dissipative flow solution on a 32×32- and 32×45-grid, respectively, in: 100 and 256 iterations, and 46 and 40 *ms* per grid point, respectively. Using a CDC Cyber 205, with the present multigrid method we need for the 80×32-grid: 5 iterations (FAS-cycles) and 23 *ms* per finite volume, without optimization for vectorization. Though the Beam-Warming and MacCormack method are supposed to be somewhat more suitable for vectorization, for finer and finer discretizations the present multigrid method will be more and more efficient than these methods, due to its better grid-independence. Yet, the main advantage of the present method is supposed to lie, just as with the Euler equations (section 2.3.4), in the significantly smaller number of iterations required. For large-scale computations for which all data cannot be kept in core, the small number of iterations required results - again - in a small number of out-of-core data transports. Since, in particular for large-scale Navier-Stokes flow computations, IO-times rather than CPU-times may be the hampering factor, this property is an important advantage of the present method.

4.3.3. Second-order accurate results

Monotonicity. To investigate the monotonicity preserving properties of our limiter (3.28), we compute the Euler flow solution at Ω_5 (Fig. 4.9), using the $\kappa=\frac{1}{3}$-scheme with and without the limiter. Numerical results obtained are given in Fig. 4.11. The results show that the limiter does what it is supposed to do: making the solution monotone.

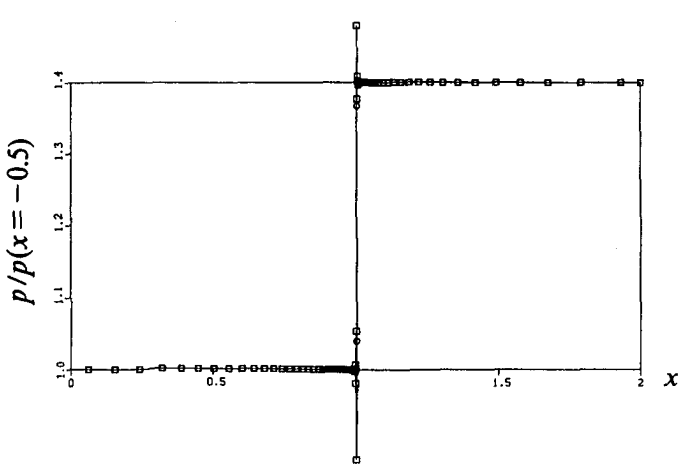

Fig. 4.11. Inviscid surface pressure distributions supersonic flat plate flow (○ : limited $\kappa=\frac{1}{3}$, □ : non-limited $\kappa = \frac{1}{3}$).

Line relaxation. To investigate the accuracy properties of our limited $\kappa = \frac{1}{3}$-discretization and to make comparisons with experimental results, we then tried to compute the higher-order Navier-Stokes solution on Ω_5. It appeared that the defect correction iteration needed to be damped. We had to apply

$$N_L(q_L^{n+1}) = N_L(q_L^n) - \omega N_L^+(q_L^n), \quad n = 0, 1, ..., N, \tag{4.1}$$

with ω some positive damping factor, for which no a-priori knowledge existed about its maximally allowable value. Continuing with this solution approach - reluctantly - we would be saddled with the first tuning parameter: ω. (We want to avoid the introduction of any tuning parameter.) Moreover, we would have lost the small advantage of diffusive term cancellation in the right-hand side of the defect correction iteration (section 3.3.3). Fortunately, replacing the point relaxation by line relaxation, it appeared that we could use $\omega = 1$ again.

As lines we apply now those crossing the layer and running into the outer flow: crosswise lines (Fig. 4.12). The corresponding multigrid behaviour is satisfactory, and in all first-order computations performed, no switch to an evolution approach needed to be made.

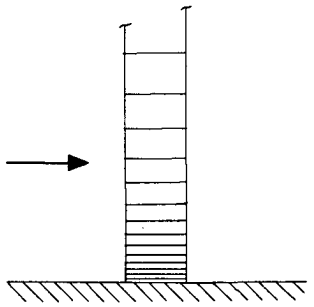

Fig. 4.12. Crosswise relaxation line.

Solution comparison. Applying (crosswise) line relaxation as smoother, and 20 IDeC-cycles with one FAS-cycle per IDeC-cycle, at Ω_5 we obtain the converged limited higher-order surface pressure distribution given in Fig. 4.13.

Comparing the higher-order surface pressure distribution and the corresponding first-order distribution (also given in Fig. 4.13), a large qualitative difference in the interaction region is clearly visible. The first-order pressure distribution lacks the plateau in the pressure distribution, which indicates that the first-order separation bubble is significantly smaller than the second-order one.

A qualitative difference between the higher-order and experimental results (see also Fig. 4.13) seems to be the expansion at the end of the pressure plateau. Though we assume it to be unlikely that in the experiment the expansion lies just in between two neighbouring pressure taps (this because of the absence of an expansion in any other such experiment), we are not (yet) convinced that the expansion is nothing but a numerical artefact. A separation bubble in a supersonic flow has expansion waves emanating above its convex side. Like in our higher-order solution, the presence of these waves might well be perceptible on the underlying surface.

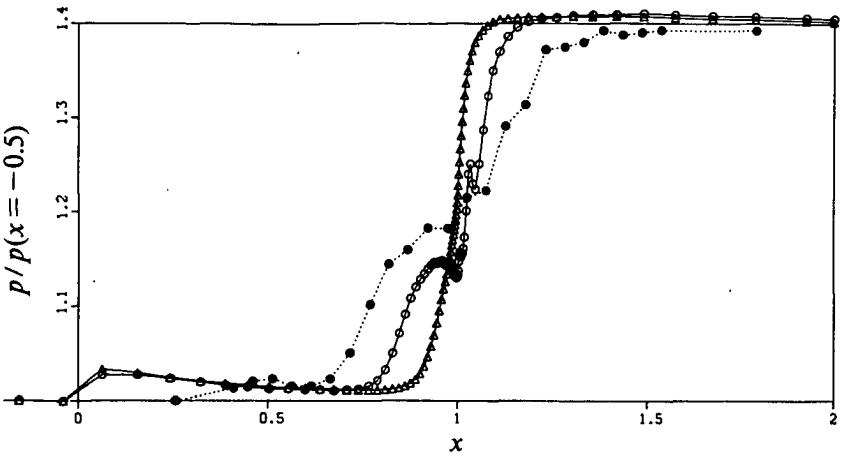

Fig. 4.13. Viscous surface pressure distributions supersonic flat plate flow, $Re = 2.96\ 10^5$, $\Omega_L = \Omega_5$ (△ : first-order, ○ : limited $\kappa = \frac{1}{3}$, ● : measured).

The wiggles in the higher-order distribution are supposed to be caused by the fact that the limiter cannot be applied near boundaries (section 2.3.2). To show that they are probably not a deficiency of the new limiter (3.28), in Fig. 4.14 we give the converged higher-order surface pressure distribution as obtained with the well-established Van Albada limiter (2.15). The Van Albada distribution appears to be oscillatory as well.

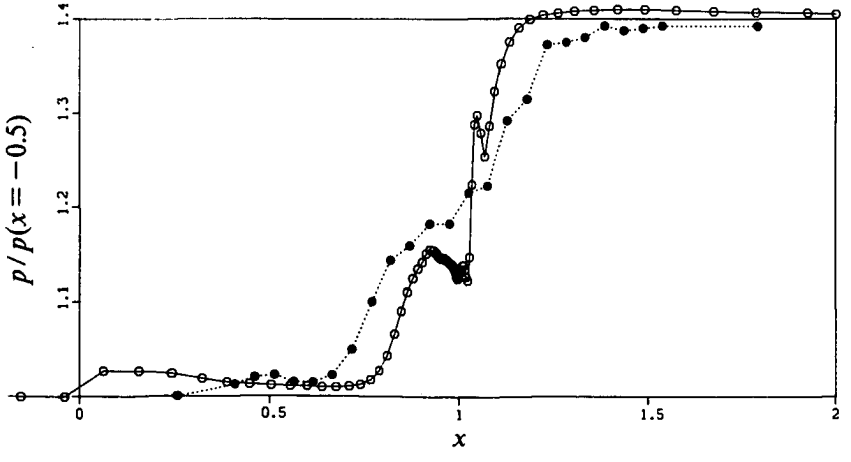

Fig. 4.14. Viscous surface pressure distributions supersonic flat plate flow, $Re = 2.96\ 10^5$, $\Omega_L = \Omega_5$ (○ : Van Albada, ● : measured).

To investigate whether the quantitative differences still existing between the higher-order and measured surface pressure distribution (such as the bubble length) are grid-independent errors of which the cause is not clear, we also compute the limited higher-order solution on Ω_6. (Uncertain error sources in the wind tunnel experiment might be crossflow influences, non-observed but non-negligible turbulence, some slight heat transfer through the wall, and so on. For the computation, an error source might e.g. be the neglect of temperature dependence in the diffusion coefficients.) The converged higher-order surface pressure distribution, as obtained on Ω_6, is given in Fig. 4.15. Comparison with the measured pressure distribution clearly shows a better resemblance than in the case of Ω_5 (Fig. 4.13), which indicates a probably rather small influence of the uncertain error sources. The converged first-order distribution is also given. Notice again the rather large qualitative difference between both computed distributions, the first-order one still without pressure plateau (though also without wiggles).

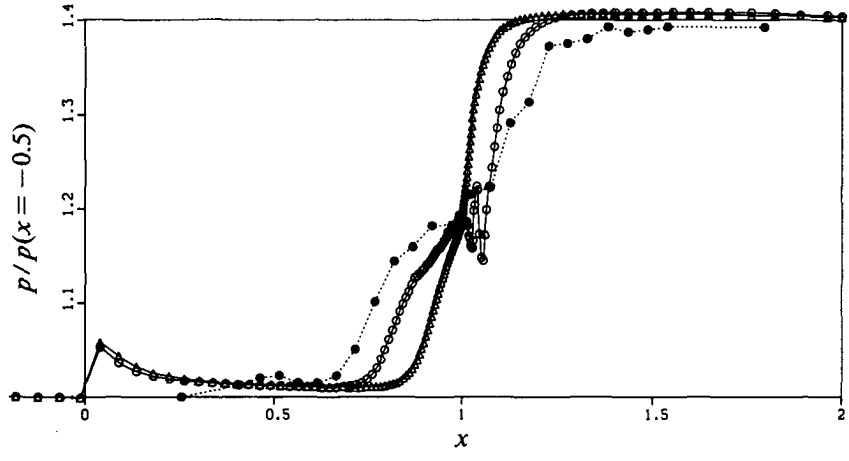

Fig. 4.15. Viscous surface pressure distributions supersonic flat plate flow, $Re = 2.96\ 10^5$, $\Omega_L = \Omega_6$ (△ : first-order, ○ : limited $\kappa = \frac{1}{3}$, ● : measured).

In Fig. 4.16 we also compare velocity profiles at an x-location inside the bubble. The smoothness of the higher-order velocity profile seems to justify the previous statement made about the oscillatory surface pressure distribution and the fact that limiters do not work near boundaries. The local maximum in both computed velocity profiles (Fig. 4.16a) probably corresponds with the expansion of the supersonic outer flow over the convex side of the bubble. To finish, in Fig. 4.17 we give a more global impression of the higher-order solution.

Again, in all previous computations a switch to an evolution was not necessary.

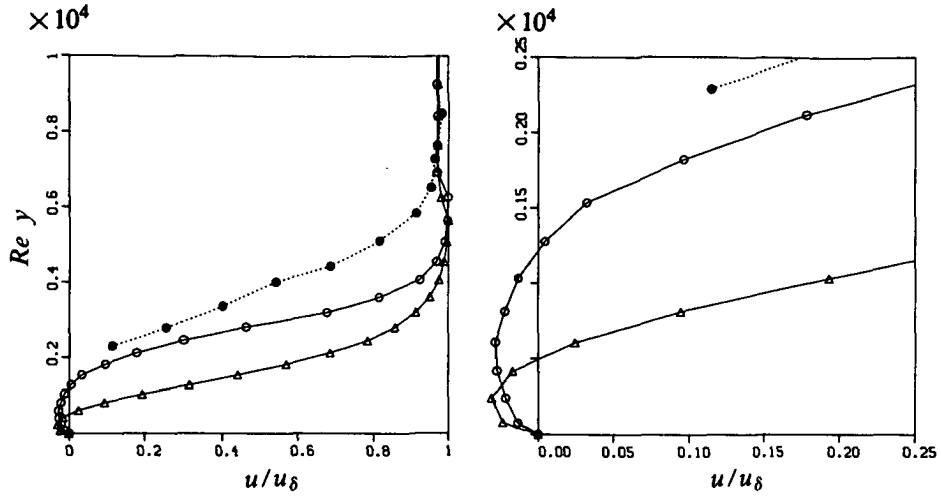

a. In full. b. In detail.

Fig. 4.16. Velocity profiles at $x = 2.87\ 10^5/Re$ supersonic flat plate flow, $Re = 2.96\ 10^5$, $\Omega_L = \Omega_6$ (△ : first-order, ○ : limited $\kappa = 1/3$, ● : measured).

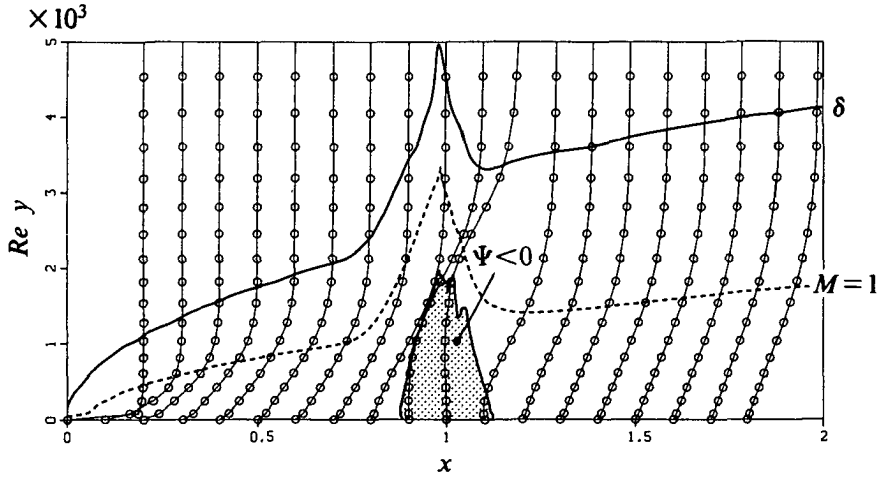

Fig. 4.17. Velocity profiles (○), boundary layer edge (δ), sonic line ($M = 1$) and separation bubble ($\Psi < 0$) for supersonic flat plate flow (limited $\kappa = 1/3$, $Re = 2.96\ 10^5$, $\Omega_L = \Omega_6$).

False diffusion. By presenting for Ω_5 not only the viscous solution obtained with the limited $\kappa = \frac{1}{3}$-scheme (Fig. 4.13), but also the corresponding inviscid solution (Fig. 4.11), insight was given about the amount of false diffusion present in the viscous solution. The fact that the present method can be used for both Navier-Stokes and Euler flows makes this comparison easy. Making the comparison is important. For example, when applying for the supersonic flat plate flow a commonly used rectangular grid, such as the rectangular equivalent of the grid in Fig. 4.9. (Fig. 4.18a), a viscous surface pressure distribution is obtained which seems to be very close to the experimental data (Fig. 4.18b). However, the corresponding inviscid distribution (Fig. 4.18c) indicates that this good resemblance is mainly caused by false numerical diffusion in the discretization of the convective terms, and hence is deceptive. In the many numerical results available in the literature for this specific Hakkinen test case, we have only seen that rectangular grids (like that in Fig. 4.18) were applied. Yet, we have not yet seen any such publication in which the corresponding inviscid solution is also shown.

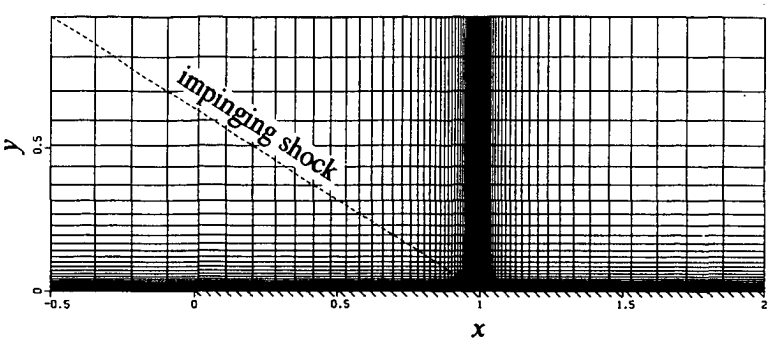

a. Grid.

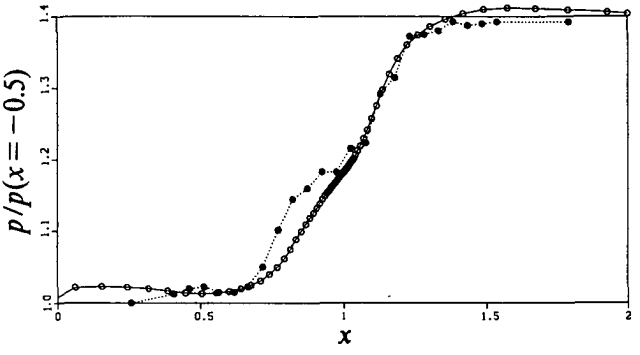

b. Viscous surface pressure distribution, $Re = 2.96\ 10^5$
(○ : limited $\kappa = 1/3$, ● : measured).

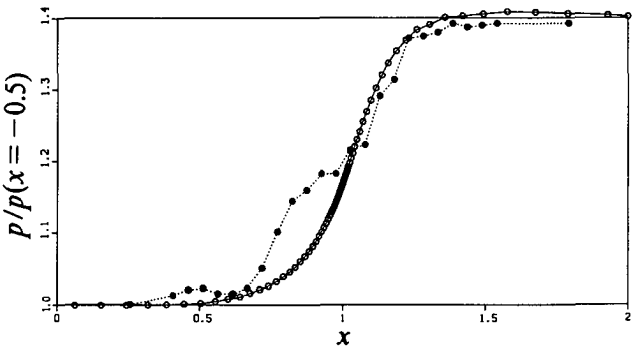

c. Inviscid surface pressure distribution
(○ : limited $\kappa = 1/3$, ● : measured).

Fig. 4.18. Results supersonic flat plate flow on rectangular grid.

4.4. HYPERSONIC BLUNT BODY FLOW

4.4.1. Purpose

To briefly explore the robustness of the solution method in hypersonics, we consider a hypersonic flow at $M_\infty = 8.15$, $Re = 10^{100}$ and $\alpha = 30^0$ around a blunt forebody with canopy. (So the flight situation considered is a reentry situation.) The forebody is composed out of two ellipse segments (Fig. 4.19), given by

$$\left.\begin{aligned} \left(\frac{x}{0.06}\right)^2 + \left(\frac{y}{0.015}\right)^2 &= 1 \\ \left(\frac{x}{0.035}\right)^2 + \left(\frac{y}{0.025}\right)^2 &= 1 \end{aligned}\right\} \quad x<0, \tag{4.2a}$$

and a parallel part, given by

$$\left.\begin{aligned} y &= -0.015 \\ y &= 0.025 \end{aligned}\right\} \quad 0 \leqslant x \leqslant 0.016. \tag{4.2b}$$

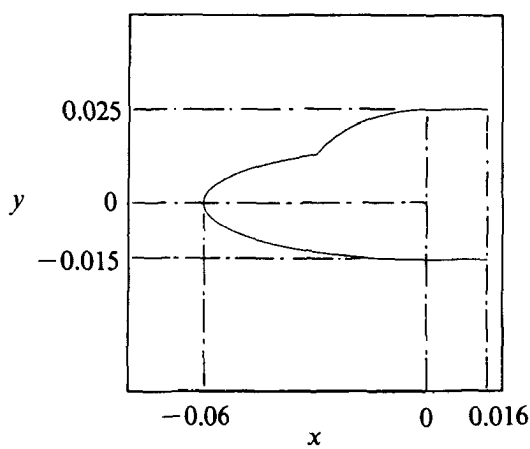

Fig. 4.19. Double ellipse.

As grids we use the C-type grids shown in Fig. 4.20. The grids are exactly equidistant in radial direction per radial column separately, and nearly equidistant in tangential direction, at the body.

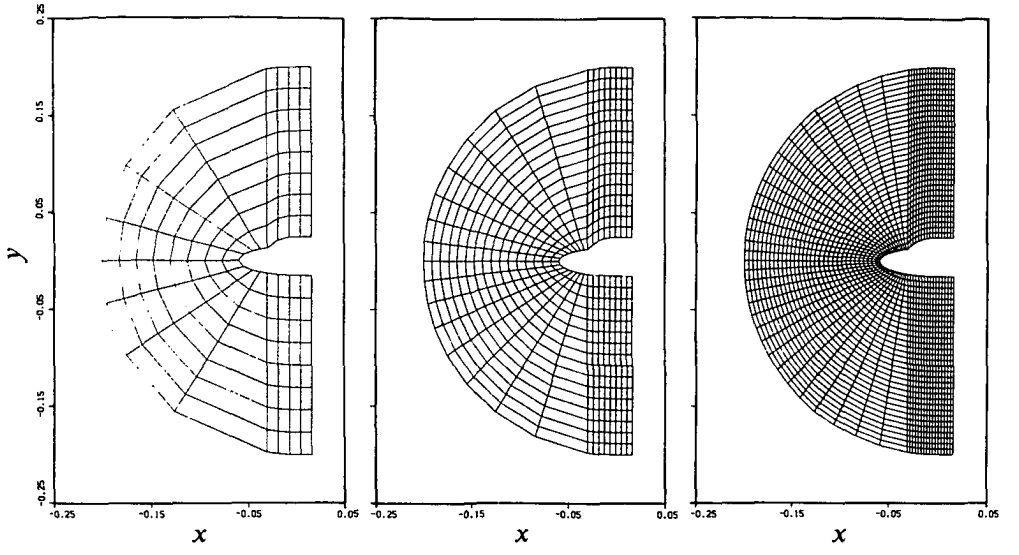

a. 16×8-grid. b. 32×16-grid. c. 64×32-grid.

Fig. 4.20. Grids double ellipse.

4.4.2. Single-grid results

Here the switched-relaxation-evolution strategy needs to be invoked. In Fig. 4.21 we show its behaviour for the 16×8-, 32×16-, and 64×32-grid, respectively. The residual ratio along the left vertical axes is the single-grid ratio $\Sigma_{k=1}^{4} |(N_1(q_1^n))_k| / \Sigma_{k=1}^{4} |(N_1(q_1^0))_k|$, where $|(N_1(q_1))_k|$ is defined as in section 4.2.2, with the only difference that here, n refers to the n-th (single-grid) relaxation-evolution cycle, one cycle being two diagonally opposite, symmetric relaxation-evolution sweeps. The solution q_1^0 is the uniformly constant initial solution which, in all three cases, fits continuously to the hypersonic upstream boundary conditions. The quantity along the right vertical axes is the permillage of volumes in the total number of finite volumes visited during one cycle, in which a switch to the evolution approach is made. The robustness of the switched-relaxation-evolution technique is clear. For none of the cases considered there is an abortion of the solution process. We even have convergence for all three cases. Further, from Fig. 4.21b and 4.21c, it appears that the evolution technique makes itself superfluous indeed.

With the present multigrid method - so far - no really satisfactory results have been obtained in eliminating the convergence slow down that can be clearly observed in Fig. 4.21 with decreasing mesh size. Present research is directed towards obtaining a satisfactory grid-independent acceleration technique for hypersonics.

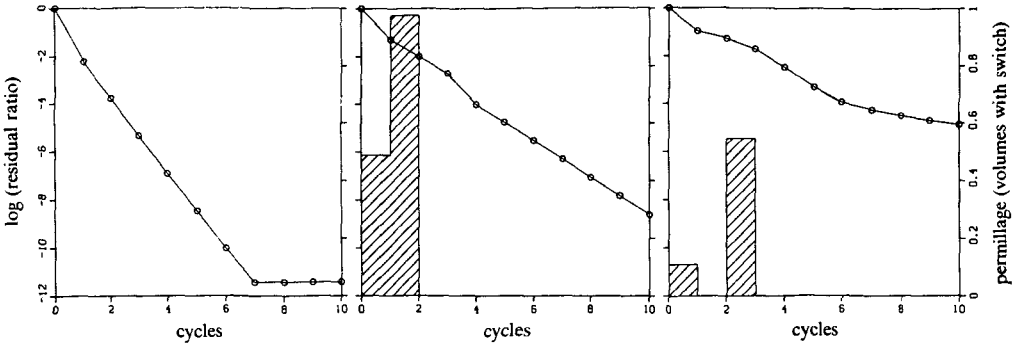

a. For 16×8-grid. b. For 32×16-grid. c. For 64×32-grid.

Fig. 4.21. Convergence results switched-relaxation-evolution technique.

4.5. Concluding remarks

With increasing Reynolds number, compared with Van Leer's scheme, Osher's scheme appears to lead to an increasingly more accurate resolution of boundary layer flows, in agreement with the theoretical results of section 3.2.2. Already for rather low Reynolds numbers the difference in accuracy is such that Osher's scheme is to be preferred for engineering purposes.

For sufficiently smooth flow problems, convergence to first-order truncation error accuracy is obtained within one FAS-cycle only. Second-order truncation error accuracy is obtained in two FAS-cycles only, the last cycle representing one defect correction cycle. For non-smooth flow problems, within the Mach number range of main interest ($\frac{1}{3} \lesssim M \lesssim 3$, section 1.4.1) a slight deterioration is observed with respect to smooth problems. Yet, the multigrid convergence rates obtained are still satisfactory. For hypersonic flows, the multigrid method's performance is no longer satisfactory. Our current research is directed towards an improvement of this performance. In hypersonics, the local switched-relaxation-evolution technique seems to be a good alternative for a failing local relaxation.

It is important to investigate the reliability of any computed Navier-Stokes solution with respect to the numerical errors in the discretization of the convective part. The present method allows an easy check of false diffusion. The same algorithm can be used for both viscous ($1/Re$) and inviscid ($1/Re = 0$) flow computations.

REFERENCES

1. R.M. BEAM AND R.F. WARMING, *An Implicit Factored Scheme for the Compressible Navier-Stokes Equations,* AIAA J. 16, 393-402 (1978).
2. H. BLASIUS, *Grenzschichten in Flüssigkeiten mit kleiner Reibung,* Z. Math. Phys. 56, 1-37 (1908).
3. G. DEGREZ, C.H. BOCCADORO AND J.F. WENDT, *The Interaction of an Oblique Shock Wave with a Laminar Boundary Layer Revisited. An Experimental and Numerical Study,* J. Fluid Mech. 177, 247-263 (1987).
4. W. HACKBUSCH, *Multi-Grid Methods and Applications* (Springer, Berlin, 1985).
5. R.J. HAKKINEN, I. GREBER, L. TRILLING AND S.S. ABARBANEL, *The Interaction of an Oblique Shock Wave with a Laminar Boundary Layer,* NASA, Washington, Memo 2-18-59 W (unpublished, 1959).
6. P.W. HEMKER, *Defect Correction and Higher Order Schemes for the Multi Grid Solution of the Steady Euler Equations,* in Multigrid Methods II, Proceedings of the Second European Conference on Multigrid Methods, Cologne, 1985, Lecture Notes in Mathematics Vol. 1228, 149-165, edited by W. Hackbusch and U. Trottenberg (Springer, Berlin, 1986).
7. P.W. HEMKER AND B. KOREN, *Multigrid, Defect Correction and Upwind Schemes for the Steady Navier-Stokes Equations,* in Numerical Methods for Fluid Dynamics III, Proceedings of the Third Conference on Numerical Methods for Fluid Dynamics, Oxford, 1988, 153-170, edited by K.W. Morton and M.J. Baines (Clarendon Press, Oxford, 1988).
8. B. KOREN, *Upwind Schemes for the Navier-Stokes Equations,* in Nonlinear Hyperbolic Equations - Theory, Numerical Methods and Applications, Proceedings of the Second International Conference on Hyperbolic Problems, Aachen, 1988, Notes on Numerical Fluid Mechanics Vol. 24, 300-309, edited by J. Ballmann and R. Jeltsch (Vieweg, Braunschweig, 1989).
9. B. KOREN, *Multigrid and Defect Correction for the Steady Navier-Stokes Equations,* J. Comput. Phys. (accepted for publication).
10. B. KOREN, *Upwind Schemes, Multigrid and Defect Correction for the Steady Navier-Stokes Equations,* in Proceedings of the 11th International Conference on Numerical Methods in Fluid Dynamics, Williamsburg, 1988, Lecture Notes in Physics Vol. xx, edited by D.L. Dwoyer and R.G. Voigt (Springer, Berlin, to appear).
11. B. KOREN, *Line Gauss-Seidel Relaxation and Multigrid for Steady, Two-Dimensional Flow Computations,* Centre for Mathematics and Computer Science, Amsterdam, Note NM-N8803 (unpublished, 1988).
12. B. KOREN, *Robustness Improvement of Point Gauss-Seidel Relaxation for Steady, Hypersonic Flow Computations,* Centre for Mathematics and Computer Science, Amsterdam, Note NM-N8805 (unpublished, 1988).
13. R.W. MACCORMACK, *A Numerical Method for Solving the Equations of Compressible Viscous Flow,* AIAA J. 20, 1275-1281 (1982).
14. P. WESSELING, *Linear Multigrid Methods,* in Multigrid Methods, Frontiers in Applied Mathematics Vol. 3, 31-55, edited by S.F. McCormick (SIAM, Philadelphia, 1987).

Chapter 5

Final Remarks

With the steady Navier-Stokes method presented in this thesis a reasonable compromise seems to have been found between the conflicting properties of accuracy and efficiency. In our opinion, a main characteristic of the method is that it does not have an upper bound in the Reynolds number above which it cannot be applied. Starting from any low, practically relevant Reynolds number, a smooth transition to the Euler flow regime seems to be possible. Though for the Mach number the applicability is restricted to a certain bounded range, the Mach number range over which the method works is still rather wide from the viewpoint of aerospace applications. No divergence problems are expected from medium-subsonic to medium-supersonic flow speeds. If - unexpectedly - the method does not work for some flow problem, it cannot be easily got going by altering a parameter in the algorithm. The algorithm does not have any real tuning parameter. As a consequence, in (in our experience) rare cases of divergence, in order to converge, one is obliged to analyze and understand the cause of divergence, which may only lead to a better and better method.

No major mathematical difficulties are expected from eliminating physical simplifications, such as the perfect gas and laminar flow assumptions. The same is expected for an extension to three dimensions.

Samenvatting

Numerieke aerodynamica speelt een belangrijke rol in de hedendaagse vliegtuigbouw. Het maakt het thans al mogelijk om met behulp van tamelijk complete stromingsmodellen als de Euler-vergelijkingen en de vergelijkingen van Navier-Stokes stromingssimulaties uit te voeren om volledige vliegtuigen. Betere numerieke methoden maken dat dit steeds nauwkeuriger en goedkoper kan. Voor de stationaire Euler-vergelijkingen is door Hemker en Spekreijse een numerieke methode ontwikkeld die aan deze vooruitgang bijdraagt. Gebaseerd op de Hemker-Spekreijse-methode wordt in dit proefschrift een numerieke methode gepresenteerd voor de meer complete stationaire vergelijkingen van Navier-Stokes.

Alvorens de uitbreiding naar Navier-Stokes te maken wordt in hoofdstuk 2 van dit proefschrift de Hemker-Spekreijse-methode eerst aan enige voor de praktijk belangrijke stromingsproblemen getoetst. Hierbij worden ook uitbreidingen als automatische roosteraanpassing en τ-extrapolatie onderzocht. Stromingsberekeningen worden uitgevoerd aan een enkelvoudig samenhangende geometrie (een windtunnelsectie) en enige meervoudig samenhangende geometrieën (vleugelprofielen). De stromingen variëren van volledig subsoon, via transsoon, tot (bijna) volledig supersoon. De resultaten zijn bevredigend en geven geen aanleiding om de gekozen Euler-methode niet uit te breiden naar Navier-Stokes.

In hoofdstuk 3 wordt de Navier-Stokes methode gepresenteerd. Beschouwd worden de stationaire, compressibele, tweedimensionale vergelijkingen van Navier-Stokes. De vergelijkingen worden gediscretiseerd in hun integraalvorm. Toegepast wordt een eindige-volume-discretisatie. Voor de berekening van de diffusieve fluxen wordt een tweede-orde nauwkeurig centraal schema gebruikt, en voor de convectieve fluxen een benaderende Riemann-oplosser. De oplossingsmethode (zie hierna) eist dat de fluxfuncties continu differentieerbaar zijn. Bekende benaderende Riemann-oplossers die hieraan voldoen zijn die van Osher en van Van Leer. Van Oshers schema is bekend dat het beter geschikt is voor Navier-Stokes dan Van Leers schema; het smeert sliplagen minder sterk uit. Resultaten worden getoond van een foutonderzoek uitgevoerd aan beide schema's. De convectieve discretisatie is eerste-orde nauwkeurig door de linker en rechter Riemann-toestand gelijk te nemen aan de toestand in de bijbehorende buurcel. Tweede- of derde-orde nauwkeurigheid wordt verkregen door stuksgewijs hogere-orde interpolatie van de linker en rechter Riemann-toestand. Een limiter wordt gepresenteerd die derde-orde nauwkeurige

fluxevaluaties mogelijk maakt. Voor een efficiënte oplossing van het stelsel gediscretiseerde vergelijkingen wordt toegepast: niet-lineair multirooster met collectieve, symmetrische Newton-Gauss-Seidel-relaxatie als gladmaker. De oplossingsmethode werkt uitstekend voor de eerste-orde gediscretiseerde vergelijkingen van Navier-Stokes. Moeilijkheden die kunnen optreden bij het toepassen van de methode op de hogere-orde gediscretiseerde vergelijkingen worden omzeild door buiten de niet-lineaire multiroosteriteratie defect-correctie-iteratie in te voeren. De hierbij te inverteren operator heeft een eerste-orde gediscretiseerd convectief deel. Convergentieresultaten worden gepresenteerd voor een drietal te inverteren operatoren, elk verschillend in de mate waarin de diffusieve termen worden meegenomen. De voorkeur wordt gegeven aan een operator met de volledige diffusieve Navier-Stokes-termen.

In hoofdstuk 4 tenslotte wordt de in hoofdstuk 3 gepresenteerde numerieke methode aan enige stromingsproblemen getoetst. Beschouwd wordt eerst een subsone vlakke-plaat-stroming waarbij de Blasius-oplossing als referentie wordt gebruikt. Vervolgens wordt beschouwd een supersone vlakke-plaat-stroming met scheve schokgolf-grenslaag-interactie. Hierbij worden windtunnelresultaten als referentie gebruikt. De resultaten zijn bevredigend. De in hoofdstuk 3 beoogde nauwkeurigheid en zuinigheid lijken voor een ruim gebied van getallen van Reynolds en Mach in de praktijk te zijn verkregen.

About the author

From September 1976 to September 1983 the author studied at the Delft University of Technology, Department of Aerospace Engineering, where he graduated on the application of a numerical method to transonic shock wave - boundary layer interaction. During the years 1981,1982 he was an undergraduate assistant at the department's Laboratory of High-Speed Aerodynamics, where he was involved with teaching in supersonic aerodynamics. In 1981, as a trainee at the National Aerospace Laboratory in Amsterdam, he also worked on the development of a computational method for the neutral atmospheric boundary layer.
In the academic year 1983-1984 the author studied at the Von Karman Institute for Fluid Dynamics, where he graduated with honours on the development of a numerical method for the steady, incompressible Navier-Stokes equations.
From July 1984 till the present the author is a research associate at the Centre for Mathematics and Computer Science in Amsterdam, where he is involved with the development of numerical methods for the steady Euler and Navier-Stokes equations.

12. De destijds door supporters van Eddy Merckx aan Joop Zoetemelk gegeven bijnaam 'wieltjeszuiger' getuigt van ondankbaarheid, gezien het feit dat bij twee van dergelijke, voldoende kort achter elkaar geplaatste lichamen, het voorste lichaam, dankzij het lichaam direct daarachter, óók een weerstand ondervindt die kleiner is dan wanneer dat lichaam alleen in die stroming zou zijn geplaatst.

13. Bij het door de Nederlandse overheid gevoerde stimuleringsbeleid ten aanzien van een pas enige decennia oude bezigheid als informatica dient te worden gewaakt voor wildgroei, en wel in het bijzonder voor overwoekering van een al enige millennia vruchtbare wetenschap als wiskunde.

14. Gezien de betere zorg door Albert Heijn aan zijn jongste medewerkers besteed, verdient het door de Nederlandse overheid gevoerde salarisbeleid ten aanzien van assistenten en onderzoekers in opleiding nog niet eens de benaming kruideniersbeleid.

Stellingen behorende bij het proefschrift

Multigrid and Defect Correction for the Steady Navier-Stokes Equations

van B. Koren

1. Ondanks het meer dissipatieve karakter leidt het Van Leer-schema niet voor alle Euler-berekeningen tot een betere multiroosterconvergentie dan het Osher-schema.
Hoofdstuk 2 van dit proefschrift.

2. Het 'stabiele' $\kappa = -1$-schema kan een defect-correctie-proces doen divergeren, terwijl voor identieke problemen, κ-schema's meer verwant aan het instabiele $\kappa = 1$-schema hetzelfde proces doen convergeren.
Hoofdstuk 2 van dit proefschrift.

3. Onnauwkeurigheden veroorzaakt door de in alle discretisatiemethoden voor de Euler-vergelijkingen noodzakelijk opgelegde numerieke dissipatie kunnen ten dele worden opgeheven in een nabehandeling met τ-extrapolatie.
Hoofdstuk 2 van dit proefschrift.

4. De vaste-wand-behandeling van Osher en Chakravarthy welke op correcte wijze compressies en expansies introduceert bij aan- respectievelijk afstroming van de wand, kan tot fysisch incorrecte toestanden leiden.
Hoofdstuk 3 van dit proefschrift.

5. Uitsmering van scheef door het rooster lopende discontinuïteiten, een nadeel van ééndimensionale Riemann-oplossers, kan worden verminderd door als upwind-richting per celwandje niet de (rooster-afhankelijke) normaalrichting op dat wandje te nemen, maar de (rooster-onafhankelijke) richting corresponderend met een eigenwaarde nul.
P.W. Hemker, B. Koren and B. van Leer, *A Grid-Decoupled, Rotated Upwind Scheme for the Multi-Dimensional Euler Equations* (in preparation).

6. Ondanks de beschikbaarheid van een betrouwbare hodograafoplossing is het NLR7301-profiel bij $M_\infty = 0.721$, $\alpha = -0.194^0$ een onbetrouwbaar testprobleem.
M. van der Nat, *De Stationaire, Compressibele, Niet-Viskeuze Stroming om het Profiel NLR7301 bij Ma =.721 en α=−.194⁰ (2-dimensionaal)*, Nationaal Lucht- en Ruimtevaartlaboratorium, Amsterdam, Memorandum AT-88-009 U (1988).

7. De stelling van Spekreijse dat de methode zoals beschreven in diens proefschrift niet geschikt is voor stromingen met een uniform laag getal van Mach M is pas correct voor $M \ll 1$, en vormt derhalve geen bezwaar voor de methode.
Stellingen behorende bij het proefschrift *Multigrid Solution of the Steady Euler Equations* van S.P. Spekreijse.

8. Toepassing van convergentieanalyse op het defect-correctie-proces

$$L_L(u_L^{n+1}) = (1-\omega)L_L(u_L^n) - \omega R_L(u_L^n), \quad n = 0,1,...,N,$$

waarin L_L het eerste-orde upwind gediscretiseerde linkerlid en R_L het centraal gediscretiseerde rechterlid van de scalaire vergelijking

$$\frac{\partial u}{\partial x} + \frac{\partial u}{\partial r} = -\frac{u}{r},$$

laat zien dat dit proces divergeert voor alle $\omega > 0$. Bij toepassing van een relaxatiemethode op een vergelijkbare discretisatie van de axiaal-symmetrische Euler-vergelijkingen dient derhalve de bronterm van deze vergelijkingen in de relaxatie te worden meegenomen.
A.J. Buijk, *Over de Uitbreiding van een 2-D Euler code naar Axiale Symmetrie d.m.v. een Defect Correctie Methode, voor Supersone Stromingen*, Afstudeerverslag, Faculteit Luchtvaart- en Ruimtevaarttechniek, Technische Universiteit Delft (1988).

9. Voor Euler- of Navier-Stokes-berekeningen aan ingewikkelde driedimensionale geometrieën biedt de Cartesiaanse roostermethode [1] betere perspectieven dan zowel de gestructureerde blokmethode [2] als de ongestructureerde triangularisatiemethode [3].

1. R.J. LeVeque, *Cartesian Grid Methods for Irregular Regions*, in Numerical Methods for Fluid Dynamics III, Proceedings of the Third Conference on Numerical Methods for Fluid Dynamics, Oxford, 1988, 375-382, edited by K.W. Morton and M.J. Baines (Clarendon Press, Oxford, 1988).
2. J.W. Boerstoel, *Numerical Grid Generation in 3-D Euler Flow Simulation*, in Numerical Methods for Fluid Dynamics III, Proceedings of the Third Conference on Numerical Methods for Fluid Dynamics, Oxford, 1988, 187-213, edited by K.W. Morton and M.J. Baines (Clarendon Press, Oxford, 1988).
3. A. Jameson, T.J. Baker and N.P. Weatherill, *Calculation of Inviscid Transonic Flow over a Complete Aircraft*, AIAA paper 85-0484 (1985).

10. Inverse Euler-berekeningen zoals voorgesteld door Jameson kunnen efficiënt worden uitgevoerd door gebruik te maken van geneste multiroosteriteratie met per (steeds fijner) fijnste rooster de multiroosteroplossing van het inverse probleem.
A. Jameson, *Aerodynamic Design via Control Theory*, Institute for Computer Applications in Science and Engineering, NASA Langley Research Center, Hampton, ICASE report 88-64 (1988).

11. Het slechte off-design lift-weerstand-gedrag zoals voorspeld door Erdmann en Zandbergen voor voor lift geoptimaliseerde rotatie-symmetrische ringvleugel-romp-configuraties heeft de veelbelovende eigenschap van deze configuraties (zeer hoge lift-weerstand-verhouding bij een laag constructiegewicht) niet overtuigend tenietgedaan, gezien het slechte off-design gedrag van de gebruikte rekenmethode.
S.F.A.H.P. Erdmann and P.J. Zandbergen, *A Survey of Ten Years of NLR Activities on Ringwing-Body Configurations (1956-1966)*, Nationaal Lucht- en Ruimtevaartlaboratorium, Amsterdam, NLR-TR-69070 U.